TIP-ENHANCED RAMAN SPECTROSCOPY IN ULTRA-HIGH VACUUM

PHILIP SCHAMBACH

Dissertation
eingereicht im Fachbereich Physik
der Freien Universität Berlin

August 2013

angefertigt am Fritz-Haber-Institut

Datum der mündlichen Prüfung:
1. Oktober 2013

Betreuer der Arbeit:
Dr. Bruno Pettinger

Befürwortender Professor am Fachbereich Physik:
Prof. Dr. Martin Wolf

Zweitgutachterin:
Prof. Dr. Stephanie Reich

ABSTRACT

Tip-enhanced Raman spectroscopy (TERS) is a promising new scanning probe technique for the investigation of the vibrational properties of molecules on surfaces. TERS possesses both, a very high sensitivity - down to the single molecule level - and a spatial resolution in the 10 nm range.

In contrast to most TERS studies, we perform our experiments under ultra-high vacuum (UHV) conditions to ensure a high sample quality. Therefore, we have added a preparation chamber to the existing UHV-TERS set-up. Large parts of the work were devoted to improving the capabilities and the manageability of the UHV-TERS device.

We have chosen the fullerene C_{60} on a Au(111) surface as sample system. From a large body of literature the vibrational as well as the adsoption properties of C_{60} are well understood. Compared to other molecules studied in UHV-TERS, C_{60} has a much smaller Raman cross-section. This allows to test if our experiment can be applied to a larger class of molecular adsorbates with comparably small Raman cross-sections. To separate the signals of C_{60} from those of foreign molecules, we have recorded time-resolved series of tip-enhanced Raman (TER) spectra. For the analysis we select series showing the typical vibrational features of C_{60} that were stable over several seconds to minutes.

TER spectra of C_{60} show a remarkable dependence on the bias voltage applied between tip and sample, indicating a significant influence of the tip-sample separation on the signal strength, even on a sub-nanometer scale.

Measurements on different morphologies of C_{60} on Au(111) exhibit shifts for certain Raman peaks that are discussed in the context of different adsorption sites and polymerisation in the C_{60} adlayer.

Finally, we present experiments, in which scanning tunneling microscopy images of C_{60} on Au(111) and TER spectra were acquired from the same spatial region. These results can act as the point of departure for future measurements with simultaneously recorded TERS maps and topographic images, that allow a correlation between chemical and structural information on the nm scale.

ZUSAMMENFASSUNG

Spitzenverstärkte Raman Spektroskopie (tip-enhanced Raman spectroscopy, TERS) ist eine vielversprechende, neue Rastersondentechnik für die Untersuchung von Schwingungseigenschaften adsorbierter Moleküle. TERS verfügt über eine hohe Empfindlichkeit, bis hin zur Einzelmoleküldetektion, bei einer Auflösung im 10 nm-Bereich.

Im Gegensatz zu den meisten TERS-Studien führen wir unsere Experimente im Ultrahochvakuum (UHV) durch. Um eine gute Probenqualität zu gewährleisten, wurde die bestehende UHV-TERS Apparatur um eine Präparationskammer erweitert. Ein substantieller Teil der Arbeit bestand in der Erweiterung der experimentellen Möglichkeiten, sowie der Handhabbarkeit des UHV-TERS Gerätes.

Wir haben das Fulleren C_{60} auf einer Au(111) Oberfläche als Probensystem gewählt. Aus der umfangreichen Literatur sind die Schwingungs- und Adsorptionseigenschaften von C_{60} bekannt. Im Gegensatz zu in anderen UHV-TERS Experimenten verwendeten Molekülen, hat C_{60} einen sehr kleinen Raman Streuquerschnitt. Dieser Sachverhalt erlaubt es, die Möglichkeiten unseres Experiments für eine große Klasse von Adsorbaten mit vergleichbar niedrigen Streuquerschnitten zu untersuchen. Um Signale von C_{60} und Fremdmolekülen voneinander zu trennen, haben wir zeitaufgelöste Reihen von spitzenverstärkten Raman (TER) Spektren aufgenommen. Nur die für C_{60} charakteristische Spektren, die über mehrere Sekunden bis Minuten stabil waren, wurden zur Auswertung herangezogen.

Die Abhängigkeit der TER Spektren von C_{60} auf Au(111) von der zwischen Spitze und Probe angelegten Spannung weist auf einen erheblichen Einfluss des Spitze-Probe-Abstandes auf die Signalstärke hin, auch im Sub-Nanometersbereich.

Unterschiedliche C_{60}-Bedeckungen ergeben Energieverschiebungen einiger TERS-Banden. Dies wird im Zusammenhang mit verschiedenen Adsorptionsplätzen und einer möglichen Polymerisierung der C_{60}-Schichten diskutiert.

Zuletzt werden Experimente präsentiert, in denen rastertunnelmikroskopische Bilder von C_{60} auf Au(111) und TER Spektren an der gleichen Stelle der Probe aufgenommen wurden. Diese Ergebnisse liefern einen Ausblick auf Korrelation von struktureller und chemischer Information im nm Bereich.

CONTENTS

LIST OF FIGURES

LIST OF TABLES

1 INTRODUCTION

Tip-enhanced Raman spectroscopy (TERS) is a combination of three interesting scientific fields: Raman spectroscopy, scanning probe microscopy (SPM) and plasmonics providing remarkable enhancement effects for optical processes. For molecules exhibiting high resonance Raman cross-sections, TERS enables the identification of molecules on surfaces down to the single molecule level at a spatial resolution of about 10 nm. For molecules exhibiting only normal Raman cross-sections, TERS still permits spectra to be recorded for submonolayer coverages with a resolution of about 10 nm. In other words, TERS operates in a nano scale regime providing chemical and structural information. Figure 1 illustrates the concept of TERS.

Raman spectroscopy is based on the inelastic scattering of photons, called the Raman effect, to honor its discoverer, Sir Chandrasekhara Venkata Raman [1–3]. When light scatters from a molecule, some photons transfer a portion of their energy to the molecule by exciting molecular vibrations. The remaining energy is emitted simultaneously as a frequency shifted photon. By detecting the energy of the scattered photons one can, hence, determine the vibrational modes of the molecules. As vibrations are characteristic for molecules and their physical and chemical states, Raman spectroscopy nowadays is a routinely used technique for chemical analysis that is appreciated by scientists in many fields of biology, chemistry and physics [4].

As it is a linear optical spectroscopy, the spatial resolution of Raman spectroscopy is restricted by the Abbe diffraction limit to about half the wavelength of the light involved [5]. Normally, visible to near infrared light is employed in a Raman experiment and, hence, the spatial resolution is in the 200 to 500 nm range. Another limitation of Raman spectroscopy is that its efficiency is extremely small, i.e. under typical conditions only large amounts of sample molecules can be detected with this technique.[1] In fact, for the first 45 years after the discovery of the Raman effect it was believed that the detection of monolayers of molecules adsorbed at surfaces would not be possible with this technique.[2]

1 As a rule of thumb, for a 1 W laser line incident on a suitable sample, the return is about 10^{-10} W of inelastically scattered light.

2 An exception is the investigation of powder samples where the surface area is so high that a very high concentration of adsorbed molecules exist in the probed volume [6]

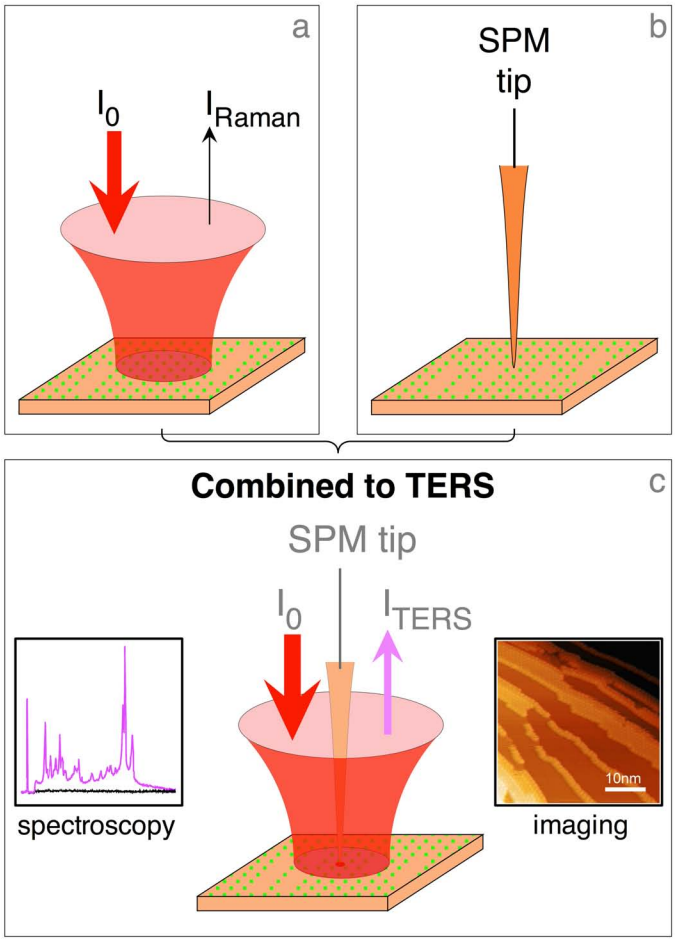

FIGURE 1: Scheme of tip-enhanced Raman spectroscopy (TERS). a) Raman scattering experiment. b) Scanning probe microscopy (SPM). c) Combination of SPM with Raman spectroscopy to TERS. TERS provides a high spectral sensitivity (left inset) together with topographic data (right inset).

An analytical tool that is routinely used for the characterization of molecules on (semi)conducting surfaces is the scanning tunneling microscope (STM) [7–10]. The STM is the type of SPM used for the experiments presented in this thesis. An atomically sharp metal tip is scanned across the surface of the sample at about 1 nm distance, while a bias voltage is applied between tip and sample. Due to the quantum mechanical tunneling effect a small current, that exponentially depends on the tip sample separation, flows between tip and sample. Because of this exponential distance dependence, the tip can be positioned very precisely over the sample with the aid of a piezo motor and scanner. Employing an STM, topographic images of surfaces and adsorbates can be obtained with atomic resolution. An identification of different chemical species is, however, not trivial with STM.

To investigate adsorbates on surfaces it would be beneficial to have a technique at one's disposal that combines the high content in chemical information of Raman spectroscopy and the high spatial resolution of an STM.

Optical measurements below the Abbe limit can, e.g., be performed with a scanning near-field optical microscopes (SNOM). These devices make use of evanescent waves that are produced when light tunnels through the very small aperture at the end of a tapered optical fiber [11–15]. The resolution is essentially controlled by the size of the aperture. Theoretically, using smaller and smaller apertures any resolution could be achieved. However, the smaller the aperture the lower is also the fraction of the transmitted and back-scattered light. Moreover, there are also technical limitations in the fabrication of such small apertures. In practice, the resolution achieved is usually in the several 10 nm range [16].

Because of the low efficiency of the Raman scattering mentioned above, a Raman experiment on (sub)monolayers of molecules on plane surfaces can only be successful if the scattering process can be enhanced significantly in some way.

One enhancement mechanism that has been known for quite some time is the resonance Raman (RR) effect [17]. When the incoming light is in resonance with an electronic transition of a molecule, the inelastically scattered fraction of the light can be augmented by up to five orders of magnitude [18]. However, it is not allways possible to employ RR because the laser has to be chosen according to the probe molecule and the RR effect is governed by selection rules different to normal Raman spectroscopy. Especially when more than one molecular species with separate electronic transition energies are to be probed, the RR approach is no longer applicable. Furthermore,

strong fluorescence may often arise and obscure any resonance Raman scattering. Only recently, Le Ru *et al.* developed a method to measure resonance Raman spectra and cross-sections even in the presence of overwhelming fluorescence with continuos wave excitation [18]. Before this invention, time-resolved techniques had to be employed to measure RR spectra of the most efficient flurophores [19–25]. There are further drawbacks of using or relying on a RR effects: because the molecules studied with RR absorb a lot of energy, photochemical processes, dissociation, degradation and photobleaching may distort adsorbates themselves as well as their structural arrangement.

Surface-enhanced Raman spectroscopy (SERS) is another enhancement effect and was discovered in the mid 1970s [26, 27]. At rough surfaces or colloids made of coinage metals the fraction of Raman scattered photons can be enhanced tremendously [26, 27]. It has been established that SERS is in fact a combination of several different effects. It is generally accepted that an electromagnetic enhancement effect gives the strongest contribution to the enhancement of up to a factor of 10^{10} [28]. The metal nano structures that compose the SERS substrate act as optical antennas [29, 30] for electromagnetic radiation in the visible wavelength range, much in the same way that radio antennas work for radio waves. Free radiation is effectively transduced to a near-field in the vicinity of the nano structure. This near-field drives the excitation part of SERS by an enhanced rate. The scattering part is enhanced as well by coupling the scattered photon near-field via the nanostructure to the far field.

In 2000, Stöckle *et al.* were the first to publish experimental work where the tip of an atomic force microscope (AFM) was used as optical antenna to enhance the Raman scattering of molecules adsorbed on a surface, thus tip-enhanced Raman spectroscopy was born [31]. As the near-field close to a single nano-particle (the tip of an AFM or STM) is responsible for the enhancement effect, the spatial resolution of TERS is approximately the size of this particle, typically around 10 to 100 nm. In the first year after its invention, three other research groups published their TERS results [32–34].

TERS as an experimental tool has diversified in many directions and is now employed by physicists, chemists and biologists [35–46].

To investigate the interaction between molecules and surfaces, a high degree of control of the sample preparation and low amounts of contamination are required. An ultra-high vacuum (UHV) environment provides these conditions. The first publications on UHV-TERS stem from our group [40, 47]. One part of this thesis is about the improvements made to the set-up used for these first UHV-TERS exper-

iments. The chellanges involved in performing TERS measurements under UHV conditions can already be estimated by the fact that up to this date, more the 10 years after the first TERS experiments, only five groups have published results of UHV-TERS experiments [40, 41, 47–51].

In many TERS studies, and in particular in UHV-TERS experiments, a combination of the two aforementioned enhancement mechanisms were used, i.e. the substances under observation exhibit a RR effect.

We have chosen the Fullerene C_{60} as a model molecule, because it belongs to the large class of molecules having rather low Raman cross-sections of $\leqslant 10^{-28}\,\mathrm{cm^2\ sr^{-1}}$. In a long term view, TERS is becoming a general analytical tool only if it is not restricted to Raman scatterers exhibiting many orders of magnitude higher cross-sections, such as the typical dye molecules commonly used in UHV-TERS experiments. Hence, on the one hand, TER studies on C_{60} represent a much more challenging task than TERS on dyes. On the other hand C_{60} offers the advantage of a large body of literature about its properties. In particular, C_{60} is well characterized by Raman and other vibrational spectroscopies [32, 52–65]. The growth and structure of C_{60} on $Au(111)$ have been studied by STM [66–68]. C_{60} forms stable two-dimensional islands of monomolecular thickness, which grow from the step edges of the substrate onto the terraces. This is an ideal starting point for our studies, because by varying the size of these islands the ratio between step- and terrace-adsorbed molecules can be varied and that should permit spectroscopic analysis.

The thesis is organized as follows: The fundamentals needed to understand TERS are addressed in Chapter 2. A description of the UHV-TERS set-up and its operation is presented in Chapter 3, including a report of the most important improvements. Some of the details of tip preparation with different etching methods are explained in more detail in the appendix Section A.3. Important steps of the alignment of the optical set-up are also presented in the appendix Section A.1 and Section A.2

Chapter 4 reports the experimental results. We present UHV-TER spectra of molecules (C_{60}) that do not show resonance Raman contributions at the excitation laser wavelength. In addition, for adsorbed C_{60} we show the full spectral window between $200\,\mathrm{cm^{-1}}$ and $1600\,\mathrm{cm^{-1}}$ containing more than 20 TERS peaks and shoulders [41]. This complements previous TERS publications, where merely smaller spectral clips for undefined C_{60} samples are presented [32, 63–65]. Chapter 4 is divided into five sections:

Section 4.1 explains general observations in TER spectra of C_{60} on Au(111) and compares them to the literature. Section 4.2 shows the mode of data acquisition and treatment. In Section 4.3, experimental results are reported and discussed that concern the response of TER spectra of C_{60} on Au(111) on a number of external parameters. In Section 4.4 STM imaging is used to characterize the compositions of the C_{60} adlayers on Au(111) surfaces, which were then spectroscopically analysed. Finally, in Section 4.5, experiments are presented where STM images and TER spectra of C_{60} on Au(111) are directly correlated.

The conclusions from this work are presented in Chapter 5 , followed by an outlook.

2

EXPERIMENTAL TECHNIQUES AND THEORY

Tip-enhanced Raman spectroscopy (TERS) is a recent development in the field of surface-enhanced Raman spectroscopy (SERS). It overcomes most of the drawbacks of other SERS techniques, such as the restriction to rough sample surfaces. It also bears the possibility to perform a local Raman spectro-microscopy with resolutions in the 10 nm range.

Any TER set-up is the combination of a scanning probe microscope (SPM), a plasmonic near-field tip that mediates the enhanced inelastic light scattering (to be described below) and a Raman spectrograph. The SPM serves to position the near-field tip accurately over the sample surface. This tip is responsible for the physical effect behind TERS, which is the same as in other SERS experiments: incident monochromatic light couples to oscillations of the free electrons in the metal tip, so-called localized surface plasmon-polaritons (LSPP). These plasmon-polaritons produce a highly enhanced electromagnetic field near the tip apex. Raman scatterers in this "hot spot" [69] are exposed to the enhanced incident field. Simultaneously, the induced dipole couple back to corresponding surface plasmon modes of the tip, such that also the inelastically scattered light is strongly enhanced. The Raman spectrograph then serves to block out the elastically scattered light and to detect the inelastic components. These carry the information about the vibrational modes of the sample useful for chemical identification.

Since the invention of TERS, different SPMs have been used in experimental set-ups. These SPMs are scanning tunneling microscopes (STM) [7–10] and atomic force microscopes (AFM) [70]. We have chosen an STM in our set-up. The fundamental concept of this device is presented in Section 2.1. Section 2.2 then gives a short introduction into Raman spectroscopy. Finally, SERS and TERS are discussed in Section 2.3.

2.1 SCANNING TUNNELING MICROSCOPE

The scanning tunneling microscope (STM) was invented in 1982 by Binnig and Rohrer [7–10]. In 1986 they were awarded the Nobel Prize in physics for providing the world with this intriguing development. Soon STM has been developed into a well-established tool for the characterization of surfaces of conducting and semiconducting samples by imaging them with sub-nanometer resolution. The principle of operation of the STM is depicted in Figure 2. The physical principle used in STM is the quantum mechanical tunneling effect through a small potential barrier. Piezo elements are employed to position a sharp metal tip over the sample at a distance of about one nano meter (tunneling gap) with very high precision. The tunneling effect allows electrons to pass into the classically forbidden zone of the tunneling gap and to reemerge at the other side. If a *bias voltage* (U_B) in the range of some mV to some V is applied between tip and sample a current (*tunneling current* I_t) can be detected. The magnitude of the current depends exponentially on the tip sample separation. The effect is in fact so pronounced that the major part of the tunneling current flows through the single atom that is closest to the sample. An electronic feedback loop uses the tunneling current as an input signal to keep the tunneling gap constant by adjusting the position of the tip along the direction of the surface normal (z-direction). By scanning the tip over the sample surface at constant tunneling current and recording the z-position of the tip at each point (Figure 2 b)), an STM *topography image* of the surface can be acquired. Figure 2 c) shows such a topographic image of C_{60} molecules absorbed on the terraces of an $Au(111)$ surface.

In the following the theory behind the STM technology is discussed. One of the first theoretical works regarding the interpretation of STM results is by Tersoff and Hamann [72]. Their calculations are based on an many particle approach of Bardeen [73] to describe the tunneling process in a metal-insulator-metal tunneling junction. Tersoff and Hamann [72] give a very demonstrative description of the tunneling process in STM, that is reproduced in the following:

If the electron wave functions to either side of the tunneling gap are Ψ_ν and Ψ_μ, respectively, and the bias voltage U_B is applied across the gap, first order perturbation theory leads to the following expression for the tunneling current:

$$I_t = \frac{2\pi e}{\hbar} \sum_{\mu,\nu} f(E_\mu)\,(1 - f(E_\nu + eU_B))\,|M_{\mu\nu}|^2 \delta(E_\mu - E_\nu) \qquad (1)$$

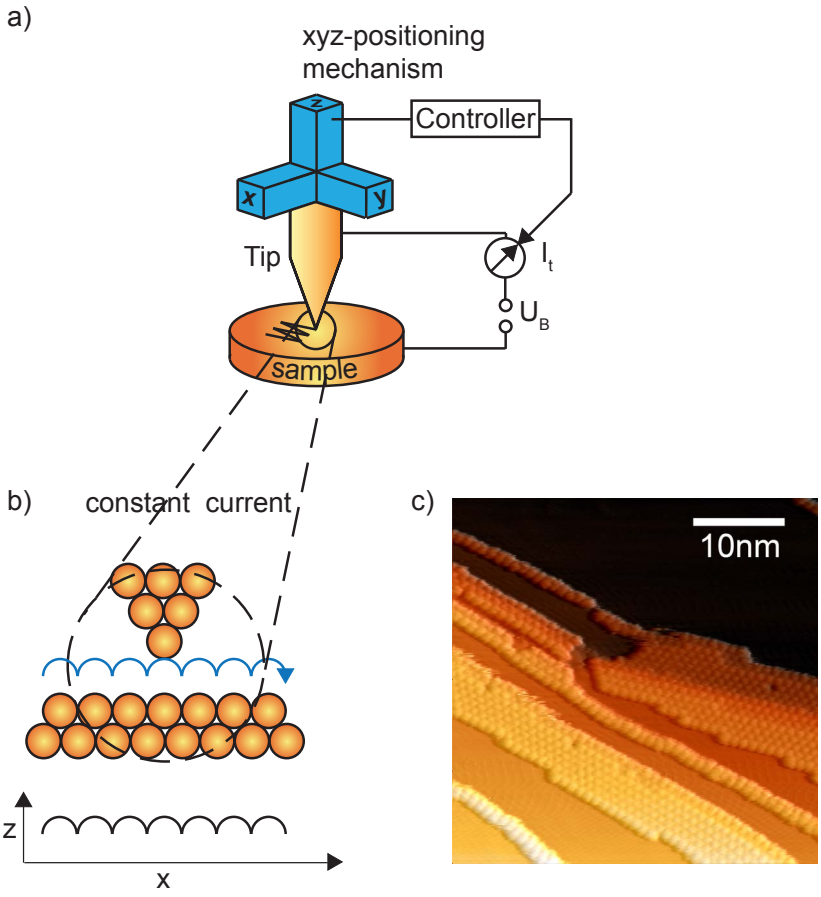

FIGURE 2: Scheme of the mode of operation of an STM. The image is an adaptation from [71]. a) the positioning mechanism with the feedback loop. b) close up view of the tunneling gap with movement of the STM tip during the scan and the recorded hight signal. c) STM image of C_{60} molecules adsorbed at step edges of an Au(111) surface. For improved visibility of the C_{60} molecules a gradient of the image is added to the topographic image.

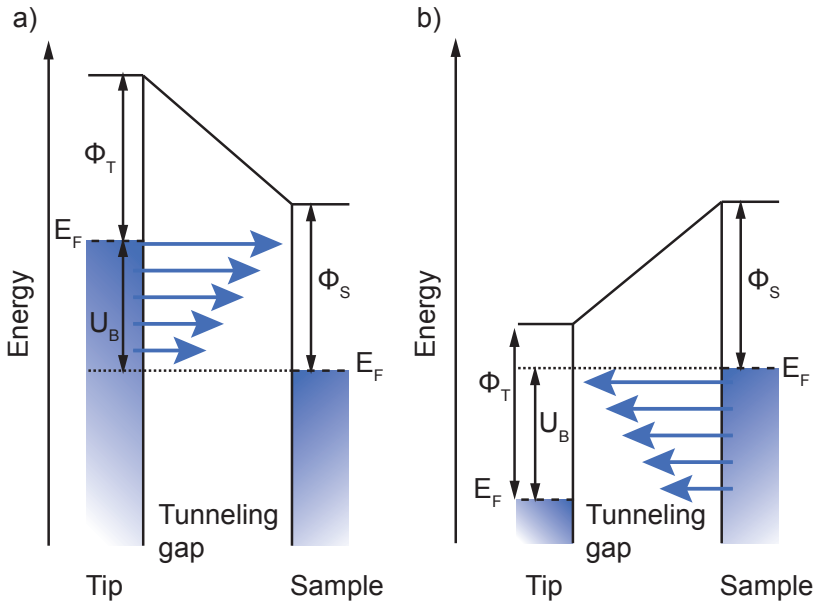

FIGURE 3: Energy diagrams for the tunneling process. Adapted from [71]. a) positive sample bias voltage. b) negative sample bias voltage.

$f(E_\mu)$	: Fermi function
U_B	: applied voltage
$M_{\mu\nu}$	: tunneling matrix element between states Ψ_μ and Ψ_ν.

Figure 3 shows an energy scheme for the tunneling process for positive (a) and negative (b) sample bias voltage. Φ_S and Φ_T are the work functions of the sample and the tip, respectively. U_B is the bias voltage, E_F the Fermi energy. Shaded blue areas symbolize the electron density of the tip and the sample. Blue arrows stand for the tunneling electrons, where the length of the arrow is the tunneling rate at the given energy. The tunneling rate of electrons close to the Fermi energy of the electrode that is higher in energy is higher than at lower energies. All electrons in the energy window $[E_F, E_F + U_B]$ contribute to the tunneling current.

For low bias voltages (U_B) like they are typical in STM measurements and low temperatures ($T \to 0, U_B \to 0$) only states near the

Fermi energy E_F are important and the Fermi function can be approximated by a step function. Equation 1 then simplifies to

$$I_t = \frac{2\pi}{\hbar} e^2 U_B \sum_{\mu,\nu} |M_{\mu\nu}|^2 \delta(E_\nu - E_F)\, \delta(E_\mu - E_F) \tag{2}$$

Bardeen [73] evaluates the tunneling matrix element

$$M_{\mu\nu} = \frac{\hbar}{2m} \int d\vec{S} \left(\Psi_\mu^* \vec{\nabla} \Psi_\nu - \Psi_\nu \vec{\nabla} \Psi_\mu^* \right), \tag{3}$$

where Ψ_ν and Ψ_μ are the wave functions of the two electrodes. The integral is taken over a surface S separating the electrodes.

Tersoff and Hamann assume special forms of the wave functions to apply the theory to the case of STM [72]. The wave function of the surface under consideration decays exponentially outside the metal and is given by

$$\Psi_\nu = \Omega_S^{-\frac{1}{2}} \sum_G a_G \exp\left[-\left(k^2 + |\vec{k}_\parallel + \vec{G}|^2 \right)^{\frac{1}{2}} z \right] \exp\left[i \left(\vec{k}_\parallel + \vec{G} \right) \vec{x} \right] \tag{4}$$

Ω	: sample volume
$k = \hbar^{-1} (2m\phi)^{\frac{1}{2}}$	: inverse decay length of Ψ_ν in vacuum
ϕ	: work function
$\vec{k}_\parallel$	: surface Bloch wave vector of the state
$\vec{G}$	: surface reciprocal lattice vector

Note, that this is a completely general form of a wave function that decays exponentially away from the surface.

The wave function of the tip is not known in general. It is modeled to be of spherical symmetry and decays exponentially into the vacuum

$$\Psi_\mu = \Omega_t^{-\frac{1}{2}} c_t\, k\, R \exp[kR] \left(k|\vec{r} - \vec{r}_0| \right)^{-1} \exp\left[-k|\vec{r} - \vec{r}_0| \right] \tag{5}$$

Ω_t	: probe volume	(6)
R	: radius of curvature, assumed to be $>> k^{-1}$	
$c_t \approx 1$	: normalisation factor	

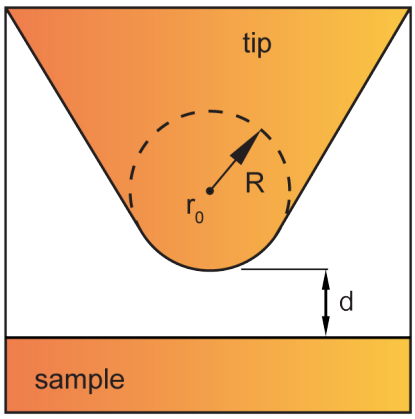

FIGURE 4: Image adapted from [72]. A scheme of the tunneling junction is shown. The tips center of curvature is r_0 and its radius R. The minimal distance between tip and sample is d.

In Figure 4 [72] a scheme of a tunneling junction is shown. The tip has a spherical termination of radius R. r_0 is the center of curvature and d the tip-sample distance.

Using Equation 4 and Equation 5 Tersoff and Hamann [72] determine the matrix $M_{\mu\nu}$ and calculate the tunneling current to

$$I_t = 32\pi^3\hbar^{-1}e^2U_B\phi^2D_t(E_F)R^2k^{-4}\exp[2kR]\sum_\nu|\Psi_\nu(\vec{r}_0)|^2\delta(E_\nu - E_F) \tag{7}$$

D_t : density of states per unit probe volume of the probe

The sum in Equation 7 constitutes the local density of states (LDOS) of the sample at the Fermi energy and at the position of the tip. For constant current I_t the tip moves on a surface of constant LDOS. Considering that $|\Psi_\nu(x_0)|^2 \propto \exp[-2k(R+d)]$ in Equation 7 the following relationship between tunneling current, bias voltage and tip sample distance is obtained:

$$I_t \propto U_B e^{-2kd} \tag{8}$$

Hence, the tunneling current I_t is proportional to the bias voltage U_B and depends exponentially on the tip sample distance d. Because of this exponential relationship small changes in the tip-sample separation lead to well measurable changes in the current that allow for a sensitive control of the tip-sample separation with sub-atomic precision.

The precise control of the tip position at a nanometer to sub-nanometer distance to the sample surface makes the STM an ideal tool for the positioning of a near-field tip in a TERS experiment, where

the tip has to be close to the Raman analyte for the enhancement to be effective. Another advantage of using an STM to control the tip position is, that it allows to record topographic images of the same sample that is also probed with TERS. We make use of this option extensively in the experiments described in this work: samples are first characterized with STM before TER spectra are taken.

2.2 RAMAN SPECTROSCOPY

Most of the light that is scattered from a molecule will have the same frequency as before scattering. Only an extremely small part of light will be inelastically scattered, i.e. these photons are shifted in energy by the energies of molecular vibrational excitations. This phenomenon was discovered by Sir Chandrasekhara Venkata Raman 1928 [1–3]. Raman was awarded the Nobel Prize in physics only two years later for this discovery that is named after him the *Raman effect*.

The following paragraphs presents a classical treatment of the light scattering from molecules that is found i.e. in [74].
An external electrical field $\vec{E}$ induces a dipole moment

$$\vec{\mu} = \alpha \vec{E}, \tag{9}$$

in the molecule. Here, the polarizability α describes the extent to which the external field drives the electron density of the sample out of its equilibrium distribution, i.e. the situation without the presence of field E. The polarizability is not a static quantity but may change with the nuclear motion of the molecule as the electronic density adjusts to the momentary nuclear position adiabatically.

The Taylor expansion of the polarizability α around the equilibrium nuclear position Q_0 is written as

$$\alpha = \alpha(Q) + \sum_{q=1}^{N} \left[\left(\frac{\partial \alpha}{\partial q} \right)_{q_0} \cdot q + \frac{1}{2} \left(\frac{\partial^2 \alpha}{\partial q \partial q'} \right)_{q q'} \cdot q \cdot q' + \mathcal{O}\left(q^3\right) \right]. \tag{10}$$

Here, Q is the collection of all normal coordinates q of the system. If the system is moved out of its equilibrium position Q_0 along coordinate q it will perform oscillations that can be approximated as being harmonic with frequency ω_q:

$$q = q_0 \cdot \cos(\omega_q t). \tag{11}$$

For monochromatic radiation the electric field of the incident light can be described by

$$\vec{E} = \vec{E}_0 \cdot \cos(\omega_0 t), \tag{12}$$

with $\vec{E}_0$ the amplitude and ω_0 the oscillation frequency. Truncating Equation 10 after the linear term and inserting it together with Equation 11 and Equation 12 into Equation 9 yields the following form for the induced dipole moment

$$\vec{\mu}(t) = \left[\alpha_0 + \left(\frac{\partial \alpha}{\partial q} \right)_{q_0} \cdot q_0 \cdot \cos(\omega_q t) \right] \cdot \vec{E}_0 \cdot \cos(\omega_0 t). \tag{13}$$

Using the trigonometric expansion of the product of two cosine functions Equation 13 can be written as

$$\begin{aligned}\vec{\mu}(t) =& \alpha_0 \cdot \vec{E}_0 \cdot \cos(\omega_0 t) \\ &+ \frac{1}{2}\left(\frac{\partial\alpha}{\partial q}\right)_{q_0} \cdot q_0 \cdot \vec{E}_0 \cdot \cos[(\omega_0 - \omega_q)t] \\ &+ \frac{1}{2}\left(\frac{\partial\alpha}{\partial q}\right)_{q_0} \cdot q_0 \cdot \vec{E}_0 \cdot \cos[(\omega_0 + \omega_q)t]\,.\end{aligned} \tag{14}$$

The time dependent induced dipole moment will act as a secondary source of radiation. Equation 14 consists of three terms that describe the components of the scattered radiation:

1. The first term produces light at the initial frequency ω_0, i.e. it describes the elastic component of the scattered radiation, an effect called *Rayleigh scattering*.

2. The second term of Equation 14 oscillates with a frequency that is by ω_q smaller than that of the incident laser light. That means that the light produced by this term is red-shifted with respect to the laser and it is called *Stokes scattering*. Via the ω_q dependence the second term of Equation 14 contains information about the vibrational eigenmodes of the system under observation.

3. The last term of Equation 14 behaves almost the same as the second, but the frequency of the scattered light is shifted by ω_q to the blue and is called *anti-Stokes scattering*. In contrast to the Stokes scattering, in anti-Stokes scattering the initial states are vibrationally excited states of the molecule. As the occupation of thermally excited vibrational states follows a Boltzmann distribution the anti-Stokes components are less intense than the Stokes components.

The following considerations will focus on the Stokes component of the scattered light for simplification and because it is the part of the spectrum that is investigated in the experiments described in this work. The corresponding second term of Equation 14 is:

$$\vec{\mu}^{\text{Stokes}}(t) = \frac{1}{2}\left(\frac{\partial\alpha}{\partial q}\right)_{q_0} \cdot q_0 \cdot \vec{E}_0 \cdot \cos[(\omega_0 - \omega_q)t]\,. \tag{15}$$

A *Hertzian dipole* with dipole moment

$$\vec{\mu} = \vec{\mu}_0 \cos[\omega t] \tag{16}$$

emits, integrated over all directions, the average power of

$$\overline{P} = \frac{\overline{\mu^2}\omega^4}{6\pi \cdot \epsilon_0 \cdot c^3}, \tag{17}$$

with the average over an entire oscillation cycle $\overline{\mu^2} = \frac{1}{2}\mu_0^2$. Insertion of Equation 15 into Equation 17 produces

$$\overline{P} = \frac{q_0^2}{48\pi \cdot \epsilon_0 \cdot c^3} \cdot \left(\frac{\partial \alpha}{\partial q}\right)^2_{q_0} \cdot (\omega_0 - \omega_q)^4 \cdot \vec{E}_0^2 \tag{18}$$

for the average power of the Stokes radiation. In Raman experiments, the observed intensity I^{Stokes} is proportional to the average power $\overline{P}$ emitted by the induced Stokes dipole moment. Hence,

$$I^{Stokes} \propto \left(\frac{\partial \alpha}{\partial q}\right)^2_{q_0} \cdot (\omega_0 - \omega_q)^4 \cdot \vec{E}_0^2. \tag{19}$$

Equation 15 and Equation 19 present the central elements of Raman spectroscopy. Equation 15 gives the general form of the inelastically scattered radiation. The Stokes light is produced by a normal mode q of the system at a frequency $\omega_0 - \omega_q$. It is customary to display Raman spectra in intensity over energy $\hbar\omega$. To be able to directly read off the vibrational energies $\hbar\omega_q$ involved, usually a relative energy axes is employed, named *Raman shift*, i.e. the energy of the incident laser radiation minus the energy of the scattered light. Equation 15 also provides the selection rules for Raman scattering. In order to show up in a Raman spectrum, a given normal mode q must have the property that the partial derivative of the polarizability taken at equilibrium position q_0 does not vanish, $\left(\frac{\partial \alpha}{\partial q}\right)_{q_0} \neq 0$. Equation 19 shows the dependence of the Raman intensity on the frequencies ω_0 and ω_q involved and the power of the incident laser E_0^2. The Stokes intensity grows linearly with laser power but with 4th power of the difference frequency $(\omega_0 - \omega_q)$.

2.3 SURFACE- AND TIP-ENHANCED RAMAN SPECTROSCOPY

In the previous two sections two main ingredients of TERS, namely scanning tunneling microscopy and Raman spectroscopy have been considered. In order to make TERS work these two components have to be combined by a common element: an STM tip that also works as a *near-field tip*. The role of the near-field tip in TERS is two-fold. Firstly, it enhances the detected Raman signal by many orders of magnitude. Secondly, the tip allows to measure Raman spectra from a region that can be much smaller than the diffraction limit of the light involved. The fundamental concepts behind these effects will be outlined in this section.

The total cross section for normal Raman scattering of molecules is extremely small; it is in the range of 10^{-31} to $10^{-28}\,cm^2$. Thus, large amounts of sample molecules are needed for a reasonable signal.
In surface science the interaction between molecules and surfaces is of particular interest. That means, (sub)monolayers of molecules adsorbed at surfaces are the desired subject of investigation. For usual Raman spectroscopy however, such coverages mean that maximally 10^5 to 10^9 molecules are located within the focal region. Thus, a monolayer of molecules having a normal Raman cross section of about $10^{-30}\,cm^2$, will produce count rates of Raman photons of less than one count per second. In order to still be able to use Raman spectroscopy in such cases one has to use some kind of enhancement mechanism. One possible mechanism is the *resonance enhancement* of the Raman effect. If the exciting light is tuned into resonance of an electronic transition of the molecule under investigation, the Raman cross section can be augmented by as much as five orders of magnitude [18]. However, not for all molecules of interest it is possible to use this approach of molecular resonances, since many electronic resonances occur in the ultraviolet frequency regime.

Another way to enhance the Raman signals on surfaces is SERS: In the mid 1970s relatively intense Raman signals were discovered by Mc Quillan *et al.* [26] and Fleischmann *et al.* [75] for molecules adsorbed on rough silver electrodes. The authors interpreted the gain in Raman signal as stemming from the enlarged surface area of rough surfaces and, hence, from the increased number of scattering molecules. Jeanmaire and Van Duyne, however, repeated the experiments carefully and calculated the factor by which the normal Raman signal had to be multiplied in order to show the observed intensities [27]. The signal from the rough surface was 10^5 to 10^6 times higher than that expected from a monolayer on a smooth surface. As this gigantic enhancement could not be explained by an increased number of molecules adsorbed on rough surfaces, a new but at that time un-

known surface-enhancement effect had to be the reason.

By now SERS is a widely applied technique in many fields of physics, chemistry and biology. There are two mechanisms involved in SERS: (i) an *electromagnetic* (EM) enhancement effect and (ii) a *chemical* or *first layer* enhancement (CE) effect.

CE in SERS comprises all enhancement mechanisms that are due to the interaction of the molecule with the surface upon adsorption. Only the first layer of molecules on the surface is subject to this group of effects. For SERS substrates that show a large EM enhancement like rough silver or gold surfaces the EM effect is dominant. For transition metal substrates the EM effect is rather low and the chemical enhancement gains ascendancy [76]. One important contribution to the chemical enhancement is the dynamical charge transfer (CT) between molecule and metal substrate that can lead to a resonant Raman scattering. It was first proposed by Burstein *et al.* [77]. Billmann and Otto inferred from electrochemical SERS experiments that the contribution of the CT effect to the total enhancement of Raman signal in SERS is one to two orders of magnitude [78–80]. As for the systems investigated in the current work the EM enhancement mechanism is far more pronounced than a possible chemical one, the chemical enhancement is no further discussed here. Readers interested in learning more about the chemical enhancement are referred to the article by Otto *et al.* in *Topics in Applied Physics: Surface-Enhanced Raman Scattering* [76].

The main effect resulting in SERS is the EM enhancement in the vicinity of metal clusters with a size range between some nanometers and several hundred nano meters. It turns out that this enhancement effect is only present for certain types of metals, most notably gold and silver, but also copper, aluminum, lithium and some others. Gold and silver are in fact the most commonly used materials in SERS. Silver is of advantage when operating with visible light below 600 nm wavelength. For wavelength larger than 600 nm gold has optical properties comparable to silver. In the experiments described in this work gold was used as an "active" material and a laser wavelength of 632.8 nm.

In order to understand the EM enhancement it is illustrative to consider a small metal sphere in an electric field. This sphere then serves as a model for both, a rough surface in conventional SERS and a near-field tip in the case of TERS.

The problem is treated in many textbooks. For example in the textbook by Novotny and Hecht *Principles of Nano-Optics* the authors use an electrostatic approximation to calculate the field distributions in the proximity of an illuminated metal sphere [81]. This approxima-

tion is only suitable if the sphere is much smaller than wavelength λ_0 of the illuminating light ($R << \lambda_0$). In the following the findings of Novotny and Hecht are reproduced:

The dielectric function of the metals sphere is $\epsilon_1(\omega)$ and depends on the frequency ω. The dielectric constant of the surrounding medium, ϵ_2, is assumed to be constant, real and positive. The incoming electric field $\vec{E}_0 = E_0 \cdot \vec{n}_x$ is polarized along the x direction. $\vec{n}_x$ is the unit vector in x direction. For the problem of SERS and TERS only the electric field E outside the sphere is of importance, because in this region the interaction with the Raman scatterer will occur:

$$\vec{E} = E_0 \cdot \vec{n}_x + \frac{\epsilon_1 - \epsilon_2}{\epsilon_1 + 2\epsilon_2} \frac{R^3}{r^3} E_0 \left(2\cos\theta \cdot \vec{n}_r + \sin\theta \cdot \vec{n}_\theta\right). \tag{20}$$

Here, θ and r are the polar angle and radial distance in spherical coordinates (r, θ, ϕ), respectively. $\vec{n}_r$ and $\vec{n}_\theta$ are the unit vectors in the respective directions indicated by their index. The first term in Equation 20 is simply the incoming field $\vec{E}_0$. The second term describes the scattered field. It is the field of a dipole stimulated by the incoming field $\vec{E}_0$ and situated in the center of the sphere,

$$\vec{\mu} = \epsilon_2 \alpha(\omega) \vec{E}_0. \tag{21}$$

Just like in the case of Raman spectroscopy (Section 2.2) α is here the polarizability that describes the response of the electrons inside the sphere to the external field,

$$\alpha(\omega) = 4\pi\epsilon_0 R^3 \frac{\epsilon_1(\omega) - \epsilon_2}{\epsilon_1(\omega) + 2\epsilon_2}. \tag{22}$$

The dependence on the frequency ω is here given explicitly only for ϵ_1 because ϵ_2 is assumed to be constant.

The dielectric constant of the surrounding medium is assumed to be positive and close to one, $\epsilon_2 \approx 1$. The denominator of Equation 20 then becomes zero when $\epsilon_1 = -2$, in which case the polarizability α goes to infinity. Gold and silver are excellent materials for SERS because their dielectric functions $\epsilon_1(\omega)$ meet the resonance condition of Equation 20 for frequencies ω in the visible range of the electromagnetic spectrum, while at the same time the damping of induced oscillations at these frequencies is small in these materials. The quantum of the electronic oscillations associated with the induced dipole moment of Equation 21 and the electromagnetic field oscillations that are coupled to them are called *localized surface plasmon-polaritons* (LSPP). They result in an augmented electric field distribution in the vicinity of the metal particle. A particle that supports LSPP is called plasmonic particle. If E_0 is the field in the absence of the plasmonic particle and E_P the field in its presence then the quotient

$$g = \frac{|E_P|}{|E_0|} \tag{23}$$

is called the local field enhancement. As a consequence of the enhanced electromagnetic field close to the plasmonic particle, a molecule in the vicinity of such a particle is exposed to an enhanced power density $P \propto E_P^2 = g^2 E_0^2$. The inelastically scattered light again couples to the LSPP of the particle and is, hence, also amplified. If I_0 is the intensity of the Raman signal without the particle and I_P the SERS intensity, then the enhancement factor (EF) is defined as the quotient

$$EF := \frac{I_P}{I_0} \propto g^4. \tag{24}$$

The proportionality in Equation 24 is a commonly assumed relation between EF and g [82–85]. This g^4 dependence of the EF is responsible for the enormous signal enhancements in SERS. For a more elaborate discussion of the g^4 behavior of the EF and deviations thereof the interested reader is referred to the discussion of Le Ru and Etchegoin [85].

Even though the example of the small metallic sphere that was just presented is very illustrative and explains the source of the EM effect in SERS, the local field enhancements g_{sphere} for a single sphere are not very high. Much greater values for g are achieved in nanometer sized gaps between coupled plasmonic particles. The EM enhancement can be so high that the detection of single molecule (SM) SERS signals becomes possible [86]. The simplest plasmonic structure with a nanometer gap is a dimer of two metallic spheres.

Le Ru and Etchegoin compare in a recent article [35] the enhancements for a sphere, a dimer and an ellipsoid. The figure 1 of their work [35] is reproduced here as Figure 5. The dimer consists of two silver spheres of 30 nm radius (Figure 5 b)) with a separation of 2 nm; the isolated silver sphere has a radius of 30 nm (Figure 5 a)) and the ellipsoid is an elongated silver nano particle (prolate spheroid, radii 20 and 60 nm, Figure 5 c)). Additional information is noted in the caption of Figure 5 that is also reproduced from the original work, where some symbols were adapted to the nomenclature of this thesis. The maximal EF is here denoted F_{max} and the average over the entire surface of the particle $\langle F \rangle$. A logarithmic false color scale shows the local EF distribution. While for the single sphere the F_{max} is 4.8×10^4, for the elongated particle it is 2.6×10^7 and for the dimer it is 4.9×10^9. The quantity $p(F > F_{max/10})$ gives the percentage of the surface of the respective particle, where the EF F is larger than a tenth of F_{max}; a_{80} is the relative area of the minimal surface on the particle from which 80 % of the SERS signal would originate for a homogeneous coverage of the particle with the Raman analyte. Both these quantities are measures for the localization of the EF.

Not only is the maximal EF five orders of magnitude higher for the dimer than for a single sphere, but at the same time the EF distribution is much more localized for the dimer than for the monomer. Both

the higher F_{max} and the stronger localization are consequences of a coupling of the two spheres constituting the dimer.

In the case of gap-mode TERS the plasmonic tip couples with a plasmonic substrate. This also leads to much stronger enhancements of the Raman signals compared to TERS with substrates that do not show pronounced plasmon resonances [90]. The resolution of TERS is also higher in gap-mode TERS [90].

Downes *et al.* calculated for an Au tip with 20 nm radius at 1 nm distance to an Au surface a lateral resolution of 2.4 nm using a finite element method [91]. Notingher *et al.* [90] compared the resolution for substrates that do or do not support LSPP. The authors determined for an Au tip with 20 nm radius lateral resolutions of 18.5 nm and 8 nm for a glass an Au substrate, respectively. This calculation qualitatively confirms the observation in Figure 5 that the localization of the EF is stronger for the coupled plasmonic structure than for the single sphere. For a combination of Au tip and Au substrate at close distance and in resonance with the exciting laser the localization of the near-field and, hence, the resolution is the highest [90]. The 8 nm resolution in this gap-mode situation for a tip with 20 nm radius is close to the 10 nm resolution calculated by Pettinger *et al.* [39] for the same tip radius.

FIGURE 5 *(facing page)*: Image and image caption reproduced from Ref. [35] with permission. Some of the symbols used in the original image caption are replaced by the respective symbols used in this work.
Examples of calculated enhancement factor (EF) distributions around hot spots for three model surface-enhanced Raman spectroscopy (SERS) substrates immersed in water: (a) a silver sphere (radius 30 nm), (b) a silver dimer of spheres (radius 30 nm, gap 2 nm), and (c) a silver prolate spheroid (radii 20 and 60 nm) representative of elongated or tip-containing nanoparticles. Calculations are performed using Mie theory [87], generalized Mie theory [88], and the T-matrix method [89], respectively. The excitation wavelength is taken at the dipolar localized surface plasmon resonance, which provides the maximum SERS EF. The logarithmic false color maps show graphically the surface SERS EF distribution [in the g^4-approximation [85]]. The plots next to them provide a more quantitative visualization of the hot-spot localization effect, showing the SERS EF in the plane of incidence as a function of arc length, L (along the surface). The most important characteristics of the hot spot are indicated in each case: Maximum SERS EF, F_{max}, surface-averaged SERS EF, $\langle F \rangle$ (over the entire particle), and other hot-spot localization metrics as discussed in the text. These plots demonstrate how extreme the SERS EF distribution can be, especially when large SERS EFs are present. For example, in the case of a dimer, the SERS EF decreases by a factor of 10 for a molecule that is only 5 nm away from the point of the largest EF.

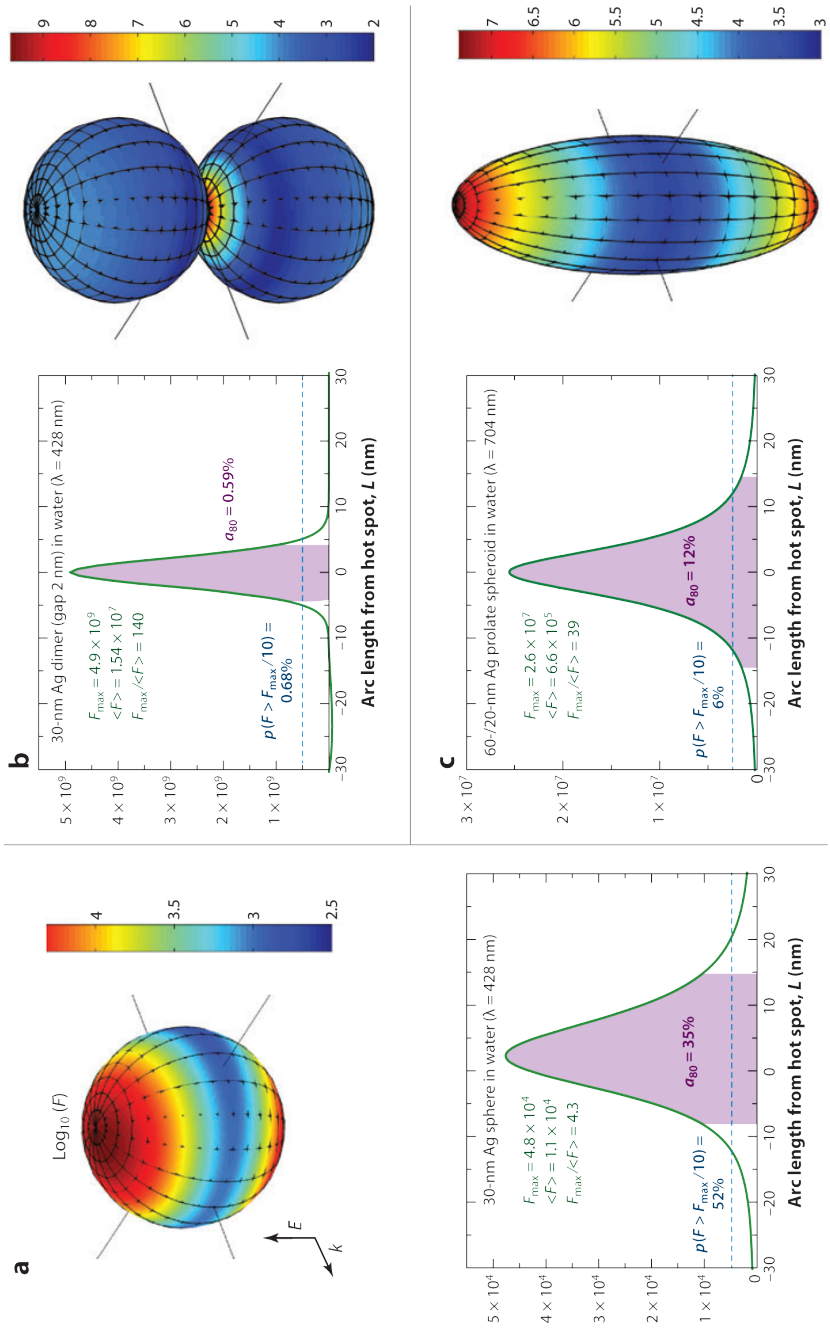
a
Log10 (F)
4
3.5
3
2.5
E
k
b
30-nm Ag dimer (gap 2 nm) in water (λ = 428 nm)
Fmax = 4.9 × 10^9
<F> = 1.54 × 10^7
Fmax/<F> = 140
a80 = 0.59%
p(F > Fmax/10) = 0.68%
Arc length from hot spot, L (nm)
c
60-/20-nm Ag prolate spheroid in water (λ = 704 nm)
Fmax = 2.6 × 10^7
<F> = 6.6 × 10^5
Fmax/<F> = 39
a80 = 12%
p(F > Fmax/10) = 6%
Arc length from hot spot, L (nm)
30-nm Ag sphere in water (λ = 428 nm)
Fmax = 4.8 × 10^4
<F> = 1.1 × 10^4
Fmax/<F> = 4.3
a80 = 35%
p(F > Fmax/10) = 52%
Arc length from hot spot, L (nm)

Hartschuh *et al.* [92] determined the lateral resolution in their experiment with a tip of 15 nm radius to be 20 nm by comparing TERS maps with AFM images of single-walled carbon nanotube (SWCNT) bundles. Stadler *et al.* [93] report a resolution better than 12 nm. These experimental values favor the more conservative theoretical results of Notingher *et al.* [90] and Pettinger *et al.* [39].

The near-field in the vicinity of the metallic tip apex decays rapidly, having a profile analogous to that of an induced dipole and its image dipole. For a homogeneous coverage of the sample surface with Raman analytes Pettinger *et al.* [94] calculate a dependence of the Raman signal on the tenth power of the tip-sample separation (more precisely: $\sim (R_s + d)^{-10}$, where R_s is the radius of a spherical tip apex and d is the gap width between tip and sample). This was verified experimentally for tip-sample distances between 1 and 20 nm, where the intensity of the Raman peaks has dropped by about two orders of magnitude [94, 95]. In Chapter 4 we will show that also smallest changes on the sub-nanometer scale at nm distance lead to remarkable differences in the signal strength of TERS.

3

EXPERIMENTAL

To perform a TERS experiment under UHV conditions an elaborate experimental set-up is required. For such an experiment it is essential to position a plasmonic near-field tip accurately in close proximity to the sample, to illuminate the tip with a laser, to collect the scattered light from the tip-sample junction and to analyze this light spectrally.

The positioning of the tip is performed by a scanning tunneling microscope (STM) and for the analysis of the scattered light a Raman spectrograph is used. The STM and the spectrograph are combined by a set of optical elements that we will, in the following, denote as *Raman detector head* (RDH). The RDH focuses the laser onto the tip-sample junction and collects scattered photons from the same region. Then it guides the inelastically scattered portion of these photons to the spectrograph. For normal Raman experiments often spectrograph units are used where all the elements building the RDH are already built in.

For TERS experiments it is of significant advantage to separate the RDH and the spectrograph constructively. This is because an STM can be more easily combined with a RDH than with the entire Raman spectrograph. While it is already challenging enough to realize this under ambient conditions, the aim to perform the experiment in UHV adds further constructive requirements. Central problems to be solved are, e.g. how to illuminate the tip of the SPM with the excitation laser and how to efficiently collect light that is scattered from the junction between the SPM tip and the sample surface inside a vacuum chamber. To the authors notice, at the moment, there are only a few research groups around the globe that have successfully implemented such an experiment and published UHV-TERS measurements [40, 41, 47–51, 96]. They have addressed this problem in different ways. In this chapter, our experimental set-up and its operation will be described.

The first successful realization of a UHV-TERS experiment was achieved by Jens Steidtner as part of his PhD thesis [40, 47, 96], carried out at the Fritz-Haber-Institute. He was inspired by the experimental set-up of Lieb *et al.* [97] and used a custom made STM with an integrated piezo-controlled parabolic mirror by DME (Danish Micro Engineering). The goal of the original experiment was to realize a

proof of concept of UHV-TERS.

The motivation to perform TERS studies under UHV conditions is the ability to investigate well defined samples such as smooth, crystalline surfaces covered with ordered layers of adsorbates and low levels of contamination. In order to achieve this, it is necessary to prepare samples under UHV conditions, which was not possible with Steidtner's set-up. Instead, samples and tips where prepared under ambient conditions and then transferred into the UHV chamber for measurements.

During the course of my work, Steidtner's set-up was modified significantly. The most significant improvements are listed below:

1. improved control of the sample preparation,
2. higher stability and more functionalities for the scanning tunneling microscope (STM),
3. a faster alignment of the TER optics,
4. reduced laser intensities (below 1 µW) during the focusing of the parabolic mirror,
5. more readjustment possibilities of optics inside the vacuum chamber from outside,
6. improved sensitivity of the detection system and
7. improved preparation of plasmonic near-field tips.

In the following sections the UHV-TERS system will be described in detail.

3.1 VACUUM AND SUPPORT SYSTEM

This section will deal with aspects of the experimental set-up related to vacuum. Furthermore, the support system, i.e. the frame that holds the vacuum chambers and the external vibrational damping systems will be described. Figure 6 and Figure 7 present photographs of the initial experimental set-up and the machine in its current state. Schematic drawings of the set-up are shown in Figure 8 and Figure 9.

Our UHV-TERS system consists of three chambers:

1. the main chamber (MCh), in which the measurements are performed,
2. a load lock (LL) used to transfer samples and tips into and out of the main chamber and
3. a preparation chamber (PCh) that holds all the tools necessary to prepare the sample under UHV conditions.

Load lock and preparation chamber are each connected to the main chamber via the gate valves (GV1 and GV2). All three chambers are mounted onto a frame (F) of aluminium profiles that can be isolated from the floor of the laboratory by two independent vibration isolation systems: an active vibration isolation (AVI) and a pneumatic vibration isolation (PVI).

The main UHV chamber is designed as a sphere of 50 cm diameter, having a number of ports. There are several prominent axes, all running through the center of the sphere and the center of a particular port. Among them are the vertical axis (z) and a first horizontal axis (x). The x-axis connects the load lock (LL) system with the STM and the RDH (more details in Section 3.3). A second horizontal axis (x') runs in an angle of ca. 30° to the first one. Along the x'-axis the sample preparation unit is mounted and connected to the main chamber via a gate valve (GV2) (see Figure 9).

The main chamber contains the STM and the RDH. Both devices were installed on a common platform which in turn is mounted vertically on a DN200CF flange. The whole unit can be moved along the first horizontal axis (x) into and out of the main chamber, guided by a rod that is attached to an external frame construction above the chamber (the crane in Figure 7, not shown in the schematic drawings Figure 8 and Figure 9). Smaller flanges are connected to the flange holding the STM and RDH. They carry the feedthroughs for optical fibers (FPMC and FMM) and electrical wiring for STM and mirror holders.

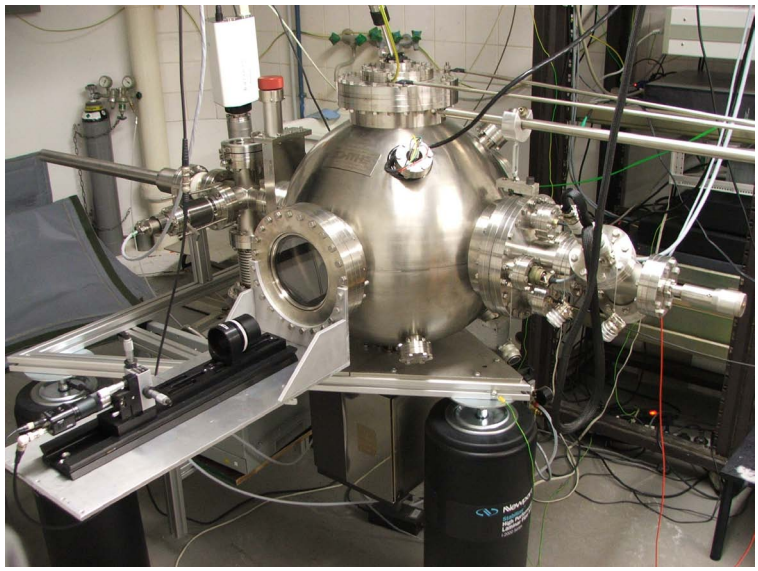

FIGURE 6: Photograph of the original UHV-TERS experiment from Jens Steidtner [96].

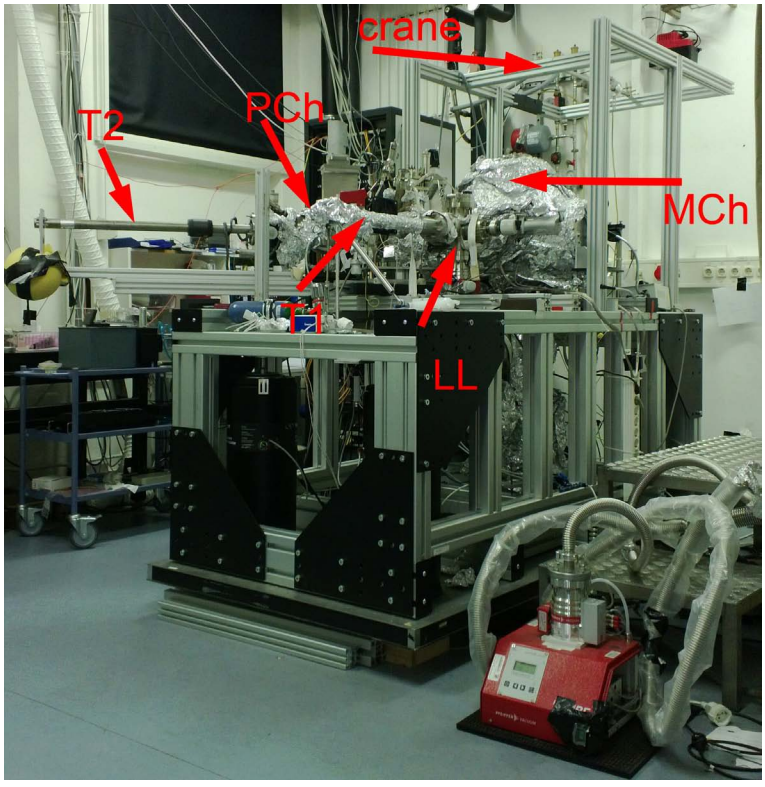

FIGURE 7: Photograph of the current UHV-TERS set-up. Details are given in the schematic drawings Figure 8 and Figure 9. Some important elements are labeled: MCh: main chamber; PCh: preparation chamber; LL: load lock; T1 and T2: transfer rod No. 1 and 2; the crane is used to move the STM and the RDH out of the MCh for maintenance.

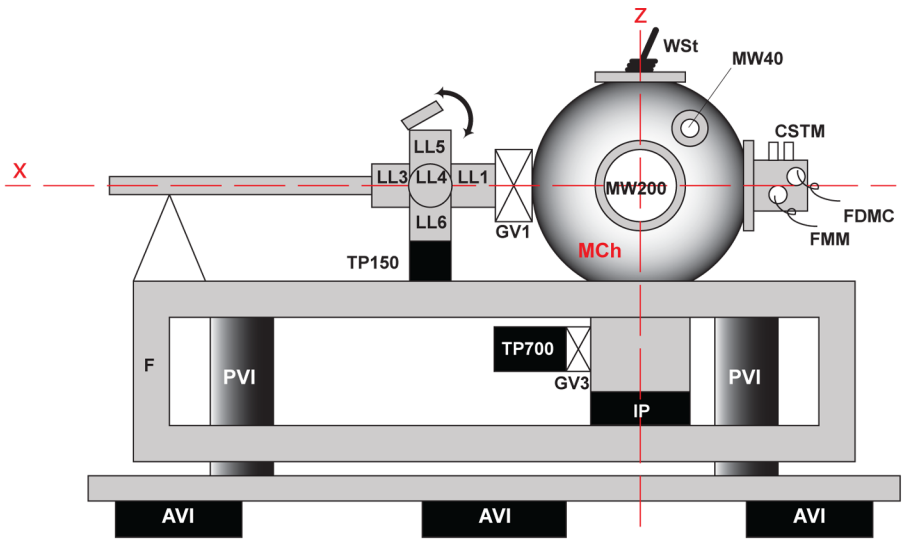

FIGURE 8: Schematic drawing of the UHV-TERS set-up. Side view. The individual parts are labeled: AVI: active vibrational isolation; PVI: pneumatic vibrational isolation; F: frame of aluminum profiles; IP: ion getter pump; TP700: turbo molecular pump; GV1: gate valve No. 1; GV3: gate valve No. 3; LL1-LL6: load lock ports 1-6; TP150: turbo molecular pump; MCh: main chamber; WSt: wobble stick; MW200: CF200 window; CSTM: connectors for STM; FMM: vacuum feedthrough for multimode fiber; FPMC: vacuum feedthrough for polarization maintaining fiber; T1: transfer rod No.1; red dashed lines show the main axes x and z.

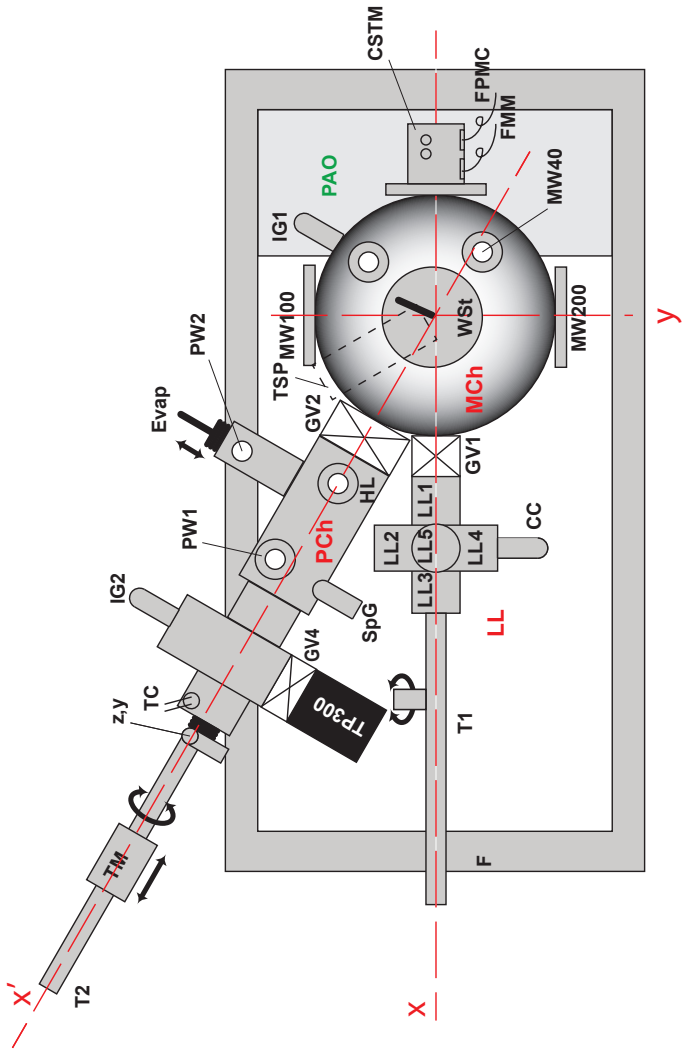

FIGURE 9: Schematic drawing of the UHV-TERS set-up. Top view. The individual parts are labeled: TP300: turbo molecular pump; GV1: gate valve No 1; GV2: gate valve No 2; LL1-LL6: load lock ports 1-6; CC: cold cathode pressure gauge; MCh: main chamber; WSt: wobble stick; MW200: CF200 window; MW100: CF100 window; MW 40: CF40 window; CSTM: connectors for STM; FMM: vacuum feedthrough for multimode fiber; FPMC: vacuum feedthrough for polarization maintaining fiber; IG1: ion gauge No.1; PCh: preparation chamber; HL: halogen lamp for sample heating; SpG: Sputter gun; PW1: window; PW2: window; Evap: evaporator; GV4: gate valve No. 4; IG2: ion gauge No. 2; TC: thermocouple connectors; TM: transfer magnet for movement of the sample along and rotation around the x′ axes; PAO: platform holding the external alignment optics; T1: transfer rod No.1; T2: transfer rod No. 2; TSP: titanium sublimation pump; red dashed lines show the main axes x, y and x′; z′ and y′: translation stage in the two directions perpendicular to the x′-axis.

Along the vertical axis (z) a cylindrical chamber is mounted from below to the main chamber via a DN200CF flange, which in addition carries a turbo molecular pump (TP700), an ion getter pump (IP) and a titanium sublimation pump (TSP). In order to avoid that vibrations of the TP700 disturb STM and TERS experiments, a gate valve (GV3) in between the main chamber and the TP700 has to be closed and the TP700 has to be shut down during the measurements. Then only the IP pumps the main chamber.

Along the same vertical axis, but on top of the chamber, a wobble stick (WSt) is mounted. It is used to move the sample around inside the chamber and has a travel of 165 mm, an angular range of 45° and can be rotated by 360°.

A fourth axis (y) is oriented perpendicular to both the vertical (z) and the first horizontal (x) axis. Along the y-axis there are ports to which a DN200CF flange (MW200) and a DN100CF flange (MW100) are mounted; both flanges are equipped with windows providing visual access during the sample transfer from and to the load lock and the preparation chamber. A smaller window (MW40) in 45° to the x-axis and 45° upwards serves the same purpose. Through the largest window (MW200), light can be coupled out of the RDH into the alignment optics that is placed outside the chambers.

The pressure in the main chamber is measured with a Bayard-Alpert ion gauge (IG1) from ALM. The pressure during measurements was in the low 10^{-9} mbar range. A quadrupole mass spectrometer (QMS) is located between the ion gauge (IG1) and the wobble stick (WSt). It is used for analysis of the residual gas in the chamber and for leak checking.

The load lock (LL) consists of a DN63CF six-way cross piece (ports LL1 - LL6). It is connected to the main chamber, opposite the flange holding the optical platform with the STM on the x-axis.

A gate valve (GV1, between LL1 and the MCh) separates the two chambers. The load lock is pumped with a turbo molecular pump (TP150) located underneath LL6. The upwards facing flange (LL5) allows fast access for sample and tip exchange via a Viton sealed lid. A cold cathode ionization gauge (CC) is used to measure the pressure.

After the load lock has been vented with nitrogen and a new sample and/or a new tip has been inserted, it is pumped down into the low 10^{-6} mbar pressure range within half an hour before the tip or the sample is transferred into the main chamber.

On the port LL3, located opposite LL1, the linear transfer rod (T1) is mounted. The sample carrier on its head can carry two samples and one tip, allowing them to be moved between LL and MCh.

Preparation chamber: In order to carry out UHV-experiments it is essential that samples are prepared under UHV conditions. For the original set-up this possibility was not envisaged. During the course of this thesis a *preparation chamber* (PCh) was constructed and installed. It allows to prepare crystals by Ar^+ sputter-cleaning, annealing and the evaporation of molecules (such as C_{60} molecules) onto the surface.

The preparation chamber is a cylindrical piece and is connected to the main chamber via another DN63CF in an 30° angle (x′) to the main axes defined by the transfer rod of the load lock (x-axis). A gate valve (GV2) separates the main and the preparation chamber and is closed during the sample preparation. It is opened for sample transfer between the two chambers and during the measurements. The gate valve to the turbo molecular pump (TP300) that pumps the preparation chamber is then closed and the pump (TP300) is shut down to avoid vibrations. The preparation chamber is pumped during the measurements via the main chamber by the ion getter pump (IP). A separate ion gauge (IG2) is used to measure the pressure in the preparation chamber.

The sample holder with the sample is connected to a transfer rod (T2) that can be moved along x′ and rotated by 360°. In addition, using a translation stage (z′,y′), the rod can be moved in two directions perpendicular to x′ by a few centimeters. In that way the sample can be moved towards different preparation instruments described below.

Thermocouple wires attached to the transfer rod connect the thermocouple pins (see design of the sample holder in Figure 14) of the sample holder to a thermocouple feedthrough (TC) at the end of the chamber. An external voltmeter is connected to the TC allowing to monitor the temperature of the sample during the preparation procedures.

To exchange the sample between the main chamber and the preparation chamber, the transfer rod T2 is moved through the open gate valve into the main chamber where the sample holder can be picked up with the wobble stick (WSt).

A halogen heating lamp (HL) (Osram, XENOPHOT, HLX 64635, 150W, 15V) is connected to one top flange of the preparation chamber on the vacuum end of a linear transfer. For heating, the sample is moved into the focus of the lamp and the heating power is controlled

by means of an electrical power supply.

Another flange on top of the chamber is equipped with a sputter gun (SpG), to which an argon gas cylinder is connected via a leak valve. The optimal position for the sample for sputtering is determined by visual inspection of the light emission from the sputter focus. For the sputtering the sample is moved to the focus of the sputter gun. The ion current that flows between sample and sputter gun is measured with an ampere meter connected between the chamber ground and the thermocouple (TC) at the vacuum feedthrough.

A Knudsen cell filled with C_{60} is used as an evaporator (Evap) for the molecules. The evaporator is mounted on yet another linear transfer on a flange opposite of the load lock. To dose C_{60} molecules onto the sample, the evaporator is preheated to 240 °C, while the surface of the sample is rotated in the opposite direction and moved as far away as possible from the evaporator along x′. Once the evaporator has reached the desired temperature, the sample is positioned in front of the evaporator with a distance of 10 cm and the surface facing towards the molecule source.

Clean Au(111) surfaces are prepared by repeated cycles of sputtering (30 min at 2×10^{-5} mbar Ar pressure, 1.5 kV and 6 µA) and annealing of the crystal (10 min at 400 °C). C_{60} molecules are dosed at a constant temperature of ~ 240 °C. The degree of surface coverage is controlled by the evaporation time and inspected using the STM.

3.2 THE SCANNING TUNNELING MICROSCOPE

The scanning tunneling microscope (STM) together with the positioning system of the parabolic mirror is custom made from DME (Danish Micro Engineering A/S, Denmark). It is designed in such a way that the tip is inserted into the scanner from the rear side. The scanner itself is located behind the parabolic mirror, such that the tip protrudes into the curved part of the mirror. Figure 10 is a drawing of the mirror with the tip holder and tip.

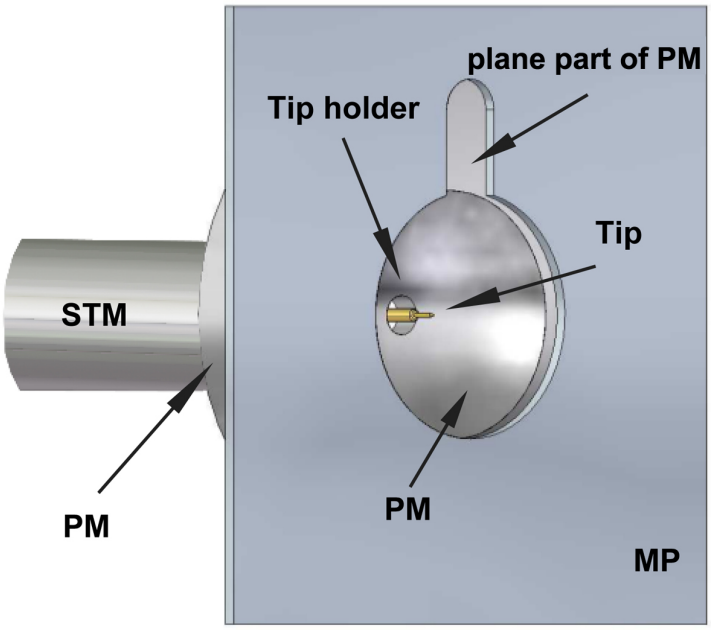

FIGURE 10: Drawing of the parabolic mirror with tip. Through a hole along the mirror axis the tip in the tip holder protrudes into the curved part of the mirror. A metal plate covers most of the flat rim of the mirror. Only a small section of the rim is visible at the top.

During the course of my PhD the STM scanner was replaced once. We worked in close collaboration with DME to adjust the parameters of the new STM until a coarse approach of the tip towards the sample did no longer damage tip and sample.

The electronics of the STM were also upgraded to a newer version of the DME controller (C-26, including new software: Scan Tool). The operator has now more options to control the device. Many functions of the STM can be automated with the help of user-programmed scripts. We have developed several programs, including one which is used to clean the tip by applying a sequence of voltage pulses. An-

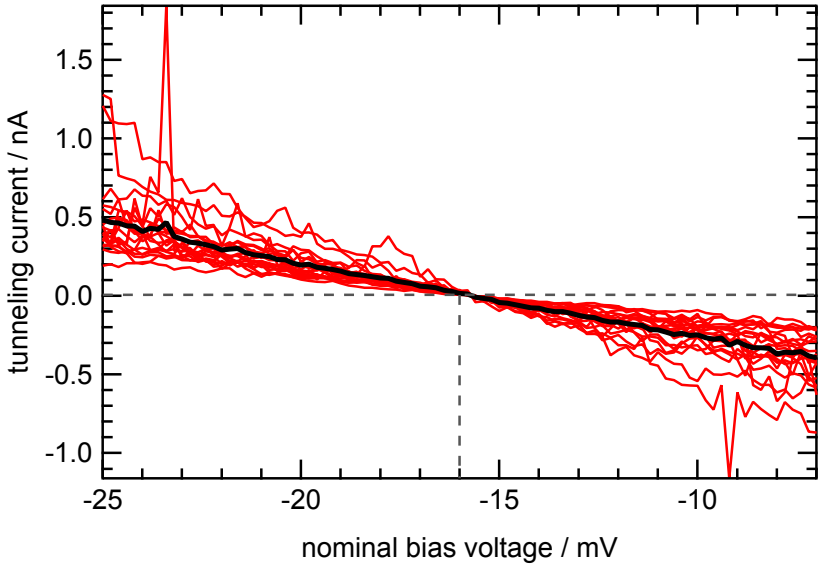

FIGURE 11: Determination of the zero of bias voltage. The voltage was scanned up and down between −25 mV and −6 mV in increments of 0.2 mV resulting in the 20 red traces. An average is given in black. The offset in bias voltage is determined to −16 mV.

other of these programs can be employed to compensate for a drift between tip and sample during the scanning; a third program measures current voltage curves. For the voltage dependent measurements presented in Section 4.3 it is important to know the zero point of the bias voltage accurately. For this purpose, current-voltage curves are recorded. The location of the physical zero of the bias is where the tunneling current crosses the zero-current line. Figure 11 shows such a measurement. The nominal value of the zero bias voltage is −16 mV. The bias voltages reported in this work are corrected for this small value if they are in the 10 mV range where the difference is of crucial importance.

Another feature of the upgraded version of the STM controller is the option to switch off the feedback loop and move the tip in all tree directions using the software interface. This is important for the focusing procedure (to be described in Section 3.3), because it allows to retract the tip from the surface without involvement of the coarse approach piezo motor. This feature of the controller is also employed to move between different parts of the scan area without actually scanning the surface. These and several other features of the new software were implemented by DME on our request.

All STM images in this thesis are constant current images, i.e. during the horizontal scan of the tip over the surface the tip hight is

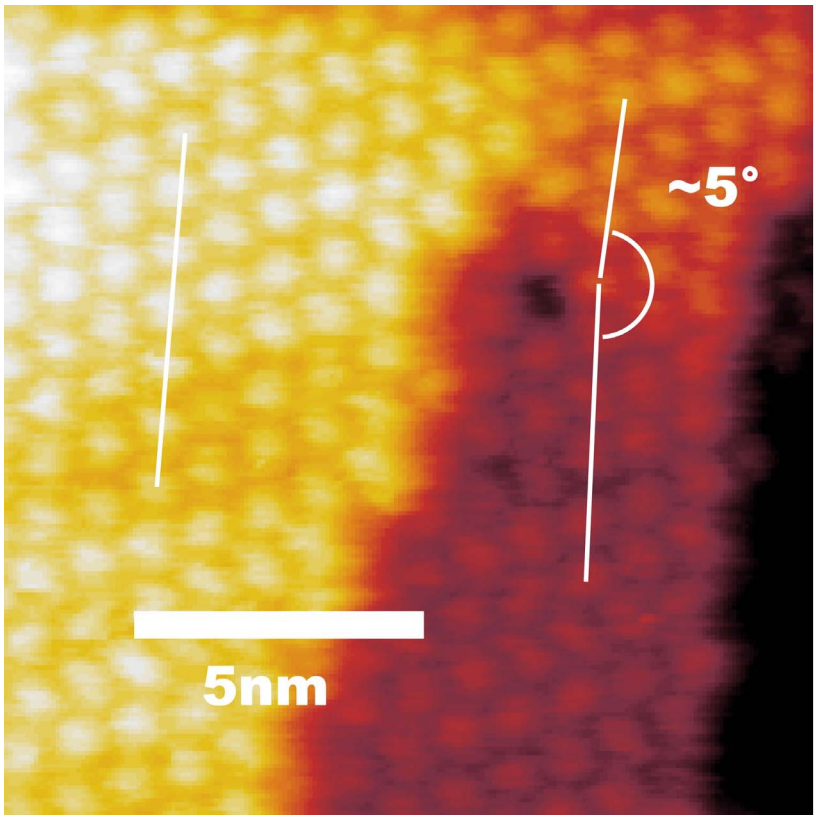

FIGURE 12: C_{60} monolayer on a screw dislocation of a Au(111) surface. The typical hexagonal pattern of the molecular layer is clearly visible on three terraces. The right terrace appears mainly in black to improve contrast for the other two that cover most of the area shown. Tunneling conditions: $U_B = -2\,V$, $I_t = 0.1\,nA$.

regulated in order to keep the tunneling current constant. The constant current mode is also employed during TERS experiments, unless stated otherwise. An example of a calibrated and drift corrected STM image is presented in Figure 12. It shows a monolayer of C_{60} grown in the well known [66, 67] closed packed hexagonal structure on an Au(111) surface exhibiting a screw dislocation. A C_{60} molecule is missing in the layer close to the vertex. The film is distorted in the vicinity of the vacancy. Two white lines mark rows of neighboring molecules to the right of the defect and comprise an angle of about 5°. For comparison, a third white line on the left hand side of the image shows a region with no defect. More STM images are presented in Chapter 4.

The sample holder plays a crucial role in the experiment because its design must ensure several functional properties, namely: a) keeping the sample in place during the experiment, b) transferring the sample from air into UHV and vice versa, c) transferring the sample between preparation and measurement chambers, d) allowing the illumination of sample and tip and the collection of scattered light, e) reading the sample temperature during the preparation process. These features and functions of the sample holder will be described in the following.

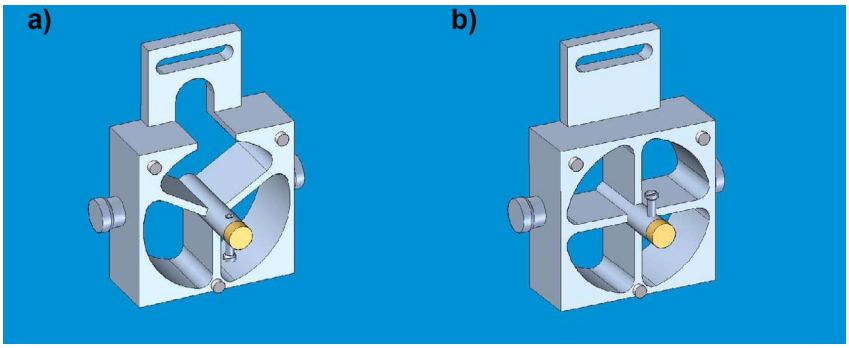

FIGURE 13: Previous designs of sample holders. a) design by Jens Steidtner. As compared to the original design, b), there are only three instead of four bars in the light path and there is an extra aperture to allow light to pass to the plane part of the parabolic mirror. This reflex is a crucial mean for focusing the parabolic mirror. Image adapted from [96] with kind permission of Jens Steidtner.

The sample holder was originally delivered by the company DME as part of the UHV-TERS system. A drawing of the original design is shown in Figure 13b). Three ceramic disks in front of the sample holder and two small metallic cylinders on its sides are used to keep the sample in place inside the STM. In addition, the sample holder has a handle on top. With the aid of this handle and of the wobble stick (WSt), the sample holder can be held and moved around inside the main vacuum chamber (MCh). For example, it can be picked up from the sample transfer rod and placed inside the STM for measurements. While the bias voltage U_B is applied to the sample via the metal body of the sample holder the three ceramic discs insulate the sample electrically against the rest of the set-up.

Two main changes were made in the design of the sample holder by Jens Steidtner when he set up the first version of the UHV-TERS system. His sample holder is displayed in Figure 13a). First, an extra aperture was cut into the body of the holder. This permits to illuminate a part of the plane mirror rim of the parabolic mirror. The resulting light reflex plays an important role for the focusing procedure of the parabolic mirror. The second modification was the replacement of the four bars by three to get a larger aperture for light collection.

As part of this thesis work the sample holder was improved considerably (see Figure 14). In the new construction of the sample holder, the three ceramic discs are replaced by small screws with ceramic ends. By turning the screws in and out, they serve two adjustment purposes.

First, the three ceramic discs define the two angles between the sample surface and the scanning plane of the STM. Figure 15 shows the situation of the sample holder facing toward the parabolic mirror (PM). A metal plate in front of the PM is fixed parallel to the scan plane of the STM. The ceramic spacers are in contact with this plane thus defining the angles between STM and sample planes.

Second, the distance between the side cylinders and the plane defined by the ceramic discs determines the vertical position of the sample relative to the PM. This distance has to be chosen in such a way that the sample surface is positioned in the focal area of the parabolic mirror.

As the focal point is located inside the arching of the mirror (the opening angle of the mirror is larger than 90°, see Figure 15) the sample has to reach into the bow. This necessity explains why the sample is mounted on a small, central tube. This tube is connected to the body of the holder by three thin bars. Although this tube as well as the thin bars are obstacles in the light path, this construction permits the collection of a large fraction of the scattered light by the parabolic mirror (NA~1) *and* to reflect a great part of it backwards where it is collected for spectral analysis.

The angle between sample surface and scan plane should be as small as possible for two reasons: a) to minimize the slope in the STM image; this holds especially for scanning larger areas, where a steep slope means the z-piezo may reach its limits. b) to minimize the slope between the sample plane and the xy-plane of the PM. This is important and time saving for the optics adjustment procedure, because less refocusing has to be done after the focus of the PM is moved onto the tip-sample junction.

Two tools where designed to find the optimal position for the three screws before the sample holder with the gold crystal is inserted into the UHV system. The first tool helps to adjust the angles between the plane defined by the ceramic ends of the screws and the sample surface (see appendix Section A.1). The second tool simulates the case of the sample inside the STM and is used to find its correct vertical position with respect to the parabolic mirror (see appendix Section A.1).

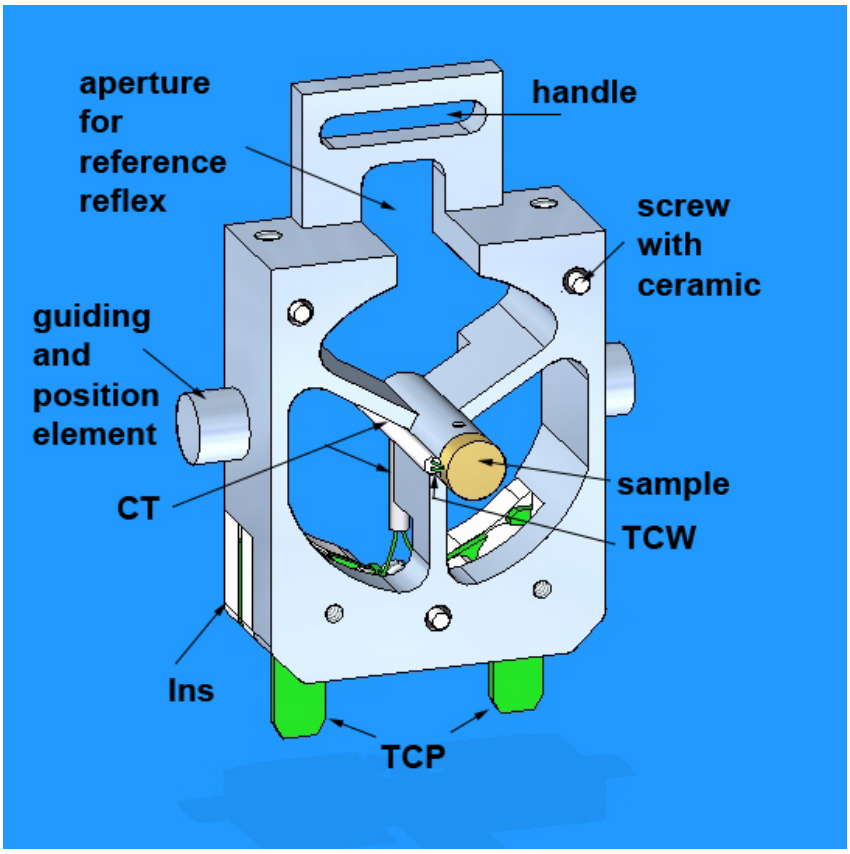

FIGURE 14: New design of the sample holder. Important elements are labeled. Abbreviations are: CT - ceramic tube, TCW - thermocouple wire (chromel and alumel respectively), Ins - Insulators and TCP - thermocouple plug.

Another improvement of the sample holder is related to the sample preparation. In order to have an good control over the cleanliness of a surface, it needs to be prepared under UHV conditions. To that end a preparation chamber was attached to the set-up. A detailed description of the design and functionality of the preparation chamber was given above. In order to clean crystal surfaces they are repeatedly sputtered with Ar ions and annealed. The sputtering current and the sample temperature have to be monitored during these operations. The temperatures are measured using a thermocouple.

A wire each of chromel and alumel are spot welded together at one end, which is the point where the temperature is measured. This contact is inserted in a 0.3 mm bore at the side of the crystal. The wires are insulated from each other and from the body of the sample holder and then guided in an aluminium oxide double tube along the side of the metal tube holding the sample. On the backside of the sample holder the wires are each spot welded to a metal plug (TCP) of the

same respective material. The plugs are insulated from the metal part of the sample holder by ceramics. In the preparation chamber these plugs are connected to matching sockets on the head of the transfer rod. From there, thermocouple wires are guided to a flange and fed through (see CT in Figure 9) to the air side of the chamber. By measuring the voltage between the external wires the temperature of the sample inside the preparation chamber can be determined. In the case of sputtering, the thermocouple wires are used to monitor the current that flows between sputter gun and sample.

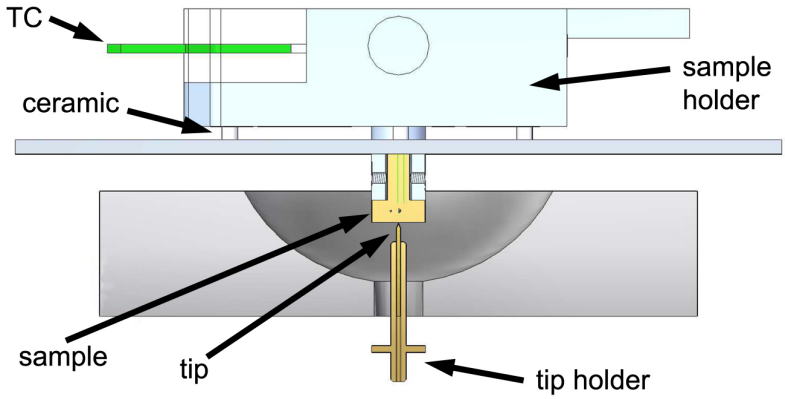

FIGURE 15: Arrangement of tip, parabolic mirror, sample, the metal reference plane and the new sample holder. The lower part of the image represents a cut through sample, tip-holder and PM.

The sample - an Au crystal with an (111) oriented surface - has a mushroom shape (Figure 15). Its head is cylindrical with a diameter of 3.5 mm and a hight of 1.5 mm. The little shaft is a rod of 1.7 mm diameter and 3 mm hight. This sample is inserted into the central tube of the sample holder and tightened by two M1 screws. Due to the smallness of the arrangement the angle between the plane defined by the three ceramic discs and the sample surface can not be adjusted with a high accuracy when fixing the crystal on the holder.

The tip holder was also delivered with the UHV-STM by DME. Originally, it consisted of a tube with an outer diameter of 1 mm, an inner diameter of 0.5 mm and a length of 10 mm that was pressed into the central hole of a disc of 0.5 mm thickness and a diameter of 3 mm (see Figure 15). The tips etched from 0.25 mm diameter Au wire were attached by kinking the wire twice and clamping it into the tube. Such a procedure creates wires with their final tip ends usually being off center. For the scanning and recording of STM images, this does not pose a problem. However, for focusing light onto the tip by our particular parabolic mirror set-up it is required to mount and fix the tip along the central axis of the tip holder. For this purpose, new tip

holders were produced with an inner diameter of 0.3 mm. The wire of 0.25 mm diameter with the sharp tip end can thus be affixed centrally on the holder axis.

3.3 UHV-COMPATIBLE RAMAN DETECTION SYSTEM

As already explained earlier, TERS is a combination of an SPM (in our case an STM) with a Raman experiment. The light of the laser used in this scattering experiment has to be focused onto the tip-sample junction and the scattered light has to be collected and anlysed by a spectrograph.

The current experiment is performed under UHV conditions. Consequently, the sample and the tip and, hence, the STM are located inside an UHV chamber. The illuminating laser and the spectrograph, on the other hand, are placed outside the chamber. So the laser beam has to be guided into the UHV chamber and the scattered light out of the chamber to the spectrograph.

To collect as many of the scattered photons as possible, a high numerical aperture (NA) focussing element has to be used. In the current case this is an on-axis parabolic mirror (PM) with an opening angle of slightly over 90° that is located between STM scanner and sample (see Figure 10 and Figure 15). Through a hole in the mirror, the STM tip is approached to the sample. The focusing of the mirror onto the sample is accomplished by controlling the two tilt angles and the distance to the sample with three piezo-motors. With two further piezo-motors the mirror can be moved along the surface plane of the sample to position the focus on the tip-sample junction. The mirror is not only employed for the collection of scattered photons, but also to focus the laser onto the tip for the excitation of TER scattering. The big advantage of this PM over a lens objective is, that with the PM almost all scattered photons (apart from a small fraction that is blocked by the sample holder, see Figure 14 and Figure 15) are collected.

For vibrational isolation (additional to the two elements described above), the STM is suspended with springs. There is, hence, no stable relation between the unit of the STM with the PM and the two elements, laser and spectrograph, outside the chamber. In order to focus the incoming light optimally and guide the scattered light onto the entrance slit of the spectrograph, such a stable relation has to be established. This is achieved by guiding the laser light into and the scattered light out of the chamber with optical fibers. The vacuum ends of the fibers are then fixed in relation to STM and PM. A number of other optical elements are placed in the UHV chamber. Their

function is described below.

The entire optics inside the chamber - denoted *Raman detection head* (RDH) in the following - is mounted onto a platform in form of a stainless steal plate that is firmly attached to the STM and suspended by springs for vibrational damping. A scheme of the optical set-up is depicted in Figure 16 and will be explained in the following.

A helium neon (HeNe) laser with 632.8 nm wavelength and a power of about 13 mW is used as a light source, which is positioned outside the chamber on an optical table. The laser defines the starting point of the optical path through the whole set-up. The endpoint is a spectrograph located outside the UHV chamber, a Shamrock 303 form L.O.T.-Oriel with an Andor Newton EMCCD detector (A-DU971N-BV).

After passing through an electro-mechanical shutter, the laser is coupled into a polarization maintaining single mode fiber (PMC1) with 4.4 µm fiber core and a numerical aperture (NA) of 0.12. The fiber is connected to an attenuator (At) (Schäfter+Kirchhoff) and then re-coupled into a polarization maintaining fiber (PMC2). This fiber passes through a Viton sealed vacuum feed-trough in a DN40CF flange into the UHV chamber. An identical feed-trough guides a multimode (MM) fiber (MM1) that carries the optical signal scattered by the sample from the UHV to the spectrometer.

On the bottom side of the platform there are two collimators with 100 mm focal length. They produce collimated beams of 25 mm diameter. A Dove prism is mounted in front of each collimator. The prisms optically connect the bottom with the upper side of the platform (Note that the prisms are not shown in the schematic drawing Figure 16. Instead the beam collimators are drawn on the upper side of the platform, for simplification). That means the incident laser beam is sent from the bottom to the upper part of the optical platform and vice versa for the scattered light beam. This construction allows to exploit the limited space in the main chamber effectively by using both sides of the platform.

The next element in the beam path after C1 is a laser line filter (LF). It cleans the beam spectrally from plasma lines of the HeNe laser and possible Raman and fluorescence light from the fiber. For this reasons it has to be placed on the UHV side, after the laser light has passed through PMC1.

Up to this point the polarization of the beam is linear and perpendicularly oriented with respect to the platform. However, such a con-

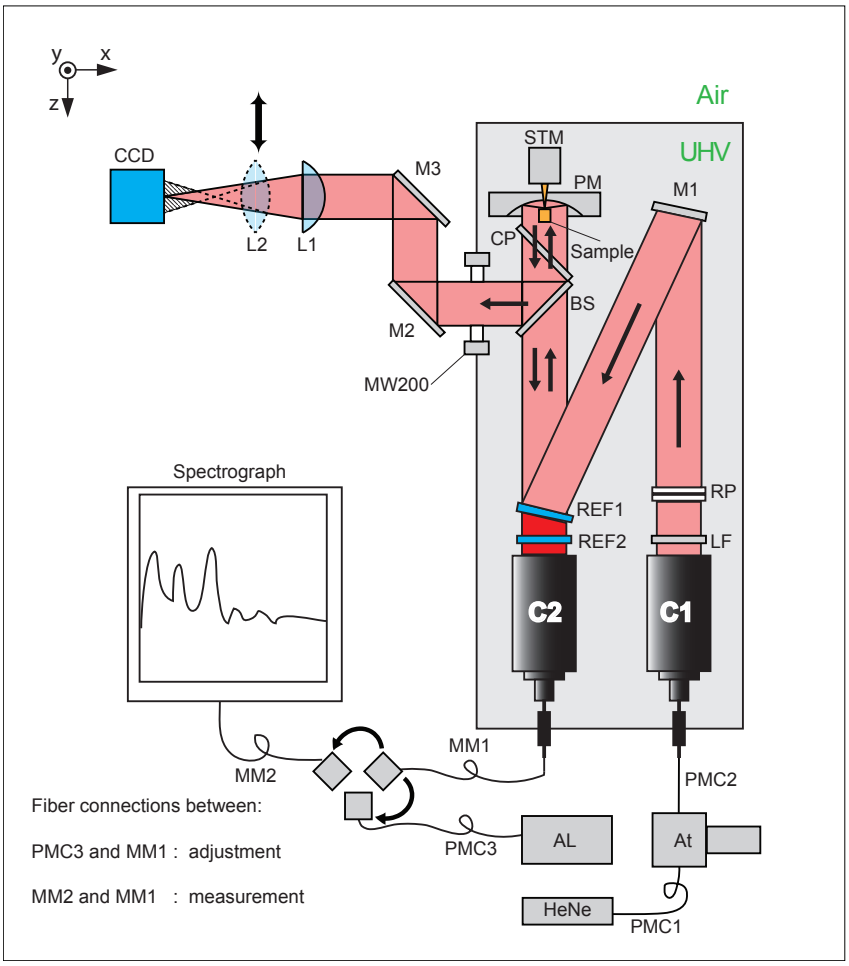

FIGURE 16: Schematic drawing of the Raman set-up. The grey box represents the main vacuum chamber. It contains the optical elements of the Raman detector head (RDH) and the STM. In the upper left part of the scheme the alignment optics are shown. In the lower part of the scheme the lasers and the fiber connections are drawn. The multimode fiber (MM1) of collimator (C2) is connected to the adjustment laser (AL) during the alignment and to the spectrograph during the measurements. Individual elements are labeled as: STM: scanning tunneling microscope; PM: parabolic mirror; CP: compensation plate, BS: beamsplitter ; M1-3: mirror No. 1-3; REF1 and 2: Raman edge filter No. 1 and 2; LF: laser line filter; RP: quasi-radial polarizer; C1 and 2: collimator No. 1 and 2; HeNe: Helium-Neon-laser; At: laser attenuator; PMC1-3 polarization maintaining fiber No. 1-3; AL: alignment laser; MM1 and 2: multimode fiber No. 1 and 2; L1 and 2: lens No. 1 and 2; CCD: alignment CCD (charge-coupled device) camera.

figuration breaks the rotational symmetry not only of the beam, but also of the PM, the sample and the tip and, thus, must have some impact on the size, shape and intensity distributions in the focal region. For optimal focussing, the desired polarization is a radial polarization

of the incident laser beam. In this experiment a so-called quasi-radial polarization is used, as an approximation to the radial polarization. For that purpose, a four-segmented polarization retarder (RP) is employed. Its mode of operation and the resulting polarization is depicted schematically in Figure 17.

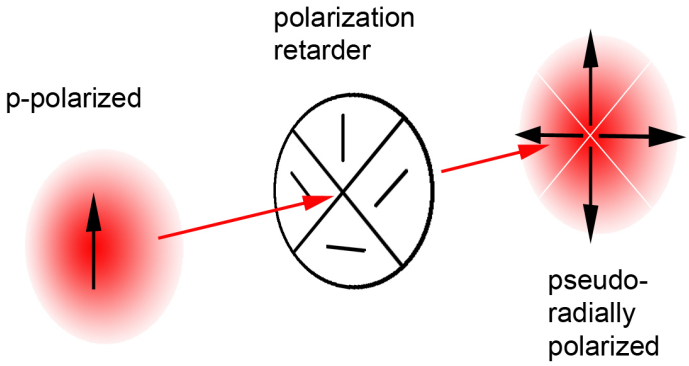

FIGURE 17: Mode of operation of the quasi-radial polarizer (RP). Red discs symbolize a cut through the propagating laser beam. Black arrows show the orientation of the field strength at a particular plane perpendicular to the direction of propagation (red arrows). The black short lines on each segment of the polarization retarder indicate the fast direction of the respective $\lambda/2$-plate.

The initially linear and up-wards directed polarization is altered locally within the beam by each of four $\lambda/2$ plates.; i.e., the laser beam is then segmented into four quarters. The black short lines on each segment of the polarization retarder indicate the respective fast direction of the element.Each quarter of the beam exhibits still linear polarization, but it is spatially rotated by 90° relative to that of the neighboring quarters. The resulting polarization is called quasi-radial, because it is composed of a finite number of segments with the field vector pointing in the radial direction of the beam. In a radial polarization the electric field vector points at each position of the beam in the radial direction. Because the incident beam arrives with quasi-radial symmetry at the sample surface and forms the focus, a strong electromagnetic field is created inside the focus that is mainly oriented perpendicular to the sample surface and parallel to the near-field tip. This provides, an excellent excitation configuration of plasmonic modes of the tip and is, therefore, particularly suitable for TERS.

Figure 18 is a scheme of the focusing of radially polarized light with a high NA parabolic mirror. Sample and tip are plotted in yellow. Red arrows indicate the direction of propagation of the laser beam. The

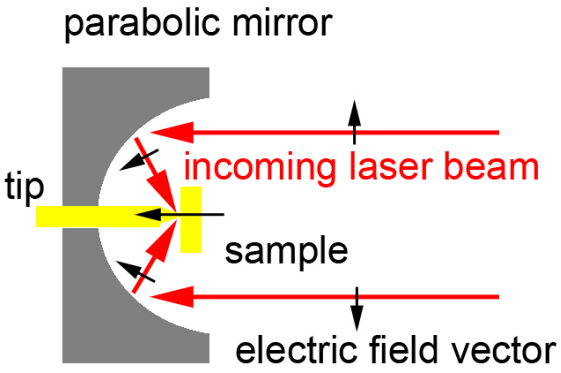

FIGURE 18: Focussing of radially polarized light with a parabolic mirror. A cut along the axis of the parabolic mirror is depicted. Red arrows show the direction of propagation of the laser beam. Black arrows represent the electric field strength at particular positions.

black arrows show the orientation of the electric field strength at the respective point in space. The resulting polarization of the focus on the sample is parallel to the tip.

The next optical elements after RP, denoted as M1 and REF1 are at this stage both acting as mirrors. They are mounted on piezo controlled mirror mounts. Using these elements, the quasi-radially polarized beam is directed towards the parabolic mirror. The employment of piezo controlled mounts represents a considerable improvement over the original set-up where no motorized mounts were used. The UHV system has to be baked at temperatures above 100 °C to obtain low pressures. The precise alignment of optics can easily be lost after the chamber has cooled down again. The piezo motors allow to compensate for misalignments after the bake-out. The possibility to realign these optical elements from outside the chamber can save a lot of time, because it avoids the breaking of the vacuum and a repeated bake-out of the chamber.

The beam splitter (BS) and the compensation plate (CP) are employed in the adjustment procedure and will be described in the next section.

For the remaining part of the explanation of the optical set-up we assume that the central axis of the parabolic mirror is oriented parallel to that of the incoming beam. Furthermore, we assume that the focus of the mirror is located in the surface plane of the sample.

Because of the quasi-radial polarization of the incoming beam, the main component of the electrical field in the focus is parallel to the mirror axis and perpendicular to the sample surface, see Figure 18.

This is the optimal illumination condition to couple the light to the tip that acts as an optical antenna [81] and creates an intense near-field between tip apex and sample surface. A detailed account of this is given, i.g. in the doctoral thesis of Andreas Lieb [98] and in ref. [97].

The light is reflected from the sample and travels back to the parabolic mirror from where it leaves as a collimated beam along the mirror axes. It travels back until it reaches the Raman edge filter.

If a tip is positioned inside the focus in tunneling contact with the sample, and if there are Raman scatterers underneath the tip, enhanced inelastic light scattering (i.e. TERS) can occur. The scattered light is then collected by the parabolic mirror, in addition to the reflected light.

The fraction of the light that is red-shifted passes through the Raman edge filter without major losses. From the light at the original wavelength only a very small fraction is transmitted. The transmitted light will be filtered further by a second Raman edge filter (REF2) (i.e. the laser content is further reduced) and the second collimator passes it into the MM fiber (MM1). On the air side the MM1 is connected to another MM fiber (MM2), which is attached to the entrance optics of the spectrometer. This consists of a fiber connector and a lens to match the NA of the spectrometer. The light spot on the entrance slit of the spectrometer has a width of 100 µm. The spectrograph disperses and focusses the multichromatic light onto different pixels of the EMCCD chip.

Alignment of the optical set-up. So far, the optical set-up was described in its aligned configuration. In order to establish the alignment, all the components have to be positioned accurately.

For the alignment further auxiliary elements are needed. An additional laser (AL) at 670 nm is employed as a reference beam. It is coupled via the optical fibers PMC3 and MM1 to the collimator C2. The wavelength is chosen to be close to that of the Raman laser, but red-shifted to such an extent that it passes through the Raman edge filters (REF1 and REF2).

A part of the beams (i.e. the reference beam from C2 and the Raman laser from C1), that is reflected from the PM, is coupled out of the vacuum chamber by a beamsplitter (BS). It is guided by three mirrors (only two are depicted here: M2 and M3) onto lenses (L1 and L2) and from there onto a CCD chip. The intensity pattern on this camera is employed to find the correct positions of the adjustable optical elements. The entire procedure involves many steps and is described

in more detail in the appendix Section A.2. In the following, a brief summary is presented.

As a first step, the optical axis of the parabolic mirror is positioned to coincide with the axis of the reference beam from C2. For that purpose the reference beam is focused by the parabolic mirror onto the sample surface. This ensures, that later on the inelastically scattered light is efficiently coupled by C2 into the multi mode fiber MM1. In the next step, the HeNe laser beam from C1 is aligned with the reference beam from C2 by moving the piezo controlled mirror M1 and Raman edge filter REF1. As a consequence,, the illuminating HeNe laser is now also focused onto the sample. In this configuration (once MM1 is disconnected from PMC3 and reconnected to MM2) already normal Raman and fluorescence experiments can be performed. To conduct TERS experiments a near-field tip made of gold is approached to the sample by the scanner of the STM. By moving the PM along the two directions perpendicular to the beam axis, the focus of the incident laser is centered around the tip. The last step that is needed before TER spectra can be recorded is connecting the MM1 to MM2 (and, hence, disconnecting it from PMC3). Further details of the alignment are given in the appendix Section A.2.

Near-field tips for TERS. The tips that are used in TERS experiments have to fulfill a number of criteria that exceed the ones for standard STM tips. In Section 2.3 the general idea behind TERS was presented. One of the main features of a TERS tip is that photons from the incoming laser can efficiently excite surface plasmon polaritons (SPP) of the tip, which are localized in a small volume near the tip apex and the sample surface. These SPPs are then scattered inelastically by nearby molecules. These inelastically scattered SPPs radiate as photons, which can then be collected, detected and analyzed. For an effective excitation and high localization of SPPs the material and the shape of the tip has to be properly chosen. As material gold is employed in our experiments because it supports such optical processes, especially in the red and near infra-red part of the electromagnetic spectrum, where the frequencies of our HeNe laser and of the Stokes scattered light are located. The shape of the tips is fabricated by electrochemical etching of gold wires with a concentrated HCl/Ethanol solution. The exact procedure as well as some modifications thereof is presented in the appendix Section A.3.

Figure 19 shows three SEM (scanning electron microscope) images of a suitable tip. The tip has a smooth surface and especially the last 2 µm show an almost perfect conical shape that ends in a hemisphere of about 20 nm radius. The smooth surface ensures that no disturbing SERS signals are to be expected from the shank. The only "nano-

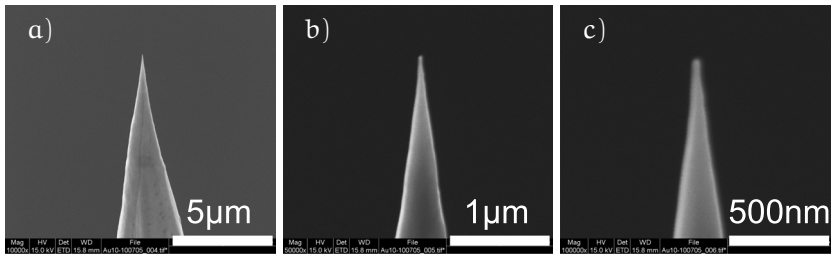

FIGURE 19: Three SEM images of a tip etched from Au wire in different magnifications. The last 10 µm, a), of the tip have a very smooth surface. Especially the last 2 µm shown in b) form a almost perfect cone. From the highest resolution image, c), the radius of the tip is determined to 20 nm. The same images together with images on larger scale are presented in Figure 59. I want to thank G. Weinberg and W. Frandsen for the acquisition of all the SEM images presented in this work.

particle" on the tip is its apex. As the polarization in the focus of the illuminating laser is chosen to be parallel to the tip axis, the incident photons can efficiently couple to SPPs, which concentrate at the tip apex and, hence, produce a strong near-field in its surrounding.

4

RESULTS

In this work we have studied the vibronic properties of C_{60} at Au(111) by gap-mode TERS experiments. Figure 20 shows the molecular structure of C_{60}. It has a rather small Raman cross-section of $d\sigma/d\Omega = 7.2 \times 10^{-29}\,cm^2\,sr^{-1}$ [62] [1] at the wavelength (632.8 nm) of our HeNe laser. To the best of our knowledge all reports of TERS under UHV conditions existing so far refer to experiments with molecules exhibiting a large resonance Raman (RR) effect and having, hence, a large cross-section already without an additional surface enhancement [40, 48, 50, 51]. In the UHV-TERS studies of Steidtner *et al.*, for example, the dye molecule brilliant cresyl blue (BCB) was used as Raman scatterer [40]. RR cross-section values for this molecule are not available in the literature. But BCB closely resembles the dye molecule Nile Blue (NB), both in structure and in optical absorption properties [99]. It is, hence, a reasonable assumption that they will also exhibit comparable RR cross-sections. NB has a differential RR cross-section of $2.2 \times 10^{-24}\,cm^2\,sr^{-1}$ [18]. That means the Raman cross-section of the dyes at resonance is about 3×10^4 times higher than the one of C_{60} under our experimental conditions.

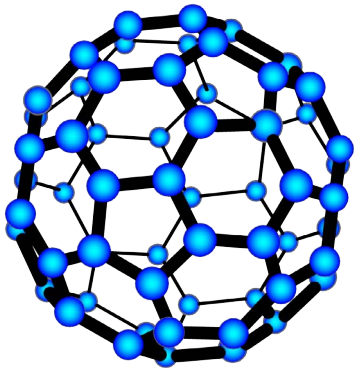

FIGURE 20: Structure of a C_{60} molecule. Image adapted from ref. [53]

1 This value of $d\sigma/d\Omega = 7.2 \times 10^{-29}\,cm^2\,sr^{-1}$ is experimentally determined in ref. [62] for the $A_g(2)$ mode of C_{60} at $1469\,cm^{-1}$. In the same article also a theoretical value of $d\sigma/d\Omega = 9.6 \times 10^{-30}\,cm^2\,sr^{-1}$ is given based on DFT calculations. The fact that the theoretical value is roughly a factor of seven smaller than the experimental one is explained by a mild pre-resonance Raman effect that is not accounted for in the calculations.

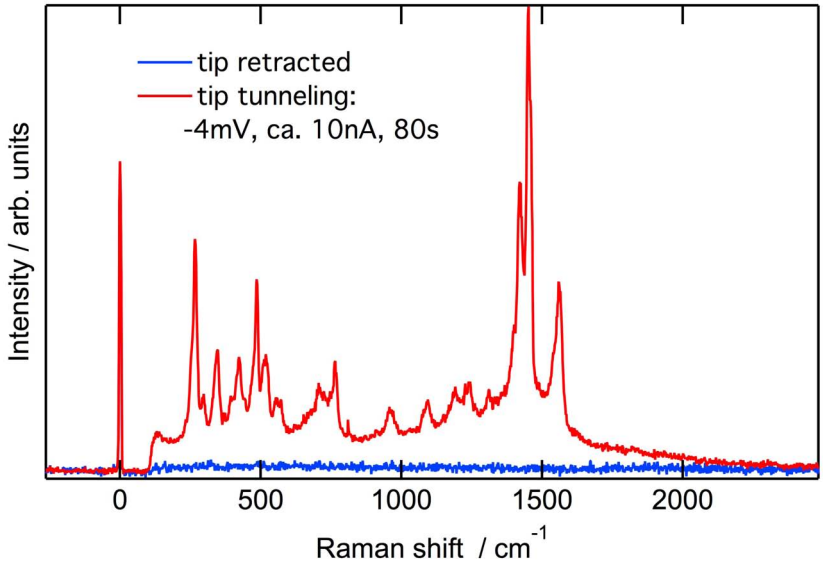

FIGURE 21: TER spectrum of C_{60} on Au(111). The blue trace shows a spectrum when the near-field tip is retracted from the surface. In the red trace the tip is in tunneling distance of the sample (ca. 1 nm). The integration times are 30 s and 80 s respectively for the blue and the red trace. The spectra are normalized to the laser lines at zero Raman shift. Tunneling conditions during recording the red trace: $U_B = -4\,mV$, $I_t \sim 10\,nA$. The tunneling current is only approximated, because in the presented case the feedback of the STM was switched off.

In this context the first important result of this work is that UHV-TERS can be performed even for sub-monolayer coverages of C_{60} on Au(111). A TER spectrum of C_{60} adsorbed at Au(111) is presented in Figure 21. The spectrum is taken on a sample with low coverage of C_{60} like that shown in the STM image Figure 22 a). The lower trace in Figure 21 shows a spectrum acquired when the tip is retracted from the surface. Apart from the laser line at zero Raman shift only a broad and very weak background is visible. The upper trace (red) shows a spectrum for a tip that is in tunneling distance to the surface. It exhibits a set of TER lines with high intensities and the overall spectral pattern resembles a normal Raman spectrum of C_{60} [53], as will be illustrated below. The spectra of (sub)monolayers of C_{60} that are presented here cover the full spectral window between $200\,cm^{-1}$ and $1600\,cm^{-1}$ of first order Rama features [41]. [2]

The motivation to use a Raman scatterer that does not exhibit a resonance enhancement and to operate in an UHV environment in our experiments is the following. It is of interest to make the TERS technique applicable to a large set of Raman scatterers, in order to investigate their interactions with surfaces by measuring their vibrational

2 Earlier TER studies on C_{60} refer to undefined C_{60} adlayers and show only smaller spectral clips. None of them are performed under UHV conditions [32, 63–65]

spectra on a small scale. Most of the molecules in question will not show a resonance enhancement. Even if they do, once more than one species is under investigation in the same experiment it is unlikely that their electronic resonances overlap and not all of them would benefit from a resonance enhancement equally well. In addition, in TERS experiments the laser frequency and the plasmonic material of the tip (and possibly sample) are chosen in a way that the laser is within the plasmonic spectrum of the tip. Hence, in most of the implementations of TERS experiments the laser frequency is fixed. In order to make additionally use of a resonance Raman enhancement one has to choose the Raman scatterer so that its electronic resonance includes the laser frequency. This is often done in TERS experiments by choosing appropriate dye molecules, but restricts the set of possible analytes tremendously. However, when using non-resonant molecules in TERS experiments, the role of contaminating molecules becomes more pronounced as compared to the case of resonant molecules. This is because the Raman cross-section and, hence, the TER spectra of such impurities can become comparable or larger than the ones of the molecules under investigation. It becomes, hence, more important to have a good control over the cleanliness of the sample. Our approach is to conduct both, sample preparation and TERS experiments, under UHV conditions to minimize contaminations. Additionally, working in an UHV environment insures that reactive molecules, e.g. oxygen are absent during the experiment. The presence of oxygen is known to lead to a faster photo-degradation in certain TERS experiments [40].

The STM images in Figure 22 illustrate nicely the main features of two different cases of sub-monolayer coverages of C_{60} on Au(111).

The growth of C_{60} on Au(111) has been studied extensively in a series of papers by Altman and Colton [66–68]. At low concentration of C_{60} on the surface the molecules first adsorb at step edges, preferentially first at fcc sites of the reconstructed surface before the hcp sites are populated [66]. This leads to a dashed pattern like that seen in the central and lower left regions of Figure 22 a). With growing surface density of molecules the gaps in the decoration of the step edges are filled like in the lower part of Figure 22 a). Eventually two-dimensional islands start to grow away from the step edges onto the gold terraces. Where two steps come close, a formation of islands is favored [67], as also observable in Figure 22 a) inside the red circle labeled B. Panels b) and c) present the same STM data in two different contrast settings to focus on different features of the image. In the lower left corner of panel b) large islands of C_{60} are seen to cover a series of steps completely with a dense layer. The central part of the image is almost free of molecules with a small number of exceptions. Figure 22 c) focuses on the Au(111) surface in the central part of the

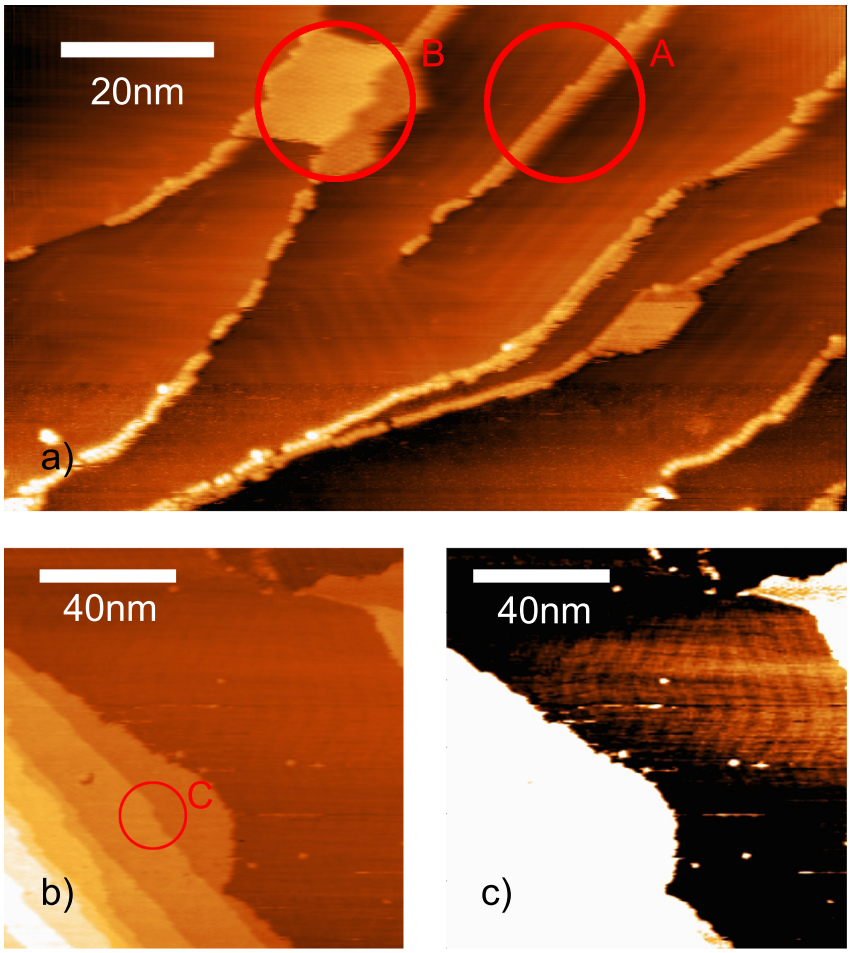

FIGURE 22: STM images of an Au(111) sample with a low (a) and high (b and c) coverage of C_{60} molecules, where c) is the same image as b) but exhibits the image data with higher contrast to improve the visibility of the Herringbone structure of an uncovered Au(111) terrace. Tunneling conditions for all images: $U_B = -2\,V$, $I_t = 0.07\,nA$

image. The well known $(22 \times \sqrt{3})$ surface reconstruction of Au(111) is clearly present, indicating a clean surface. Only in some places, especially at kinks in the reconstruction, individual molecules or small clusters appear as white spots.

Assuming a tip radius of $r_{tip} = 20\,nm$, the area from which the TERS signal originates has a radius of $r_{TERS} \sim 10\,nm$ [39]. In Figure 22 three areas of this size are indicated with red circles. The TERS enhancement factor (EF, see Equation 24 in Section 2.3 for definition) can be estimated from the TERS intensity, the intensity of the Raman background, the focus area and the TERS area [39]. As no Raman signal is detectable in the background (see blue trace in Figure 21) the noise level of the background spectrum serves as upper limit for the

background Raman signal. The focus radius is assumed to be 150 nm based on measurements conducted by Jens Steidtner [47, 96]. Using these numbers a lower limit for the TERS EF is calculated to be 3000. This is two to three orders of magnitude lower than the highest EF (1.6×10^6) reported with the old version of the experimental set-up under similar experimental conditions for the dye molecule *brilliant cresyl blue* (BCB) [96]. The last statement does, however, not mean at all that the actual enhancement factor in our current experiment is worse than in previous measurements. The Raman cross-section of BCB is about 3×10^4 times higher than that of C_{60}. In a TERS area like B or C in Figure 22 there are about 200 to 300 C_{60} molecules, in the case of area A even only about 40 (the distance between two neighboring C_{60} molecules is ~1 nm in the islands). That means detecting a (sub)monolayer of C_{60} could correspond to a 100 fold higher sensitivity than that needed for the detection of a single molecule of BCB [40, 96].

However, it is also possible that the resonance enhancement and electromagnetic (EM, see Section 2.3) enhancement do not combine strictly multiplicatively. For example the resonance Raman effect could experience some quenching in analogy to the quenching of fluorescence of molecules adsorbed on metals. In this case, the value of four orders of magnitude for the expected quotient of TERS signal intensities of BCB and C_{60} would have to be reduced. Even if a factor of 100 is lost due to some quenching of the resonance Raman effect, the EF in our C_{60} experiments would be still of comparable magnitude as the EF ~ 1.6×10^6 reported for BCB by Jens Steidtner [40, 96].

The rest of this chapter is organized in the following way. First, the main features of a C_{60} TER spectrum are discussed and compared to Raman spectra of C_{60} from the literature in Section 4.1. Section 4.2 then describes the way the data were collected and analyzed. The response of TER spectra of C_{60} on variations of external parameters is discussed in Section 4.3. Section 4.4 deals with the spectra of different surface coverages and degrees of polymerization of C_{60} on Au(111). Section 4.5 focuses on experiments where STM images and TER spectra were acquired from the same spatial region.

4.1 GENERAL FEATURES IN TER SPECTRA OF C_{60} ON Au(111)

In this section the main features in TER spectra of C_{60} on Au(111) are discussed.

The steep edge at about 110 cm^{-1} in the spectrum in Figure 21 results from the two Raman edge filters (see Section 3.3) that suppress light at higher energies (including in particular the laser line, yet this line remains still present in the spectra and, thus, serves as a marker for the zero position). Between 240 cm^{-1} and 1580 cm^{-1} about 20 TER peaks and shoulders are seen that will be discussed in the following.

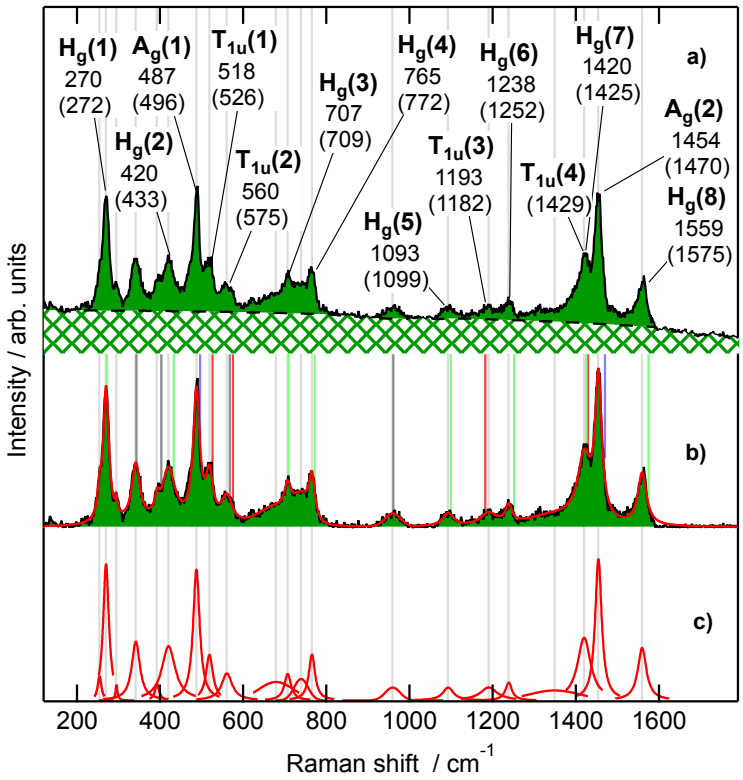

FIGURE 23: TER spectrum of C_{60} on Au(111) with peak assignment. a) Spectrum (full green) with background (green checked pattern). Tags give the group theoretical names of irreducible representations of the full icosaeder group I_h. b) Spectrum with the background subtracted (black trace and green filling) and fitted curve as sum of the peaks in c) (red trace). c) Fitted peaks. Light grey vertical lines mark the fitted peak positions. The colored vertical lines in b) indicate peak positions of isolated C_{60} from [100]. Blue lines correspond to Raman active A_g modes, green lines to Raman active H_g modes and red lines to T_{1u} modes that are IR active. Dark grey lines indicate some of the "silent" modes that are not optically active for isolated C_{60}.

Figure 23 shows another TER spectrum of C_{60} on Au(111) to discuss the main features. In panel a) the recorded spectrum is given as black trace. The black dashed line and the green checked pattern represent the background of the spectrum that was determined by employing an R routine [101]. A broad and relative intense background signal (ranging from 20 % to more than 100 % of the maximal TERS peak intensity) is a well known and characteristic feature of SER spectra in general and in TERS in particular, while in normal Raman spectra such a background is absent. The origin of the background in SERS and TERS is still under debate [102–104]. One possible source for the background could be a remnant of fluorescence.

To improve the visibility of the spectral features in Figure 23 they are colored in full green, while the background is shown by a green checked pattern. The symmetry group of an unperturbed C_{60} molecule is the full icosaheder group I_h. On this basis, the group theoretical names of irreducible representations of the I_h group are assigned to the peaks in tags, instead of the actual reduced symmetry of adsorbed C_{60} which is unknown. This correlation is justified, because most of the observed vibrational frequencies are very close to those reported for isolated C_{60} molecules. For convenient comparison, these labels also contain the position of the fitted peaks and in brackets below the corresponding values for isolated C_{60} from a publication of Menendez and Page [100] that we take as a reference. Isolated C_{60} has ten Raman active modes. These are two totally symmetric A_g modes ($A_g(1)$ and $A_g(2)$) and eight fivefold degenerate H_g ($H_g(1)$ through $H_g(8)$). Further four modes are infrared (IR) active: $T_{1u}(1)$ through $T_{1u}(4)$. These are each threefold degenerate.

A C_{60} molecule consists of 60 carbon atoms and has, hence, 180 degrees of freedom. Accounting for three translations and three rotations this leaves 174 vibrational degrees of freedom. Because of the degeneracies resulting from the high symmetry these correspond to only 46 distinct vibrational modes. Only the 14 modes mentioned above are optically active. The remaining 32 vibrations are not observed in first order IR or Raman spectra and are, therefore, often called "silent" modes. However, the original symmetry can be reduced, for example for a C_{60} crystal, for a C_{60} sample containing ^{13}C atoms [3] or for C_{60} molecules that are adsorbed on a surface. In such cases some of the "silent" modes can become Raman active. The same holds for modes that are - in the I_h symmetry - IR active, they can become Raman active when the symmetry is reduced. A reduced symmetry can also result in the splitting of degenerate modes.

3 Because of the natural abundance of ~ 1.1 % of ^{13}C, 34.7 % of C_{60} molecules contain a single ^{13}C atom and another 11.2 % contain two [62].

Panel b) shows the spectrum with the background subtracted (black trace and green filling) and a fit- curve as sum of the individual peaks in c) (red trace). The colored vertical lines indicate peak positions from ref. [100]. Blue lines correspond to Raman active A_g modes, green lines to Raman active H_g modes and red lines to T_{1u} modes that are IR active. Dark grey lines indicate some of the "silent" modes. In panel c) the fitted peaks are displayed.

As TERS is operating on the nanoscale, a number of experimental parameters are not (much) under control, such as the tip quality and possible contaminations on the tip. Although, the experiments are performed under UHV conditions, some degree of contamination of the surface can also not be excluded. Unless stated otherwise, the experiments presented in this work are performed without knowledge of the exact amount and arrangement of C_{60} molecules during the TERS measurements, because in the majority of experiments no STM measurements were performed of the same sample location. Rather, the sample was characterized before the TERS measurement by STM, in order to establish the amount of C_{60} molecules and the composition of the C_{60} layer. Exceptions to this are discussed in Section 4.5, where STM images and TER spectra are correlated.

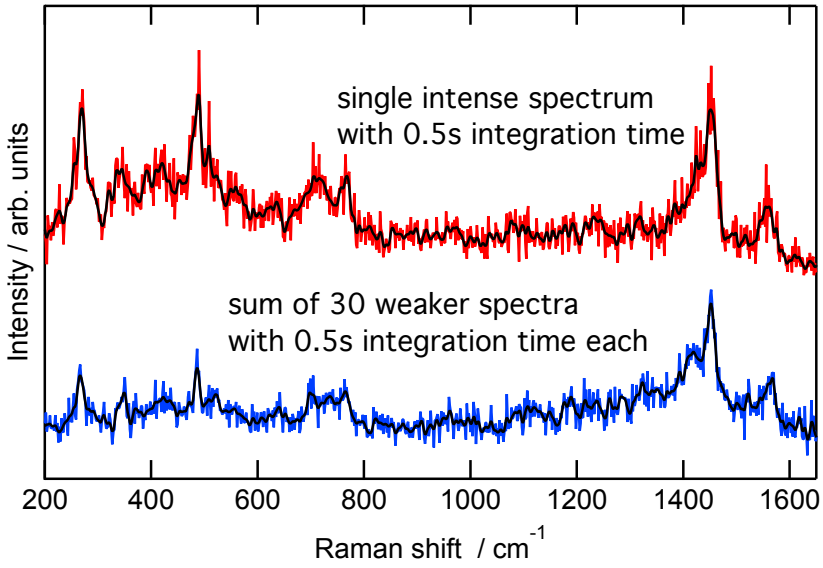

FIGURE 24: A single intense TER spectrum next to the sum of thirty weaker spectra. The red trace is offset vertically for clarity.

It is also difficult to determine the exact position of the near-field tip in relation to the focus. This is an issue intrinsic to the current experimental set-up, where the relative position between focus and tip is not locked during the relative movement between sample and

tip. It is, hence, difficult to determine the exact laser power density at the tip location.

Because of all the uncertainties described above, the measured TER intensities span a large range from being undetectable even with several minutes integration time to being intense enough to show all the major Raman bands in 0.5 s. An example of an intense spectrum taken with 0.5 s integration time is shown in Figure 24 next to a sum of 30 consecutive weak spectra.

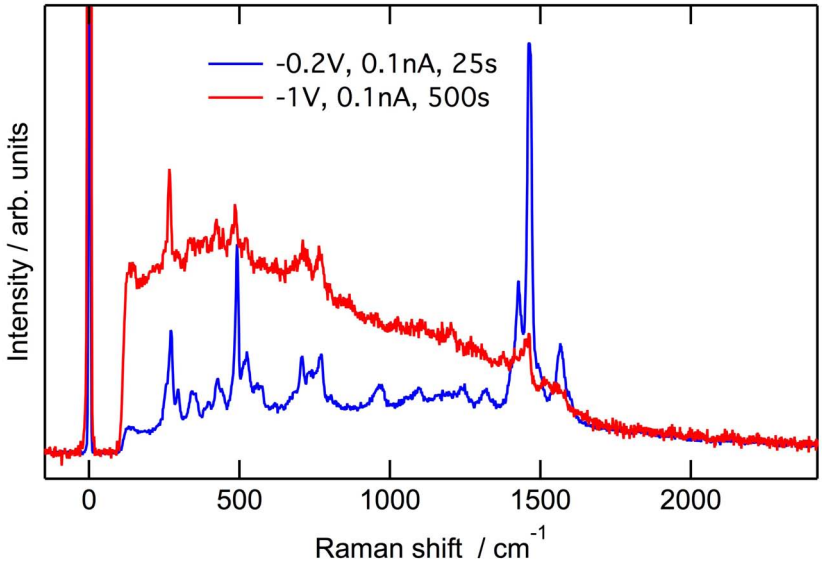

FIGURE 25: Two TER spectra from two different samples with high coverages (about half a monolayes) of C_{60} on Au(111). The two spectra are normalized to the intensity of the lowest TERS peak at 260 cm^{-1} to facilitate the comparison. Bias voltage, tunneling current and integration time are given in the legend. Data presented here and in Figure 21 are acquired each with a different tip on a different sample.

Figure 25 shows two more TER spectra of C_{60} on Au(111). Both spectra are acquired from samples with a high coverage of C_{60} of about half a monolayer. Different tips and different samples are used in each of the two experiments and the one reported in Figure 21. While the tunneling parameters during the experiment in Figure 21 are with a bias voltage of $U_B = -4\,mV$ and a tunneling current of about $I_t = 10\,nA$ rather exotic, the spectra in Figure 25 are recorded under conditions that are common also for the acquisition of STM images. For better comparability the two spectra in Figure 25 are normalized to the intensity of the lowest TERS peak at 260 cm^{-1}. The blue trace was recorded in 25 s. It is very similar to the spectrum in Figure 21: the background is rather broad and flat and the peaks

are much more intense than the background. For the red trace on the other hand, a much higher integration time of 500 s was needed. Here, the background peaks at lower Raman shifts of around 400 cm^{-1}. The background reflects the localized surface plasmon-polariton (LSPP, see Section 2.3) spectrum of the tip. This also explains the reduced relative intensities of the TERS peaks at higher Raman shifts in the red compared to the blue spectrum. The LSPPs of the tip-sample combination are responsible for the EM enhancement effect behind TERS (see Section 2.3). The spectrum of these LSPPs defines the dependence of the EM enhancement on energy and, hence, the relative intensities in TER spectra. In general we observe a high variation of absolute and relative intensities in the TERS spectra for different tips.

Contaminations on both the surface and the tip can also produce strong TER signals that may become equal or higher in intensity or even stronger than the spectra of adsorbed C_{60} aimed for. Finally, for various reasons C_{60} molecules might degrade and show altered spectra. Simple averaging or increasing the integration time would result in spectra that contain all such contributions. To exclude the undesired signals as much as possible, the following routine was employed: I) recording a time series of spectra with an integration time of 0.5 s each and a number of 100 to 1000 subsequent spectra (see the next section for some examples). II) Visual inspection to identify regions of temporal stability as well as regions containing foreign peaks. III) Only stable sequences that show all the main TERS bands of C_{60} are averaged over to gain a higher signal to noise ratio.

All TER spectra presented so far where acquired with this method. An average of all stable spectra exhibiting C_{60} characteristics, that we recorded at various samples with many different tips, is presented in Figure 26 along with a SER spectrum from C_{60} on Au colloids from Luo et al. [105] and a FT-Raman spectrum of C_{60} at room temperature from Parker et al. [106].

As this TER spectrum is an average over many different tips and surface compositions, it is comparable to the case of SERS on colloids where many "hot spots" are sampled simultaneously. Indeed, our spectrum in a) resembles closely the SER spectrum [105] in b). A comparison of curve a) with the FT-Raman spectrum [106] in c) shows first of all a significant broadening of all TERS peaks and substantial changes in relative intensities of the Raman bands. Some of the lines are also frequency shifted, most notably the strong $A_g(2)$ mode at 1470 cm^{-1} is shifted by more than 10 cm^{-1} to lower energies in the SER and TER spectra. Possible reasons for such a frequency shift will be addressed also in Section 4.4. A third difference in SERS and TERS as compared to a normal Raman spectrum of C_{60} is the appearance

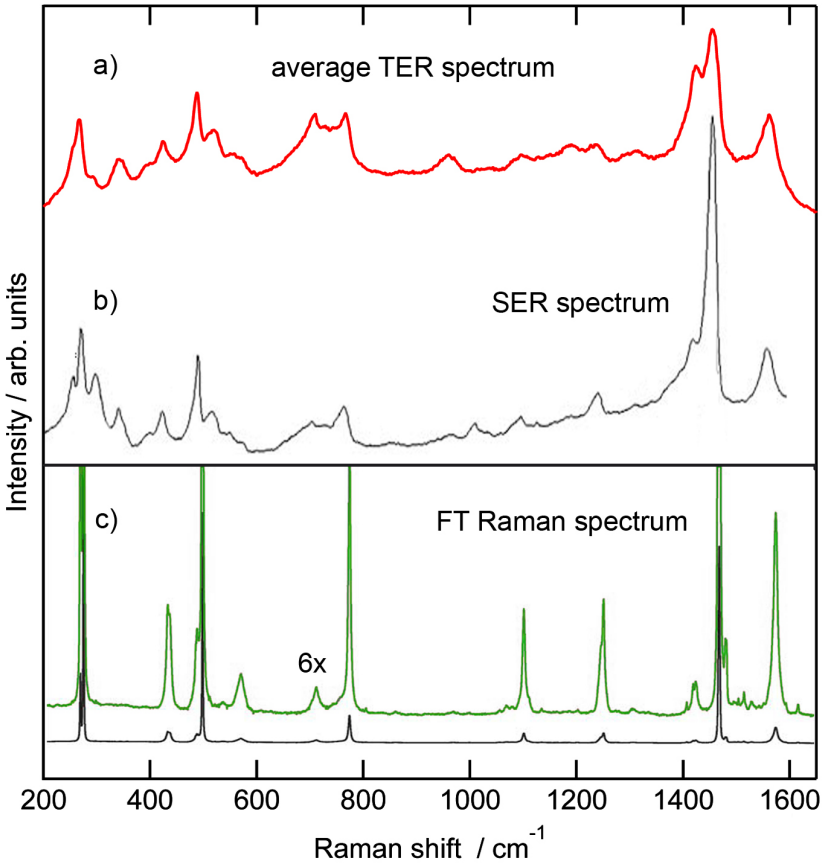

FIGURE 26: Comparison of average TER, SER and FT-Raman spectra of C_{60}. a) Average TER spectrum. b) SERS of C_{60} on gold colloids [105]. c) FT-Raman spectrum of C_{60} at room temperature from ref. [106].

of extra peaks. These can be attributed either to a peak-splitting as result of a lifting of degeneracies or to an activation of "silent" modes. Both are consequences of a symmetry reduction from the high I_h to some lower one. Possible origins for the change in molecular symmetry will be discussed in Section 4.4.

4.2 TIME SERIES OF TER SPECTRA

This section reports the most common observations in time series of TER spectra and describes the way we analyze and interpret them. Figure 27 and Figure 29 show two examples of relatively stable spectral series as intensity plots in a gray scale, where white corresponds to low, and black corresponds to high intensity.

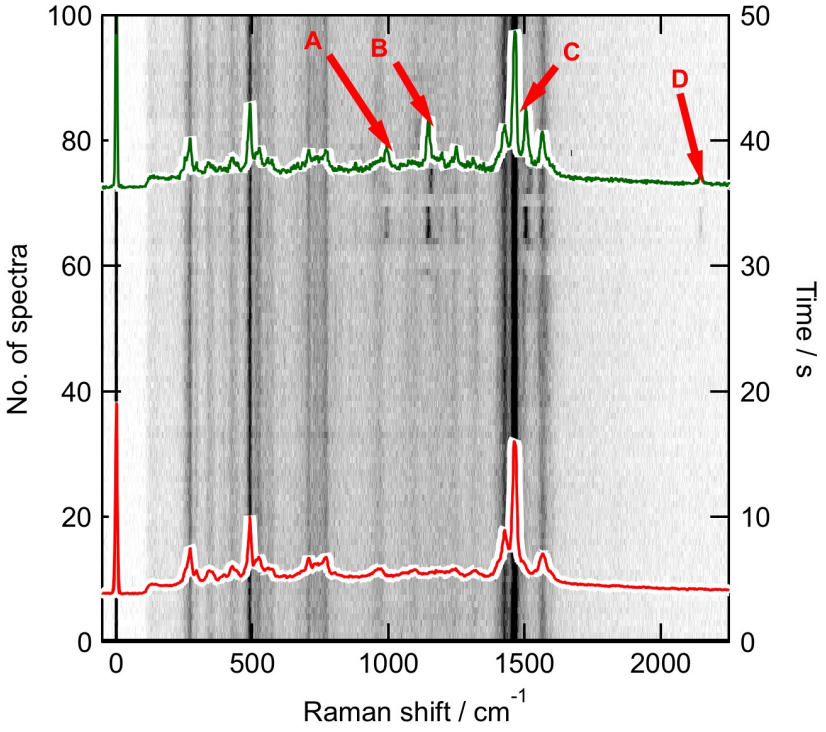

FIGURE 27: Intensity plot of a time series of TER spectra of C_{60} on Au(111) with transient lines not belonging to C_{60}. The integration time is 0.5 s. The left axis gives the number of the spectra and the right one the elapsed time. The horizontal is the spectral axis giving the Raman shift in wavenumbers. Red trace: integrated spectrum from spectrum 0 to 50. Green trace: integrated spectrum from 64 to 69. Both spectra are normalized to the intensity of the laser line for comparison. Red arrows point to peaks that are not identified with C_{60} lines. Tunneling conditions: $U_B = -0.2\,V$, $I_t = 0.1\,nA$. A difference of the green and the red trace is shown in Figure 28.

The x-axis represents the spectral direction while the left y-axis shows the number of the spectra and the right y-axis the elapsed time. In Figure 27 a series of 100 spectra is presented. For the first 65 spectra only the characteristic spectral lines of C_{60} are observed. The relative intensities of the Raman lines and the background are very stable as seen from the homogeneity of the intensity plot along the y axis. An integrated spectrum is plotted as a red trace on top of the intensity plot. Between spectrum 64 and 80 a set of new lines appears

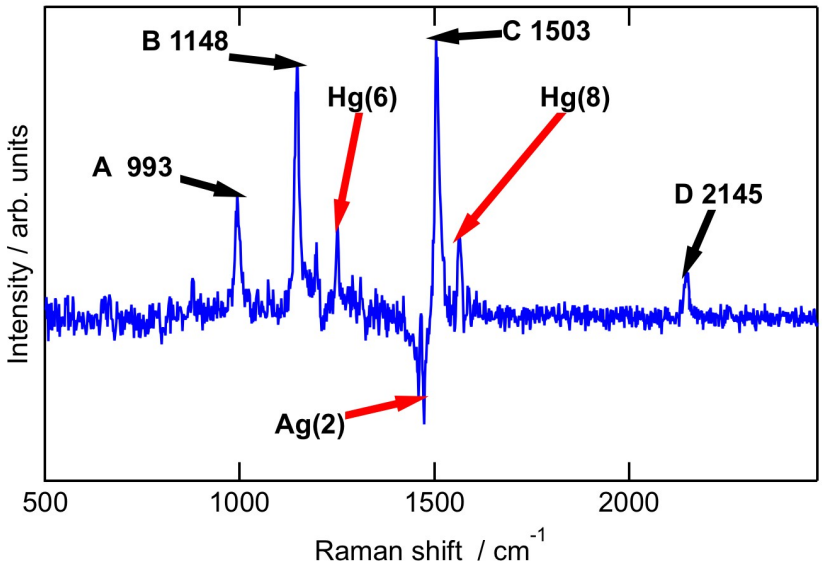

FIGURE 28: Difference spectrum of the green and the red spectrum in Figure 27. The black arrows point to the new lines. Red arrows show lines at or close to the positions of the Raman peaks of C_{60} with the corresponding symmetry assignment.

and disappears again. The green trace in the upper part of the image shows the integrated spectrum between spectrum 64 and 69. Four sharp new peaks at 993 cm^{-1}, 1146 cm^{-1}, 1503 cm^{-1} and 2145 cm^{-1} are observed.

Figure 29 depicts a similar situation as Figure 27. Only in Figure 29 a different set of lines appears for a short period of time. Again the red trace is the summed spectrum over the spectra before the extra lines appear and the green trace the one over the spectra with the additional lines at 1315 cm^{-1}, 1366 cm^{-1} and 1638 cm^{-1}. Also, the $A_g(2)$ mode at 1460 cm^{-1} of the green spectrum is more intense than that of the red one. A zoom of Figure 29 into the spectral region of the additional peaks is shown in Figure 30.

This closer look reveals that at least two of the new lines are not stable over the entire span of their existence. The peaks F and H around 1366 cm^{-1} and 1638 cm^{-1}, respectively, wander about spectrally in a synchronous manner. The red and the green trace on the upper part of the intensity plot are the same as in Figure 29. The blue trace in the lower part presents their difference. While it is very difficult to identify the molecular species that produce these Raman lines, the sharpness and the synchronous behavior of the lines suggest that they stem from a single variety of molecules. The three most probable sources for these molecules are I) contaminations of the near field tip from the etching process; II) contaminations on the sample surface due to

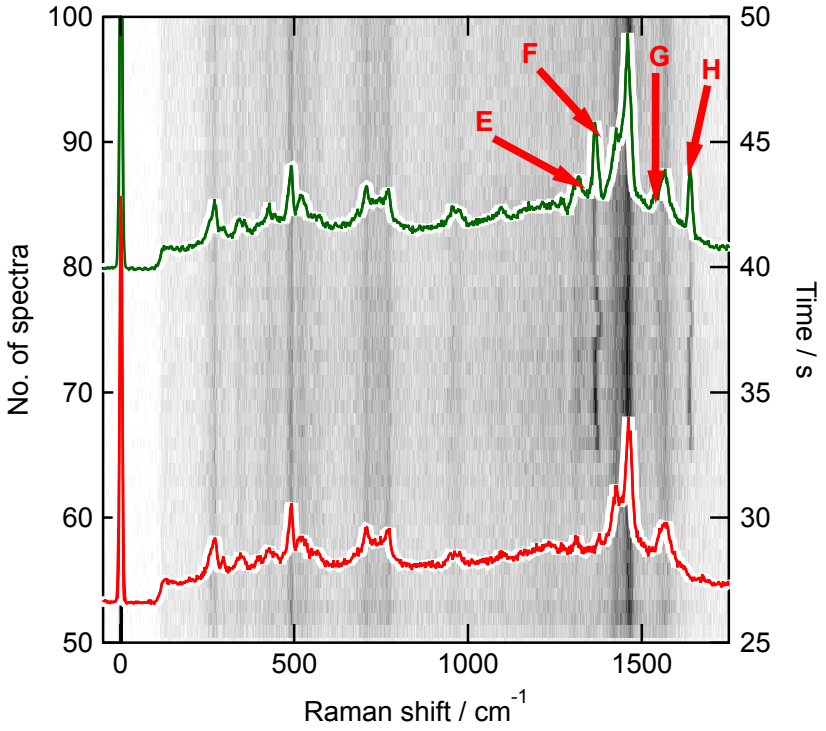

FIGURE 29: Intensity plot of a time series of TER spectra of C_{60} on Au(111) with transient lines not belonging to C_{60}. The green trace is the integrated spectrum over spectra 64 through 87. The red trace over the spectra between 50 and 64. Both spectra are normalized to the intensity of the laser line for comparison. The new lines are labeled E through H.

either insufficient cleaning of the Au(111) sample, an adsorption of foreign molecules during the evaporation or from the rest gas in the vacuum chamber; III) a reaction product from C_{60}.
In both difference spectra described above there are some peaks that are at or very close to the positions of C_{60} Raman peaks. These are indicated by red arrows and the usual labels $H_g(6)$, $A_g(2)$ and $H_g(8)$. This might hint towards an origin of additional peaks from derivatives from C_{60}. At this point however, this can not be proven and the appearance of the C_{60} peaks in the difference spectra can be coincidental.

The sudden appearance and vanishing of the additional lines excludes a situation where the entity producing these lines is fixed to the surface and the tip drifts over it. The tip drifts rather slowly with not more than 1 nm per second and the near-field underneath its apex has an intensity gradient on the 10 nm scale. This would result in a slower intensity dynamics of the lines on the order of 10 s. Instead

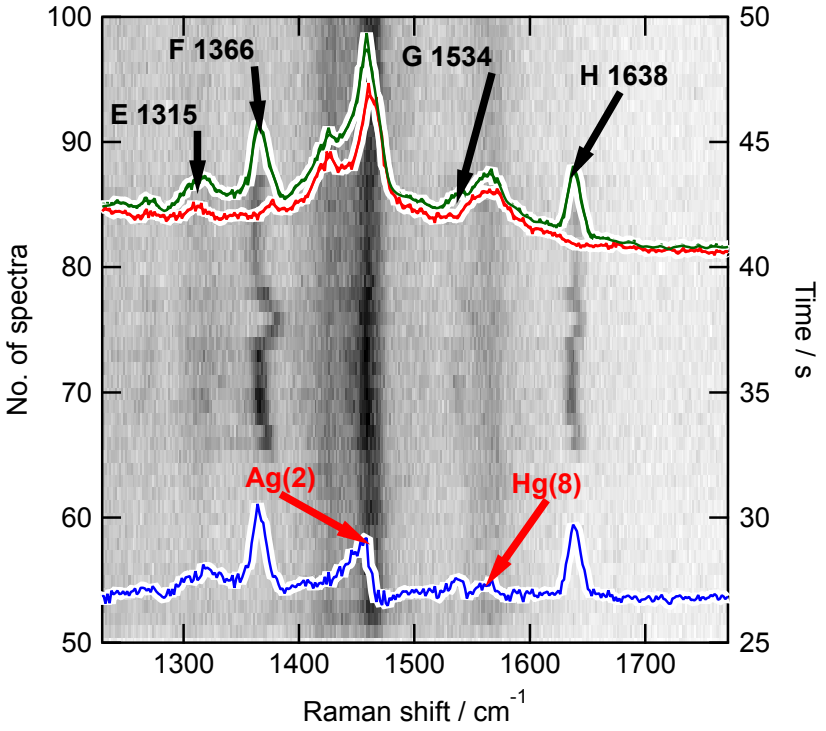

FIGURE 30: Close-up of the region of Figure 29 containing additional peaks.

the foreign Raman lines are probably caused by molecules diffusing in and out of the hot spot, either on the sample surface or on the tip.

The spectral wandering of the lines indicates a change of the corresponding molecules. As the change in spectral position is continuous, as seen from Figure 30, a chemical reaction as a cause is unlikely. More probably these changes reflect a slowly changing interaction of the molecules with their surroundings; for example a drifting of molecules through the electric field gradient around the tip apex.

Finally, the sharpness of the lines and the fact that they wander but do not split or broaden supports the assumption that a rather small number of molecules, if not a single molecule, is behind this effect. A synchronous behavior of a larger amount of identical molecules is less likely.

Additional peaks appear in the vast majority of spectral series that we recorded. For rather stable series they present like in the examples described above: a small number of lines not generic to C_{60} appears for some seconds, fluctuates in intensity and spectral position and then disappears again. But the spectral changes can be also more drastic. Figure 31 and Figure 32 show two such cases.

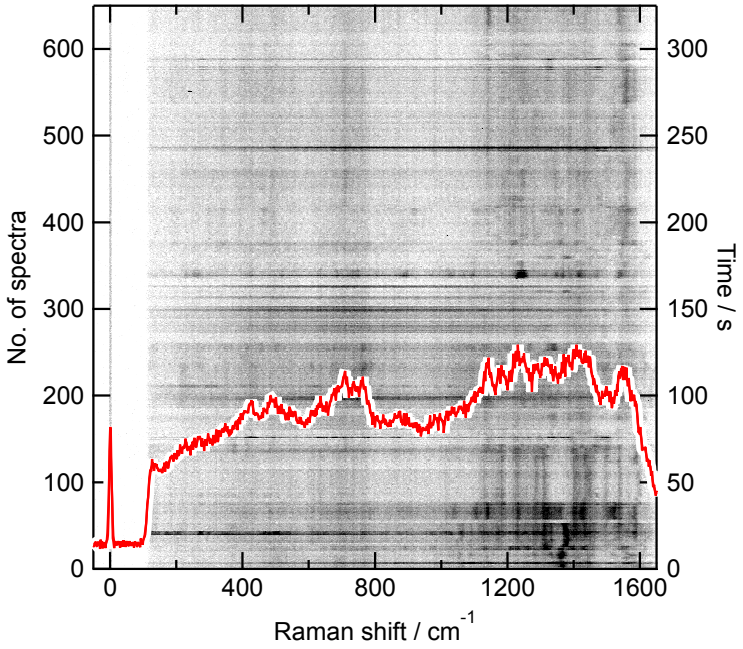

FIGURE 31: Time series of TER spectra exhibiting a lot of spectral changes. The red trace is an average over the entire series.

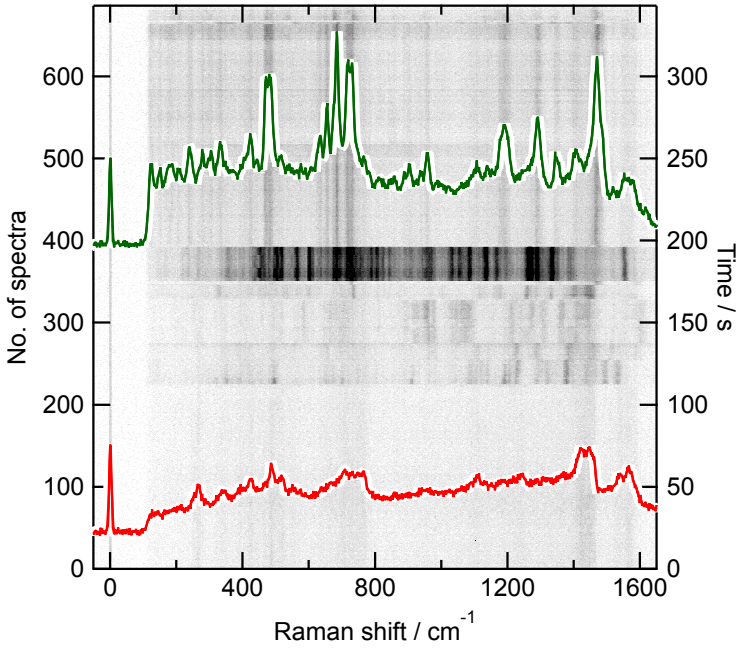

FIGURE 32: Time series with sudden jumps between stable regions of different TER spectra. Red trace: average spectrum of the first 200 spectra. Green trace: average spectrum of the stable region between spectra 394 to 667.

In Figure 31, apart from a large number of Raman lines, that appear and disappear at various positions the intensity plot also presents dark and bright lines along the horizontal direction. They show sudden changes in the broad background of the spectra, that often coincide with the appearance or vanishing of Raman lines. A spectral series like in Figure 31 was not further considered for analysis because of its instability. The red trace on top of the intensity plot is an average over all 700 spectra. The general shape reminds that of a C_{60} spectrum, but the features are very weak, rendering a definite assignment to modes of C_{60} difficult.

Figure 32 shows a case where the spectral features change several times abruptly, without any change of external parameters, while the spectra are stable for many seconds to minutes in between these jumps. The red trace is the integrated spectrum over the first 220 spectra and the green one over the last 270 spectra. The former shows the characteristic peaks of C_{60}, the latter only some of them. The sudden changes between otherwise stable spectra are probably caused by tip configuration changes, such as a pick-up or change of molecules at the tip apex.

Unless stated otherwise, all spectra presented in the following stem from time series of spectra that are stable over several seconds to minutes. Spectra are then integrated over the stable region to gain a better signal to noise ratio.

4.3 DEPENDENCE OF TER SPECTRA ON EXTERNAL PARAMETERS

There are a few, more global parameters that influence TERS of C_{60} at Au(111) such as the incident intensity of the illuminating laser, the tunneling current and the bias voltage of the STM. A fourth parameter is the distance between STM tip and surface, which is, however, controlled by the preset tunneling current and the bias voltage. Only if the feedback of the STM is switched off, an external control of this distance is possible to some extent.

Influence of laser power on TERS and tip heating: First the response of TER spectra to the change of the power of the illuminating laser is investigated. Figure 33 shows a set of TER spectra each for different laser intensities. The red traces show the original data and the black traces correspondingly smoothened curves, added to guide the eye. The lowest spectrum is taken at an initial power I_0 of about 0.5 mW. This spectrum is rather noisy, but the $A_g(2)$ mode can be clearly distinguished. For the next spectrum the laser intensity is increased by a factor of 2.8. Now all major Raman lines of C_{60} are visible. In the middle spectrum the laser is turned on to its full power of 3 mW. For the remaining spectra the laser power is turned down again.

Across the series there is no obvious frequency shift of the Raman lines nor a change in relative intensities, nor a change of the shape of the broad background. The absence of any such effect is important for the comparison of spectra that were recorded at different positions of the sample. The focus of the illuminating laser is about 300 nm in diameter. When moving to a new place of the sample with the STM tip, the focus stays fixed in relation to the sample. Hence, the tip will in general be exposed to a different laser intensity after the change in position.

While the TER spectrum of C_{60} seems to be unaffected by a change in laser power, there is a strong effect of the laser on the tip itself in form of heating. The heating of the tip was investigated using an Au(111) sample without C_{60} molecules and a TERS tip like those employed for the TERS measurements. Figure 34 shows an STM image of the surface in two versions. The right one presents the raw data and the left shows the same data set, but a line mean filter was applied that equalizes the mean value of each scan line (horizontal direction). The graph below shows a line cut along the slow scanning (vertical) direction at the position of the blue arrow in the STM images and averaged over the width of the blue box. After about 13 nm the laser is turned on to its full power by opening an electromechanical shutter. Due to photo-heating the tip extends. The z-piezo retracts in order to maintain the preset tunneling current. This retraction is seen in the

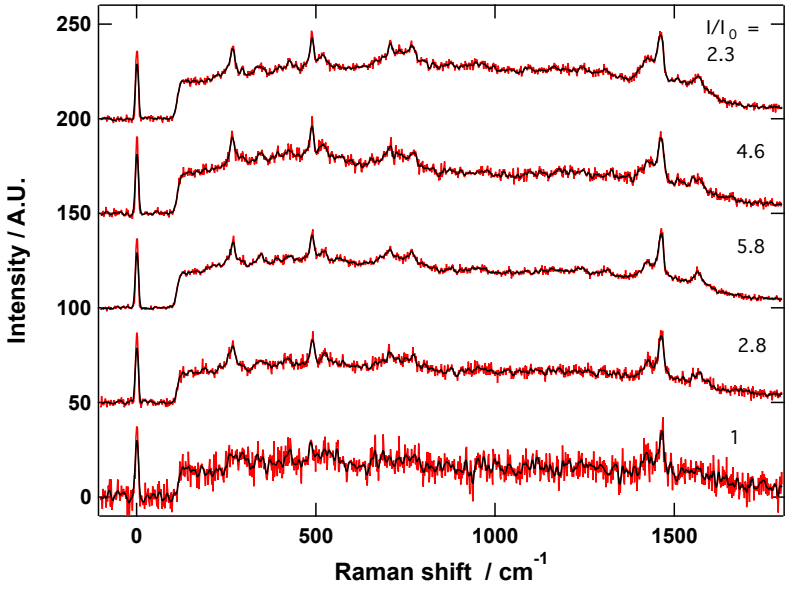

FIGURE 33: Consecutive TER spectra at different laser intensities. Relative laser intensities are specified next to the traces. $I_0 \sim 0.5\,\mathrm{mW}$. Each trace is averaged over a different number of spectra taken with 0.5 s integration time each. The total integration time for the individual spectra are from the lowest to the topmost: 5.5 s, 6 s, 8 s, 4.5 s and 32 s. The spectra are normalized to the laser peak at zero Raman shift.

raw image as a apparent change in surface height. The scan of the entire image took about five minutes. After this time the expansion of the tip has not stopped yet. At the end of the scan the tip has extended by 14 nm (we observe an expansion for all tips under illumination. The amount, however, varies largely between 1 and 14 nm). Judging from the continuous expansion over many minutes and recalling the fact that no influence of the TER spectra on laser intensity was observed (Figure 33 and corresponding discussion above), that would indicate a significant heating, it is concluded that the expansion is not due to a major increase in temperature of the final tip end on a nano- to micrometer scale. Rather, a large portion of the gold tip wire is heated by a few centigrades only. Interesting is the fact, that no lateral offset of the tip is seen in the STM image: the monatomic step in the left image continues in a straight direction after the laser in switched on. This is important to guarantee that the spectra in the intensity-dependent measurements in Figure 33 are indeed taken on the same position on the surface.

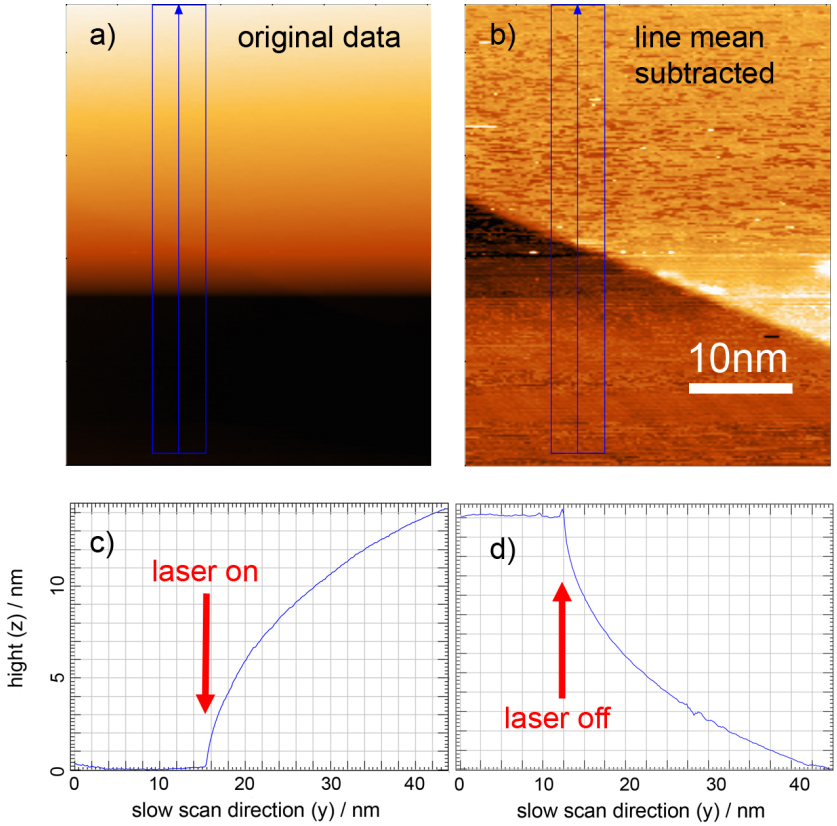

FIGURE 34: Expansion of the near-field tip through heating with the illuminating laser. The two STM images are produced from the same data set recorded with an STM and an Au tip on an Au(111) surface. The left image (a) represents the raw data while in the right image (b) a line mean filter was applied that equalizes the mean value of each scan line (horizontal direction). c) shows a line cut along the slow scanning (vertical) direction at the position of the blue arrow in the STM images and averaged over the width of the blue box. After about 13 nm the laser is turned on to its full power by opening an electromechanical shutter. Due to photo-heating the tip extends. The z-piezo retracts in order to maintain the preset tunneling current. This retraction is seen in the raw image as a apparent change in surface height. The scan of the entire image took about five minutes. After this time the expansion of the tip has not stopped yet. d) Cooling of a tip after the laser was switched off suddenly. Tunneling conditions: $U_B = -2\,V$, $I_t = 0.4\,nA$.

Influence of tunneling parameters on TERS: In this section the response of the TER spectra of C_{60} on changes in the three parameters tunneling current, bias voltage and tip-sample separation is investigated. Figure Figure 35 shows an intensity plot of a time series of TER spec-

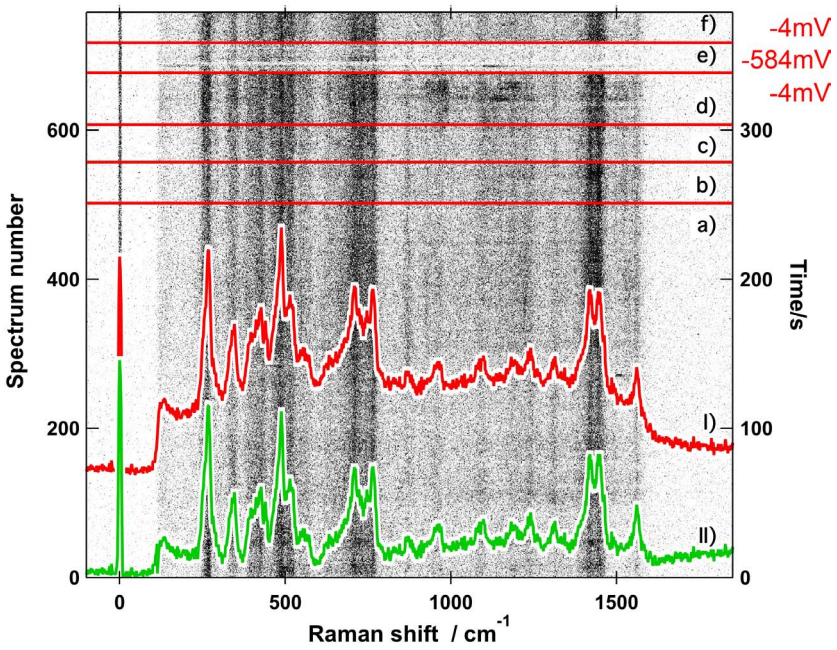

FIGURE 35: Intensity plot of a time series of TER measurements. The left y-axis shows the ordinal number of the spectrum, while the right y-axis shows the elapsed time. The integration time for each spectrum is 0.5 seconds. Horizontal lines in red identify the positions in time where a parameter was changed. The sets of parameters tunneling current (I_t) and bias voltage (U_B) for the areas a) through f) are: a) $I_t = 1\,nA$, $U_B = -0.004\,V$, b) $I_t = 1.7\,nA$, $U_B = -0.004\,V$, c), $I_t = 0.7\,nA$, $U_B = -0.004\,V$, d) $I_t = 0.2\,nA$, $U_B = -0.004\,V$, e), $I_t = 0.2\,nA$, $U_B = -0.584\,V$ and f), $I_t = 0.2\,nA$, $U_B = -0.004\,V$.
In the lower part of the picture two traces are shown. The red one (indicated by I)) is the sum of all the spectra up to the lowest red line. The green trace II) is constructed from I) by subtracting the background.

tra taken while the STM tip was laterally fixed in tunneling contact. The acquisition time for each spectrum is 0.5 seconds. Red horizontal lines indicate the moment of a deliberately taken change in either tunneling current or bias voltage. For the first 500 spectra (250 seconds), i.e. for the entire area below the first red line, the tunneling conditions ($I_t = 1\,nA$, $U_B = -0.004\,V$) are not changed. A sum of all these 500 spectra (red trace) and its background corrected version (green trace) are drawn on top of the intensity plot, where the intensity is given in arbitrary units. The typical lines for C_{60} that were discussed in Section 4.1 are clearly seen. Evidently, the spectra are relatively sta-

ble over a time period of 250 s. How little their main features change can be seen more clearly in Figure 36: Area a) of Figure 35 was partitioned into 10 successive areas of 50 spectra each, which then where summed over to produce the 10 traces that are displayed.

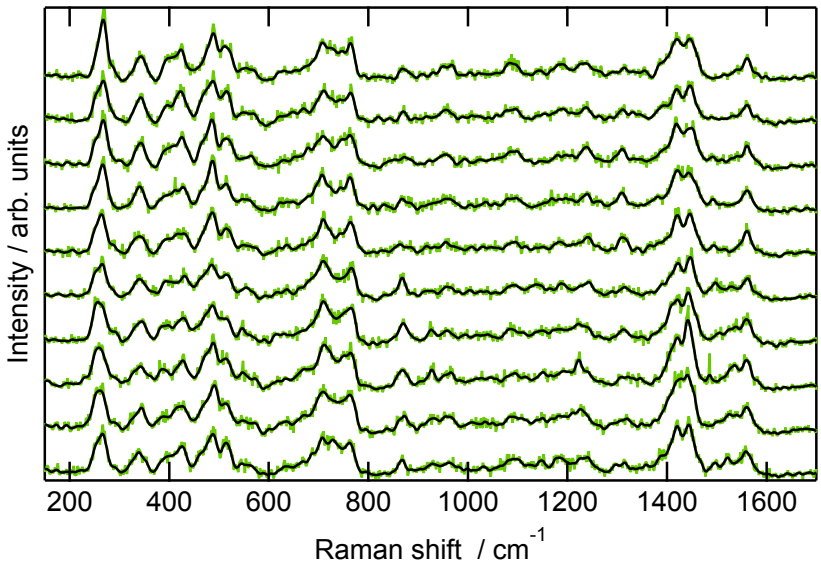

FIGURE 36: Series of average spectra from Figure 35 before current and voltage are changed. Each of the ten TER spectra in this figure results from binning 50 successive spectra from area a) in Figure 35. For improved visibility on each original trace (green) a smoothed version of the same spectrum is drawn in black and the broad background was subtracted.

A high temporal stability of both, spectral position and intensity of the Raman lines is compulsory for experiments where external parameters such as tunneling current, bias voltage or laser intensity are changed.

At the first three red lines in Figure 35 the tunneling current was changed from initially $I_t = 1\,nA$ successively to $I_t = -1.7\,nA$ (area b)), $I_t = 0.7\,nA$ (area c)) and $I_t = 0.2\,nA$ (area d)) while keeping the bias voltage fixed at $U_B = -0.004\,V$.

No obvious change in the Raman spectra can be seen apart from a gain in intensity of a peak around $966\,cm^{-1}$ that could be assigned to the silent mode $G_u(4)$ at $961\,cm^{-1}$ for isolated C_{60} [100]. Alternatively, this peak could also be of foreign origin like the transient peaks discussed in Section 4.2.

The same data are presented again as average spectra in Figure 37. Here, the first spectral trace a) is identical with the last trace of the stable series in Figure 36. Traces b) through f) are sums over the re-

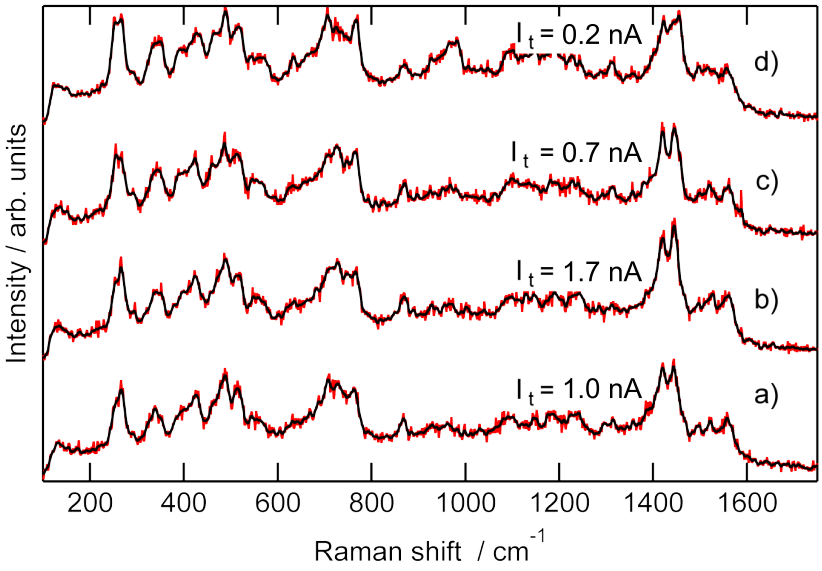

FIGURE 37: Dependence of TER spectra on changes in tunneling current. Average spectra of the data presented in Figure 35. Bias voltage $U_B = -0.004\,V$ for all traces. The tunneling current for the individual traces is: a) $I_t = 1\,nA$, b) $I_t = 1.7\,nA$, c) $I_t = 0.7\,nA$, d) $I_t = 0.2\,nA$.

spective regions in Figure 35. As these regions do not all contain the same number of spectra, the sum spectrum is normalized by dividing through the number of spectra.

At the red line between regions d) and e) in Figure 35 the bias voltage was changed from $U_B = -0.004\,V$ to $U_B = -0.584\,V$ and again back to $U_B = -0.004\,V$ at the last red line between e) and f).[4] The effect on the TER spectra is clearly visible in both Figure 35 and Figure 38, that shows the corresponding average spectra. While there is an over-all loss in intensity from d) to e) the peaks on the high-energy (higher Raman shift) side of the spectrum decrease more drastically than those on the low-energy end. The effect is so drastic that the lowest Raman line at $260\,cm^{-1}$ appears to be hardly altered in Figure 35, while the three highest lines that are clearly visible for very small bias voltage seem to be lost in the noise for $U_B = -0.584\,V$ (region e) in Figure 35. In the average spectrum f) of Figure 38 some of the high-Raman shift peaks can be made out again.

4 Note, that these bias values are corrected for the offset of $-16\,mV$ discussed in the context of Figure 11.

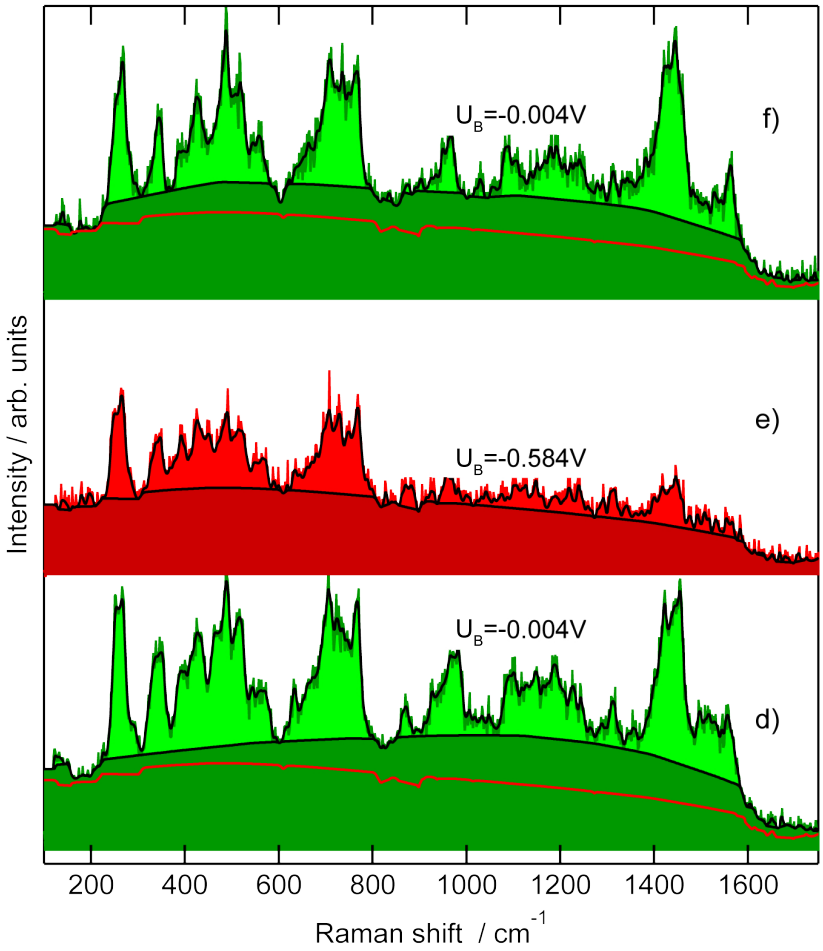

FIGURE 38: Dependence of TER spectra on changes in bias voltage. Average spectra of the data presented in Figure 35. Tunneling current $I_t = 0.2\,nA$. The bias voltage for the individual spectra is: d) $U_B = -0.004\,V$, e) $U_B = -0.584\,V$ and f) $U_B = -0.004\,V$. The background (determined with a routine described in ref. [101]) is drawn as black trace for each spectrum. To compare the shapes of the backgrounds, the background of e) is also drawn as red trace on the spectra d) and f).

Most likely, the TER intensity dependence on the bias voltage is not caused by the voltage (or electric field) change as such, but by the change of the tip-sample distance that is induced by the voltage change in order to keep the tunneling current constant. It is known that TERS signals show a strong distance dependence. In ref. [95] for example, the distance dependence of TER spectra of co-adsorbed guanine and perchlorate is observed on a scale between 1 nm and about 20 nm and found to agree with theory that predicts a $I_{TERS} \propto (R_s + d)^{-10}$ distance dependence of the TERS intensity I_{TERS} on the tip-sample separation d, where R_s is the radius of the tip apex.

In the current experiment, however, the distance changes on a sub-nanometer scale (about 0.3 nm). The plasmon mode spectrum of the system composed of gold tip and Au(111) surface changes when their distance is altered. The smaller the distance the more intense the plasmons become, leading to an increased enhancement of Raman spectra. At the same time the plasmon modes shift to the red with decreasing distance, in agreement with the findings of [95]. This leads to a more pronounced enhancement of the modes having higher Raman shifts.

Also the change in tunneling current results in a modification of the tip-sample separation. That no changes are observed for different currents can be explained by the fact, that the maximal change in current was only a factor of 8.5, while the bias voltage was changed by a factor of almost 150.

To investigate this close-range distance dependence further the following experiment was performed. A gold near-field tip was approached to an Au(111) surface with a low coverage of C_{60} like shown in the STM image in Figure 22 a). The experiment will be explained in detail in the following and the results are depicted in Figure 39. Panel a) shows an intensity plot of the series of TER spectra over a period of about 300 s. The spectral pattern of C_{60} is clearly visible. The observable intensity changes are consequences of changes in the tip-sample separation. In panel b) two cuts along the time axis are presented. These cuts show the time variation of the $A_g(2)$ peak at 1450 cm^{-1} and of the $H_g(8)$ peak at 1560 cm^{-1}. These time variations are induced by distance variations imposed manually on tip sample gap. Details of the experiment will be given below. In order to lower the noise level of both traces in b) the data matrix represented in a) was first decomposed by a *singular value decomposition* (SVD) [107, 108] and then reconstructed using only the five strongest components that carry most of the spectral information of the matrix plotted in a). In this way the noise contained in the spectra is eliminated to a large extent (actually, the noise contributions are shifted by the SVD rou-

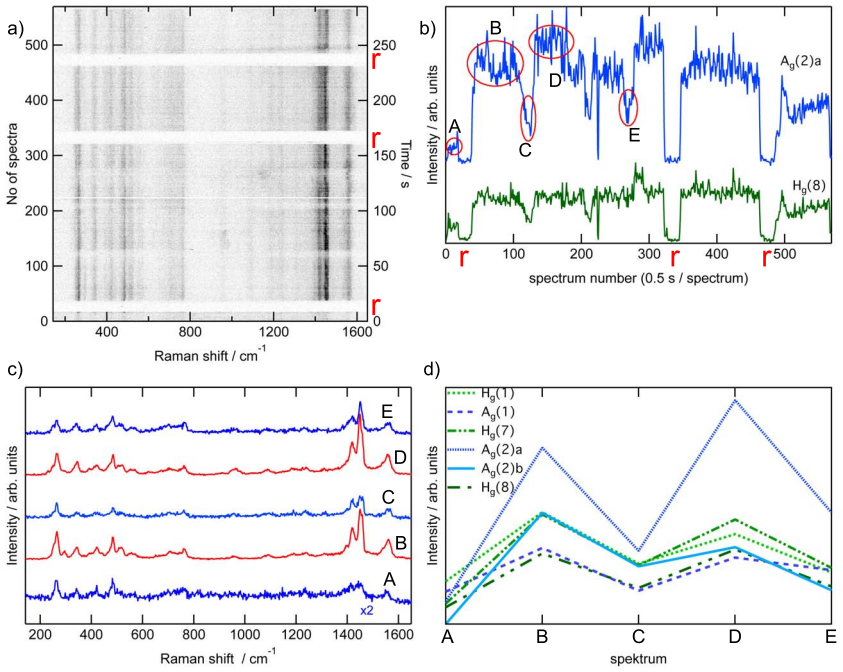

FIGURE 39: Response of TERS to changes of the tip-sample separation. a) Intensity plot of a time series of TER spectra of C_{60} on Au(111). b) Cuts along the time axes through the time series at spectral positions 1450 cm^{-1} (blue trace) and 1556 cm^{-1} (green trace). c) Average spectra over regions of comparable intensity indicated by capital letters in panel b). d) Development of the intensities of six TERS peaks indicated in the legend. Further explanations are found in the main text. Bias voltage $U_B = -0.04$ V.

tine to higher components of the decomposition that are not used for reconstruction). The reconstructed data set is only used to produce the two traces in panel b). All other panels contain the original data. The $A_g(2)$ band obviously is split into two as seen more clearly in the enlarged spectrum D of Figure 39c) in Figure 40. We will call the intense peak at about 1450 cm^{-1} "$A_g(2)$a" and the shoulder at about 1460 cm^{-1} "$A_g(2)$b". The splitting of the $A_g(2)$ line might be a result of the presence of two different adsorption sites of C_{60} on Au(111). This point will be addressed in Section 4.4. The blue trace in Figure 39b) is at the spectral position of the $A_g(2)$a band, the green trace at the position of the $H_g(8)$ mode. Average spectra over the time intervals indicated by red ellipses and capital letters in b) are plotted in panel c). Panel d) then shows the peak heights of selected Raman bands for the five spectra in c). At positions labeled with a red "r", the tip was retracted until no tunneling current could be measured.

The actual course of the experiment was performed as described in this paragraph: Once the tip had been moved into the tunneling

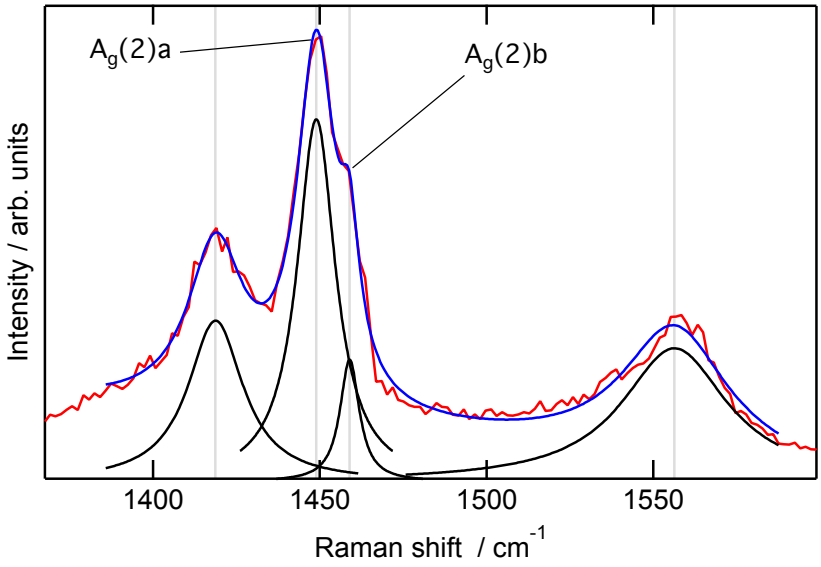

FIGURE 40: The spectral region of the $A_g(2)$ mode of spectrum D from Figure 39c) is shown in detail. The $A_g(2)$ mode is split into a peak at 1450 cm^{-1} and a shoulder at 1460 cm^{-1}. Fitted with four Lorentzian functions.

regime, the bias voltage was set to $U_B = -4\,mV$ and the tunneling current to $I_t = 0.1\,nA$. A stable sequence of TER spectra was recorded for about 10 s and is shown in region A of Figure 39. Next, the feedback loop of the STM was switched off and the tip was retracted until no tunneling current could be measured. As a consequence the TER signal disappeared completely, see the first region labeled "r".

At ~ 30 s, the tip was again approached closer to the surface until the tunneling current came close to the threshold of the preamplifier of the STM of 13.5 nA. The TERS signal increased drastically, see region B. As the feedback loop of the STM was off, drift in the z-direction was not compensated. Hence, the tunneling current changed upon changing the tip-surface distance. The tunneling current fluctuated and decreased (not recorded), accompanied by a simultaneous decrease in TER intensity. This decline in intensity is seen in the slope in Figure 39 b) between regions B and C. When the current dropped to only some nA, the tip was approached again until a high current value was established, which was accompanied by an increase of the TER signal (see region D). During the entire time, TER spectra where recorded subsequently, and each of them with 0.5 s integration time. Between D and E the system was again left to itself, showing - aside noise - a constant intensity level that deceased at some instances more or less stepwise. After the region E the tip was approached again closer to the surface until after point E a tunneling current around

10 nA was flowing. For the rest of the time series the tip was retracted twice until no tunneling current was detected (regions "r") and approached again into tunneling.

The effect of the tip-sample separation on the signal strength is again illustrated by the average spectra in Figure 39 c). The lowest trace belonging to region A is multiplied by two for convenient comparison with the other spectra.

All peaks gain intensity from A to B, then decrease again in C, before they become intense once more in D and weak in E. For six Raman bands ($H_g(1)$, $H_g(7)$, $H_g(8)$, $A_g(1)$, $A_g(2)$a and $A_g(2)$b) this sequence of up and down of the TERS intensities is presented in Figure 39 d). The depicted values are the peak heights of the respective Raman modes evaluated by fitting the spectra with Lorentz peaks like exemplified in Figure 40 for the four highest modes of spectrum D.

This experiment illustrates nicely that there is a strong dependence of the TERS intensities on the tip-sample separation in gap-mode TERS in the tunneling distance regime below 1 nm. This close-range distance dependence has consequences for TERS as an analytical technique. First of all it allows to measure TERS signals of molecules with smaller Raman cross-sections because the signal enhancement can be increased simply by changing the tunneling conditions. Secondly it shows that care has to be taken in the interpretation of TERS maps. Usually synchronous to the TERS maps a topographic image is recorded. When operating in gap-mode, the Raman analyte is adsorbed on a plasmonic surface. While recording a topographic image, the tip-sample separation is modulated, which can lead to a modulation of the TERS signal strength that can not be correlated with the amount of Raman scatterers inside the TERS radius. Hence, care has to be taken when TERS maps are employed to measure the lateral resolution of the particular TERS experiment.

4.4 TERS OF C_{60} ON Au(111) FOR DIFFERENT SURFACE COMPOSITIONS

In this section TER spectra from samples with three different surface composition of C_{60} on Au(111) are discussed:

Type I: Samples with a low coverage of C_{60}, where the molecules mainly adsorb at step edges of Au(111).
Type II: Samples with higher coverages of C_{60}: in this case the molecules form larger two-dimensional islands of monomolecular thickness that expand from step edges onto terraces.
Type III: Sample of type II that was five days old and showed clear changes of the two-dimensional island composition: the originally homogeneous, hexagonal structure is transformed to a more amorphous pattern. TERS experiments had been performed on the sample on several days before. However, the changes in the C_{60} layer are not due to photo-degradation, because they are observed at several positions of the sample. To change the position on the sample, it was retracted by several millimeters and then again fixed in the STM. The probability to arrive at the same sample area of 1 µm twice is, hence, near zero.

An example of an STM image of a type I sample was presented above on page 52 in Figure 22 a). Monoatomic steps of Au(111) are decorated with thin lines of molecules, mostly one and sometimes two molecules in width. Occasionally, smaller islands grow from the step onto a terrace.

Panel a) of Figure 41 presents a close up of the same sample position as Figure 22 a) . The hexagonal arrangement of the small island is clearly seen. In panel c) an STM image of a surface with roughly 50% of a monolayer of C_{60} is shown, obviously a type II sample. The largest fraction of the molecules is organized in large islands. Only 5% to 10% of the molecules are in contact with a step edge of the substrate.

The STM image in panel b) shows an intermediate step between a) and c). While some of the steps are still only decorated by a single row of molecules, at other steps elongated islands grow from the step onto a terrace. For this case no TER spectra where recorded and, thus, will not be discussed in the following. However, the image in panel b) shows nicely that those C_{60} molecules that are attached to a step edge in a single row appear a bit larger in the STM image. Equally, for islands: the row of molecules that is in contact with the Au(111) step edge show up a little bit elevated. Finally, panel d) shows a surface five days after the preparation, a prototype of a type III sample. The homogenous film in c) has clearly evolved into a granular structure.

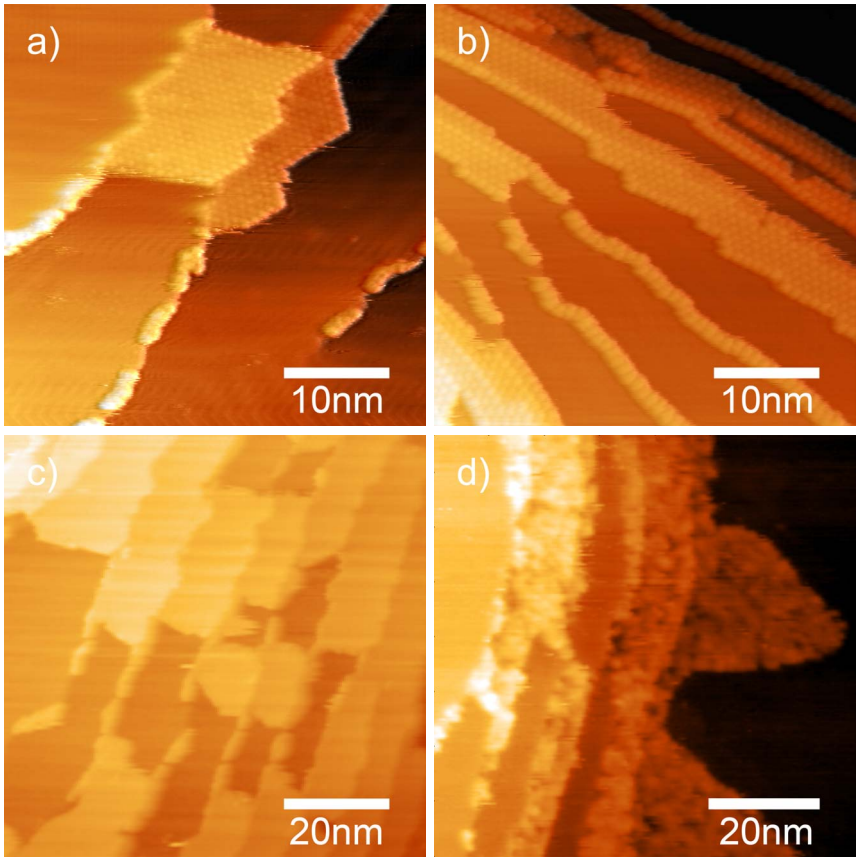

FIGURE 41: STM images of different surface compositions of C_{60} on Au(111). a) Sample with low coverage and mainly step decoration with C_{60}. b) Intermediate surface density of C_{60} molecules. c) about 50 % coverage with C_{60}, fresh sample. d) sample with ~ 50 % coverage of C_{60} after five days in UHV. Tunneling conditions: a) and b) $U_B = -2\,V$, $I_t = 0.07\,nA$, c) and d) $U_B = -2\,V$, $I_t = 0.1\,nA$

The following observation is noteworthy. Neither type I nor type II exist in pure form. That means on a sample with step decoration there are always a few small islands and for a sample with larger islands there is still a certain amount of molecules that is in direct contact with the step edges. However, in an average of many spectra taken on surfaces of type I the step decoration dominates, while for II the main part of the spectrum stems from molecules on terraces organised in close-packed islands.

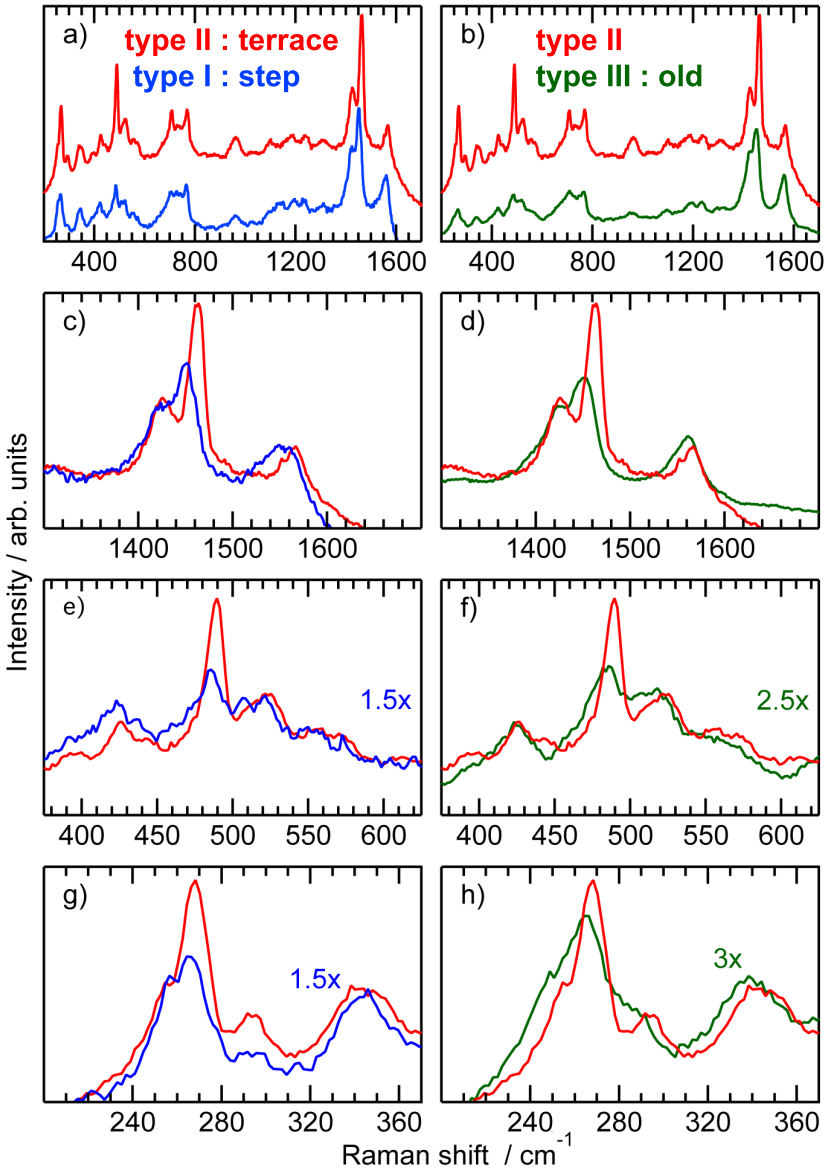

FIGURE 42: Averaged TER spectra of three different types of samples. Type I: Low C_{60} coverage, mainly step decoration. Type II: High coverage (~ 0.5 monolayer). Type III: Sample with high coverage and signs of decomposition in STM images; sample was five days old and stored under UHV conditions. The trace colors blue, red and green refer to type I, type II and type III samples. Panel a) and b) present overviews over the entire spectral range from 200 cm^{-1} to 1700 cm^{-1}. For convenient comparison, in both panels a) and b), the two spectra are separated by a vertical offset. Panels c) through h) show details of specific spectral regions. Curves with the same color belong to the same data set. The spectra in panels c) through h) are normalized to the $H_g(7)$ peak. For better comparison some spectra are additionally multiplied by the indicated factors.

Figure 42 presents the TER data to the three different surface configurations. The spectra in the upper row show the entire spectral region of interest of the C_{60} Raman spectrum from 200 cm^{-1} to 1700 cm^{-1}, while the remaining six panels show zooms into specific subregions. The red trace in all panels corresponds to an average of 22 spectra (each of them is already averaged over a stable region) of type II samples, recorded at two different days. The green trace is an average of 23 spectra of type III samples all taken at the same day and the blue trace is an average of 14 spectra from type I samples taken at one day.

First, the difference between spectra of high (red trace, type II samples) and low (blue trace, type I sample) C_{60} coverage of the Au(111) surface is discussed. Panel a) in Figure 42 shows that the two spectra resemble each other closely. The most prominent distinction is a difference in relative intensity for several Raman bands, most notably of the ratio between the two A_g modes and other vibrational modes. A second distinction consists of a shift of the $A_g(2)$ mode by 10 cm^{-1} in the red spectrum with respect to the blue one. Panel c) presents the expanded spectral region between 1300 cm^{-1} and 1600 cm^{-1}. In addition, to facilitate the comparison of relative intensities, the spectra are normalized to the height of the $H_g(7)$ peak at 1420 cm^{-1}. While the $A_g(2)$ mode for type II samples (high C60 coverage, red trace) is located at 1460 cm^{-1}, for the surface with mainly step decoration the same mode is far less intense and appears at 1450 cm^{-1} with only a weak shoulder at 1460 cm^{-1}. Like in Section 4.3, these two modes are denoted $A_g(2)$a and $A_g(2)$b, respectively. The line at 1460 cm^{-1} is interpreted as the $A_g(2)$ mode of molecules forming islands on a terrace of Au(111). The 1450 cm^{-1} line ($A_g(2)$a) in the blue spectrum is assigned as the $A_g(2)$ mode stemming from type I samples, i.e. from molecules adsorbed at a step edge. The appearance of the shoulder at 1460 cm^{-1} ($A_g(2)$b) is then due to a certain amount of molecules that are not located at the step edges, but organized in islands. That no sign of a shoulder at 1450 cm^{-1} is observed in the red spectrum can be explained by the fact that the fraction of molecules adsorbed at step edges for samples with high coverage of C_{60} is much lower than the fraction of molecules that build islands in low coverage samples. This is obvious from the STM image in Figure 22 a), where the number of molecules in the islands is roughly the same as the number of molecules in contact with a step edge. On the other hand, for panel c) of Figure 41, only 5% to 10% of the molecules are in contact with a step edge of the substrate.

The $H_g(8)$ mode around 1560 cm^{-1} is slightly shifted to lower energies in the blue spectrum. Because of the broadening of the same line the exact shift is not determined (The broadening could be due to the appearance of a new Raman active band, that we observe occa-

sionally at different positions between the $A_g(2)$ and the $H_g(8)$ mode. The origin of this band is not clear at the moment).

Panel e) of Figure 42 shows the spectral region around the $A_g(1)$ mode. Here the blue trace (type I samples) was amplified by a factor of 1.5 with respect to the red one to facilitate the comparison, as it is also done in panel g). Both the $H_g(2)$ and the $A_g(1)$ mode are shifted to lower values for the step decorated (type I, blue trace) surface by almost $5\,cm^{-1}$. The $A_g(1)$ mode has also lost in intensity relative to neighboring modes.

In panel g) the lowest part of the TER spectra is presented. The $H_g(1)$ mode is split into three lines due to a reduction of the molecular symmetry, [109]. The intensity of the main $H_g(1)$ line is reduced in the blue spectrum as compared to the red one, while all three $H_g(1)$ derived lines stay at the same spectral position. The broad peak at around $340\,cm^{-1}$ is not present in Raman spectra of C_{60} crystals, but it is reported in SERS studies on Au substrates. Two silent modes of isolated C_{60} are known around the position of this peak. An activation of one or both of them due to a reduction of symmetry could explain the appearance of the TERS feature. In the step edge spectrum (blue) this line is less broad than for the corresponding terrace spectrum (red).

Next, the right column of Figure 42 which presents the same spectral sections as the left column is discussed. The green spectrum stems from a sample with clear signs of a change in composition of the C_{60} adlayer in the STM images, like illustrated in Figure 41d). We interpret this modification as a polymerization of the C_{60} molecules. The red spectrum is the same as in the right column. In Figure 42d) the high energy region around the $A_g(2)$ mode is shown. Here again, the intensities are normalized to the height of the $1420\,cm^{-1}$ peaks for comparison. The $A_g(2)$ line of the polymerized sample is considerably reduced in intensity and downshifted by $10\,cm^{-1}$ to $1450\,cm^{-1}$. Notice that compared to the corresponding blue spectrum in pane c), the $A_g(2)$ line of the green spectrum does not show a shoulder at $1460\,cm^{-1}$, but is a single smooth and broad band. The $H_g(8)$ line is also downshifted but only by about $5\,cm^{-1}$. The $T_{1u}(1)$ and the $A_g(1)$ mode, shown in panel f), experiences about the same amount of frequency shift. The $A_g(1)$ mode is also reduced in intensity. In panel h) again the lower part of the spectra is shown. All peaks of the polymerized spectrum here are shifted by about $2\,cm^{-1}$ with respect to the spectrum of the fresh sample. The triplet of $H_g(1)$ derived lines also is broadened; what is seen as a small peak in the red spectrum is now a broad shoulder.

The TER spectra of step decoration (blue, type I samples) and polymerized C_{60} (green, type III sample) resemble one another in many respects. The main difference is that the type I spectrum exhibits sharper features. In panel h), showing the low Raman shift region of the TERS spectra, one can see that the type III spectrum is shifted to smaller Raman shifts compared to the type II spectrum, while the features of the blue spectrum coincide with those of the red one in energy.

It is possible that what we interpret as spectra of C_{60} at Au steps is in fact also a spectrum from polymerized C_{60}. Different adsorption geometries for C_{60} at step edges in comparison to those at terraces could favor the polymerization. A similar effect is known for bulk C_{60} samples. There, the photo-polymerization is observed only in a temperature window between about 260 K and 370 K [110]. The hindering of the polymerization at low temperatures is explained by a phase transition between a room temperature fcc lattice structure with one molecule per unit cell and a low temperature sc structure with four molecules per unit cell. In order for the polymerization to take place, double bonds of neighboring molecules have to be parallel and less than 4.2 Å apart [111]. For the low temperature phase of crystalline C_{60} this criterium is not met. For temperatures above 100 °C the covalent bonds of the polymer break again and the pristine monomer form of the sample is restored [112].
Altman and Colton conclude from STM measurements that the rotational orientation of C_{60} molecules adsorbed in monolayer islands on Au(111) changes on a time scale of minutes [67]. The interaction of the molecules with the surface leads to a relative orientation of neighboring molecules that could hinder a possible photo-polymerization. The slow change of the orientation of adsorbed molecules can explain the polymerization on the time scale of days. Only when the relative orientation of two adjacent molecules is right, they can form covalent bonds to form polymers. As the reorientation of C_{60} happens on the time scale of minutes, the probability for finding a correct orientation and distance between two adjacent C_{60} molecules is rather low and, thus, there is a rather low polymerisation rate. On step edges, however, different relative orientations of molecules can favor or hinder the polymerization.

Frequencies of isolated C_{60} molecules [100]		From this work			Pressure-polymerized C60 [109]			
I_h symmetry		I	II	III	DS	O	T	R
		255	**253**	**247**	*256*		*258*	*243*
		267	**268**	**266**	*269*	*256*	*279*	*273*
		278						
272	$H_g(1)$	**294**	**294**	**287**	*295*	*274*	*282*	*306*
342	$T_{3u}(1)$	**344**	**344**	**339**	*338*	*346*		*344*
353	$G_u(1)$				*365*		*363*	
		390	393		*392*			
403	$H_u(1)$			402	*402*			
		424	**426**	**425**	*428*			*415*
					441			
433	$H_g(2)$	**438**	**445**	**459**	*450*	*452*	*453*	*453*
485	$G_g(1)$		479		*478*	*471*		*470*
496	$A_g(1)$	**486**	**489**	**483**	*490*	*488*	*487*	*487*
		508	511	506				
526	$T_{1u}(1)$	**522**	**524**	**520**	*528*	*530*	*532*	*523*
534	$H_u(2)$				*546*	*543*	*538*	*533*
553	$T_{3g}(1)$	**556**	**556**	**558**				
567	$G_g(2)$							
568	$T_{1g}(1)$				*561*	*562*	*588*	*595*
575	$T_{1u}(2)$		573		*576*	*577*	*565*	*555*
					613	*614*	*605*	*608*
668	$H_u(1)$				*668*	*668*	*654*	*663*
709	$H_g(3)$	**704**	**707**	**709**	*708*	*714*	*713*	*719*
					711	*716*	*716*	*718*
736	$G_g(3)$	726		729	*733*	*738*	*747*	*743*
743	$H_u(4)$	743		748				
					755	*753*	*743*	
772	$H_g(4)$	**766**	**769**	**766**	*770*	*748*	*768*	*749*
796	$T_{3g}(3)$				*778*	*780*	*778*	
831	$T_{1g}(2)$		839	820				
			877	864	*920*	*924*	*932*	*998*
961	$G_u(4)$	**963**	**962**	**954**	*943*	*945*	*955*	*956*
984	A_u							
		1024	1023					
1079	$G_g(4)$							
1099	$H_g(5)$	**1091**	**1099**	**1093**	*1102*	*1109*	*1109*	*1077*
		1137		1137				

Frequencies of isolated C_{60} molecules [100]		From this work			Pressure-polymerized C60 [109]			
I_h symmetry		I	II	III	DS	O	T	R
1182	$T_{1u}(3)$	**1193**	**1180**	**1189**	*1189*	*1195*		*1206*
1205	$T_{3u}(4)$							
1223	$H_u(5)$	1234		1235	*1233*	*1243*		*1222*
			1240		*1246*	*1260*	*1263*	
1252	$H_g(6)$				*1250*	*1260*	*1259*	*1229*
1289	$T_{1g}(3)$							
1309	$G_u(5)$				*1283*			
						1297	*1296*	*1292*
1310	$G_g(5)$		1310	1304		*1310*	*1308*	*1315*
						1319	*1342*	
					1321	*1326*	*1346*	*1306*
1344	$H_u(6)$							
1345	$T_{3g}(4)$				*1348*	*1350*	*1328*	*1354*
				1396	*1403*	*1396*		
1425	$H_g(7)$	**1423**	**1425**	**1423**	*1424*	*1432*		*1381*
1429	$T_{1u}(4)$				*1426*	*1426*		
		1450						
1470	$A_g(2)$	1459	**1462**	**1451**	*1462*	*1457*	*1449*	*1406*
1482	$G_g(6)$							
							1465	*1493*
1525	$T_{3u}(5)$	1523			*1518*			
							1544	*1538*
1569	$H_u(7)$				*1556*	*1560*		*1550*
1575	$H_g(8)$	**1560**	**1564**	**1560**	*1570*	*1572*	*1573*	*1567*

TABLE 1: Table of Raman lines of C_{60}. The first two columns give the Raman shifts for isolated C_{60} molecules in cm^{-1} and the assignment according to the irreducible representations of the molecular symmetry group I_h. The next three columns contain the values extracted from the spectra presented in Figure 42 for the three surface types. Boldface numbers indicate peaks and shoulders that are clearly visible, while weaker features are in normal font. Reference values of C_{60} dimers (DS), linear (O), tetragonal (T) and trigonal (R) polymers are presented in the last four columns. These values for dimers and polymers are reproduced from [109].

Table1 presents the fitted peak positions of the three average spectra that are shown in Figure 42 in the columns labeled I through III for the corresponding sample compositions (type I, type II and type III samples) discussed above. In the first column reference values for the undisturbed C_{60} molecule and the labels according to representation theory are given. The last four columns contain Raman modes for C_{60} dimers (DS) and the three different C_{60} polymers: linear (O), tetragonal (T) and trigonal (R), according to ref. [109]. The features found in spectrum II fit best to values of the C_{60} dimer. This can be caused by a possible photo-dimerization of the C_{60} layer. Another explanation could be that the interaction of the C_{60} molecules with the Au(111) surface has a similar symmetry breaking effect as the formation of C_{60} dimers; i.e. the same selection rules would apply for both cases. The $A_g(2)$ modes around $1450\,cm^{-1}$ in spectra of type I and III fit best to the presence of T polymers. The existence of this type of polymers can also explain the granular structure of the C_{60} layer observed in STM images, i.e. Figure 41. In order to form tetragonal polymers the C_{60} molecules have to give up the hexagonal arrangement of the pristine C_{60} monolayer. On the other hand is it not clear why the tetragonal polymer should be favored over a trigonal polymer when starting from a hexagonal film.

4.5 CORRELATION OF STM IMAGES AND TER SPECTRA

An important goal for TERS experiments is to record STM images and maps of TER spectra from the same area of the sample. This would allow the correlation between chemical information, given in the form of vibrational spectra, and structural information from topographic images on a nanometer scale.

The correlation of topographic and TERS images was already accomplished for samples with higher Raman cross-sections under ambient conditions. An example is the imaging of the G' band of a single wall carbon nano tube bundle by Hartschuh *et al.* [92].

During the final drafting of this theses Zhang *et al.* have published a UHV-TERS study where they present TERS maps with sub-molecular resolution [51]. To achieve the necessary sensitivity for such an experiment they use a special double-resonance mechanism.

An important prerequisite for correlating TERS maps with STM images is the ability to either record STM images before and after the TERS measurements or to record TER spectra during the acquisition of STM images. A requirement for the simultaneous STM and TERS experiments is the capability of recording STM images while the tip is illuminated. In the following three experiments are presented that demonstrate all the aforementioned prerequisites.

First, the experiment summarized in Figure 42 and already published in ref. [41] is discussed. Figure 43a) shows an STM image of two islands of C_{60} molecules adsorbed at a step edge of an Au(111) surface. One island is on the upper terrace, the other on the lower terrace. The individual molecules are clearly visible and are arranged in the well known hexagonal structure. After the STM was taken the tip was positioned in the center of the image and TER spectra were recorded for about 40 s. These spectra are presented in panel c). Each trace is an average of 16 successive spectra of 0.5 s integration time and has a temporal overlap with its neighbors of 3 s. The red trace at the bottom of the image is the earliest and the blue trace on top is the last average spectrum. The typical TERS features of C_{60} are visible. Immediately after the TERS measurements another STM image was recorded; it is displayed in panel b). The same double island is still present. Because of a small drift of the tip the islands appear off-set by some nm towards the lower left of the image. Some of the molecules seem to have disappeared, but the image quality does not permit to count the exact number. Especially in the right island less of the individual molecules are discernible and some undefined structures appear. These differences in the two images could point to some mod-

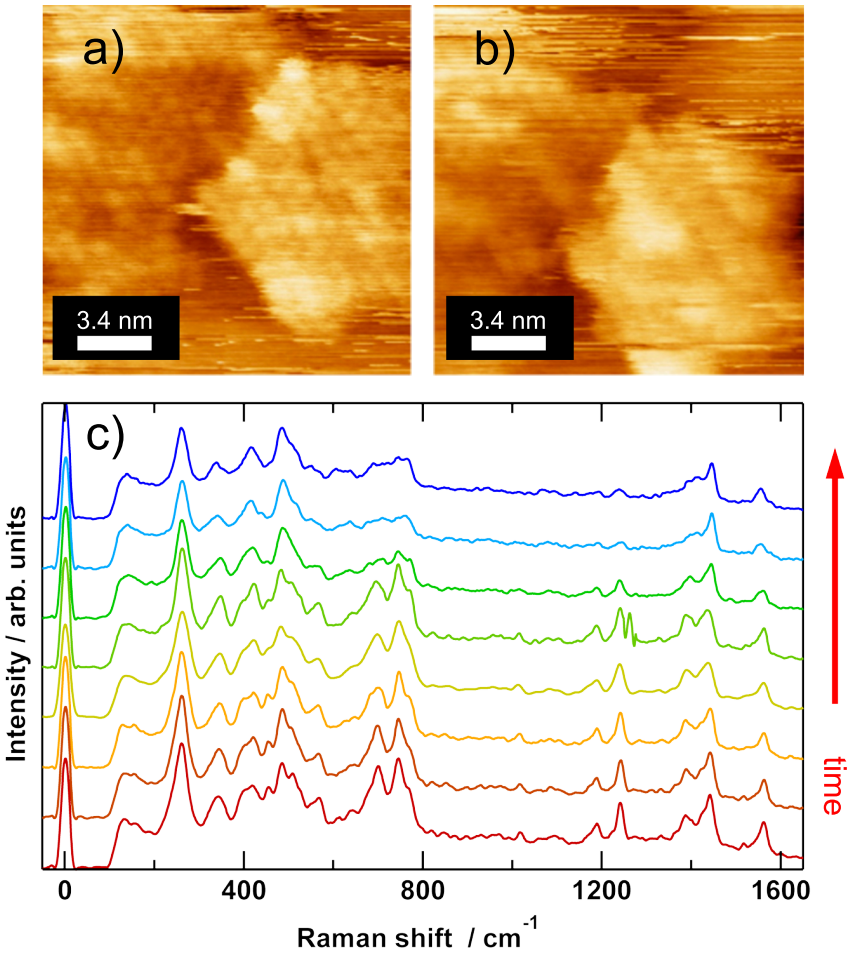

FIGURE 43: Series of STM images and TER spectra of a C_{60} island on Au(111): a) STM images before and b) after the TER spectra were recorded. c) Series of TER spectra. More information is given in the main text. Figure and caption adapted from ref. [41]. Time per spectrum: 8 s. Overlap of neighboring spectra: 3 s. Tunneling conditions: $U_B = 0.3$ V, $I_t = 0.7$ nA

ification of the molecules. During the course of the experiment, the TER intensities dropped in general. In addition, the features just below 800 cm^{-1} loose a large portion of their intensity. Simultaneously, the two peaks around 1200 cm^{-1} vanish almost completely. Hence, both TER spectra and STM images indicate a change in the composition of the C_{60} islands. However, in both, the STM images and the series of TER spectra the main features remain stable. This experiment demonstrates that it is indeed possible to take TERS spectra from C_{60} and correlate them directly with the topographic structure of the adsorbate on the surface.

The next experiment provides evidence that an illumination of a TERS tip during an STM measurement does not necessarily introduce

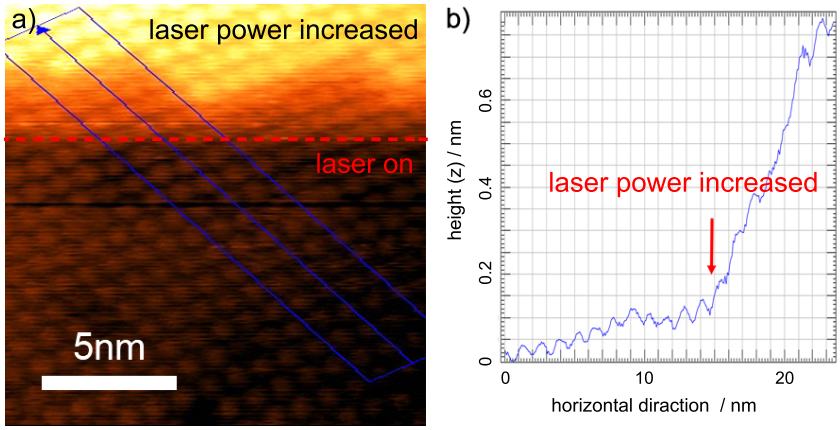

FIGURE 44: STM Image of C_{60} on Au(111) during illumination. a) STM image. At the beginning the laser power is set to about 150 µW. At the position indicated by a red dashed line the laser power is slowly increased to around 500 µW. b) line profile along the direction indicated by the blue arrow in a). Tunneling conditions: $U_B = -2\,V$, $I_t = 0.07\,nA$

changes of the sample. Figure 44 shows STM data of a compact C_{60} monolayer on an Au(111) surface during illumination of the tip. In panel a) the STM image is presented and the hexagonal arrangement of C_{60} molecules is visible. A step edge of the underlying Au(111) surface appears as the zig-zag pattern in the upper quarter of the image. A blue arrow indicates the direction of a line cut through the topographic data presented in panel b). The blue box shows the width that was averaged over to produce the blue trace in b). The laser power was around 150 µW in the lower two thirds of the STM image and was increased to about 500 µW afterwards. This is indicated by the red dashed line in panel a) and the red arrow in panel b). After the laser power is increased the tip expands by about 0.4 nm. This expansion presents itself as an apparent upwards bending of the surface like discussed earlier in the context of Figure 34.

In a third experiment, TER spectra are recorded during the acquisition of STM images. The results are presented in Figure 45. Panel a) and b) show two successive STM images. The imaging conditions are $I_t = 0.1\,nA$ and $U_B = -1\,V$ in both cases. The Au(111) surface shows many narrow steps that are covered by a closed monolayer of C_{60} molecules. There are no major differences between the two images. Most structural details are present in both images. Panel c) shows a time series of TER spectra recorded during and shortly after the two scans. The acquisition time per spectrum is 10 s. The first 22 spectra beneath the first white horizontal line are recorded during the first scan; the next 22 spectra between the two white lines during the second scan. The remaining six spectra are recorded immediately after

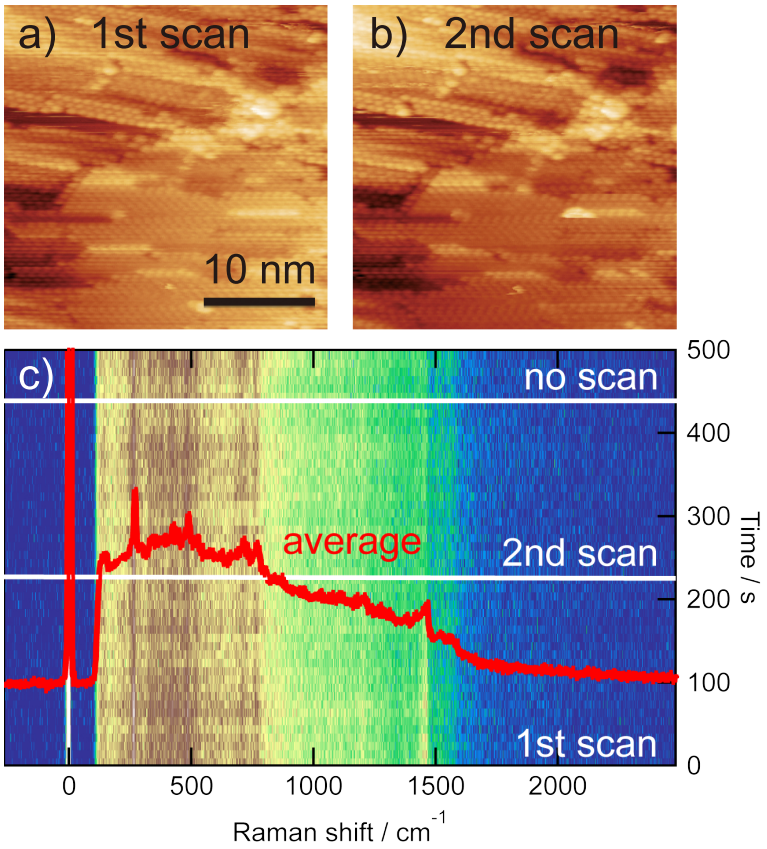

FIGURE 45: Simultaneous STM and TERS measurements. a) and b) are two successively recorded STM images. During and after the scan TER spectra were recorded and are presented in c) as an intensity plot. The white vertical lines in c) indicate the end on the scans. The integration time for each spectrum is 10 s. An average over all 50 spectra is shown as a red trace on top of the intensity plot. Tunneling conditions: $I_t = 0.1\,\text{nA}$, $U_B = -1\,\text{V}$. Laser power about 3 mW.

the scans with the tip at rest in the center of the image under the same tunneling conditions used for the scanning. An average spectrum of the entire series of 500 s duration is displayed as a red trace on top of the intensity plot. The typical features of a TER spectrum of C_{60} are clearly visible. The broad background peaks at low Raman shifts of about $500\,\text{cm}^{-1}$ and declines towards higher Raman shifts. Not only the background but also the Raman peaks are of reduced intensities at higher Raman shifts than closer to the laser line. This observation was already discussed in Section 4.1 in the context of Figure 25. The broad background reflects the plasmon spectrum of the tip-sample configuration. These plasmons are responsible for the TERS effect and lead to TERS EF that depend on energy. Consequently Raman peaks at positions where the background is more intense are also more enhanced than at spectral positions with a lower intensity of the background.

The presented experiment illustrates nicely that simultaneous STM imaging and TERS is possible without introducing changes of the sample like seen in Figure 43.

All three experiments presented in this section show, that simultaneous recording of TERS maps and topographic images is within reach with the current experimental set-up.

5

CONCLUSION AND OUTLOOK

Tip-enhanced Raman spectroscopy (TERS) belongs to the most intriguing recent developments of analytical tools for surface science. For TERS, a sharp tip of suitable material and shape is required that supports the excitation of surface plasmons and, thus, the creation of enhanced near-fields. Such near-field tips act as optical antennas to enhance Raman signals of adsorbed molecules by many orders of magnitude. Controlled by a scanning tunneling microscope (STM), the tip is positioned over the surface of interest and facilitates spectroscopic studies with a spatial resolution in the 10 nm range and, in some cases, even with single-molecule sensitivity.

In this work we have included an existing UHV-TERS module in a larger UHV set-up that allows in situ sample preparation. This allows a fabrication of samples with well defined composition. During the course of this rebuilding, the existing UHV-TERS module was improved considerably in terms of experimental capabilities and manageability. Details are discussed in Chapter 3 and Appendix A. In particular the preparation time for an experiment was considerably reduced by optimizing the adjustment optics and procedure. A time consuming breaking of the vacuum in the case of a misalignment of the optical elements inside the vacuum chamber is avoided by establishing more control over these elements from outside the chamber.

We have chosen C_{60} on Au(111) as a model sample system to test the potential of our device. There exists a large body of literature about the vibrational properties of C_{60}. From STM studies it is known, that C_{60} forms stable, two-dimensional islands of monomolecular thickness at room temperature. If TERS is to be used as a standard tool, it has to allow the investigation of vibrational properties of a wide class of adsorbates, in particular those with small Raman cross-sections. In contrast to the molecules studied in all prior UHV-TERS experiments, C_{60} does not exhibit an resonance Raman effect under our experimental conditions. Compared to BCB for example, the Raman cross-section of C_{60} is four orders of magnitude lower. The detection of TER signals from (sub)monolayers of C_{60} is, hence, a good test for the sensitivity of our device. At the same time, possible contaminations on sample or tip can have comparable or higher Raman cross-sections as C_{60}. In fact we observe a large amount of spectra of unknown origin. To surmount this problem, we record time series of TER spectra. Stable series that show the typical features of C_{60} are

selected for further analysis. A large fraction of rather stable series of C_{60} show undefined peaks that shift continuously in energy. They are interpreted as foreign molecules that diffuse through the TERS area and experience changing interactions with their surrounding.

The recording of time series of TER spectra is also used to investigate the response of TERS from C_{60} on changes of the external parameters tunneling current, bias voltage and tip-sample separation (Section 4.3). While minor changes in the tunneling current leave the spectra unchanged, we find that a change of the bias voltage between -4 and $-600\,\mathrm{mV}$ has a huge effect. The peaks in the higher energy part of the spectrum lose most of the intensity, while the intensities at smaller Raman shifts decrease much less. This effect can be explained by a change of the plasmon resonance in the coupled plasmonic system of gold tip and gold surface due to the alteration of the gap in between them. At smaller bias voltage the tip is closer to the surface and the plasmon resonance is more intense and shifted to the red (higher Raman shifts). The change of this gap-mode plasmon is also reflected in a corresponding change of the shape of the broad TERS background.

An experiment where the tip-sample distance was deliberately altered confirms the strong dependence of the TERS signals on subnanometer changes in the tip-sample distance in the tunneling regime. Previous experiments have so far only investigated the range between 1 and 20 nm tip-sample separation. Our results can prove vital to the interpretation of TERS maps that are recorded simultaneously with topographic images. While recording a topographic image the tip-sample gap is modulated which can have a strong impact on measured TERS intensities.

TER spectra and STM images of C_{60} on Au(111) are analyzed in Section 4.4 for three different surface coverages of C_{60}: I) at small surface density of C_{60} only the step edges of Au(111) are decorated with thin lines of one or two molecules width, II) for a much larger coverage extended islands of C_{60} cover the Au(111) terraces, and III) samples of type II) that are several days old and show major changes in the C_{60} film structure. The hexagonal arrangement of the molecules in two-dimensional islands has disappeared and is replaced by a granular structure. The corresponding TER spectra reflect the differences especially between the fresh sample with extended islands and the aged sample.

The TERS features of the aged sample can be explained by a polymerization of the C_{60} molecules, which can also explain the changes observed in the STM images. The differences between the TER spectra of the step-decorated sample and the polymerized one are very sub-

tle. The relatively low Raman shift for the $A_g(2)$ mode at 1450 cm^{-1} is attributed to C_{60} molecules adsorbed at steps. A shoulder of the $A_g(2)$ mode at 1460 cm^{-1} is interpreted as a contribution of C_{60} molecules an terraces.

However, because of the close resemblance of these spectra with spectra from polymerized samples of type III), a polymerization of type I) sample can not be excluded.

Finally, in Section 4.5, three further experiments were discussed that show that the prerequisites for TERS mapping are fulfilled. The first experiment consists of a series of STM images and TERS measurements of an island of C_{60} molecules adsorbed at an Au(111) step edge. After a first STM image, TER spectra are recorded for about 40 s before a second STM image is taken. The two images show essentially the same features. The structure of the island has only changed slightly and the total number of molecules seems to have changed by a minor amount. Also the series of TER spectra indicates some changes of the Raman features. The main characteristics of C_{60}, however, persists over the entire sequence of spectra.

The second experiment shows an STM image of a closed layer of C_{60} molecules on Au(111) recorded while illuminating the tip. An increase of laser power during the scan presents as an apparent slope in the topographic image that can be attributed to an extension of the STM tip due to heating. This observation shows that the tip is indeed exposed to the laser radiation, but the observed structure of the adsorbate layer is not affected, it remains stable. In the third experiment, a series of TER spectra was acquired during and after two STM images where recorded on a stepped region of a sample covered with a complete monolayer of C_{60}. The STM images have molecular resolution and do not show signs of major changes in the composition of the C_{60} layer. The corresponding TER spectra are very stable over the entire 500 s of the experiment and show the typical features of C_{60}.

The studies presented in this thesis open multiple perspectives for further experiments in the field of UHV-TERS. It was shown that molecules with relatively low Raman cross sections can be investigated with TERS under UHV conditions. A cleaning of the near-field tips in UHV before the experiments is likely to further reduce contributions of contaminations in the spectra.

Experiments with different molecules and substrates could elucidate the mechanism behind the close range distance dependence of TERS spectra that we describe in Section 4.3.

A simultaneous recording of STM images and TERS spectra, as shown in Section 4.5, can help to resolve the question whether C_{60}

molecules adsorbed at step-edges show really a downshifted $A_g(2)$ mode compared to terrace-adsorbed molecules. In particular, if TERS spectra are taken at different positions of the scanned sample area, maps with local vibrational, and hence, chemical information on the 10 nm scale can be produced.

TERS mapping can also shed light on the bias-induced polymerization and fragmentation of adsorbed C_{60} molecules in analogy to that reported by Nakaya *et al.* [113].

A

APPENDIX

The sample holder was described in Chapter 3. In order to facilitate the focussing procedure of the parabolic mirror (PM), it is important to align sample surface and xy-plane of the PM movement. This is achieved by moving three ceramic tubes on the sample holder. The position of these tubes defines in the same time the vertical position of the sample in the STM. This position has to be adjusted as well, in order to allow the STM tip to be approached in the center of the sample. Two tools were constructed to help with these adjustments.

A.1 SAMPLE MOUNT ADJUSTMENT

The *angle adjustment tool* is schematically shown in Figure 46. A laser is coupled to a collimator that produces a wide beam, running upwards. Opposite of the collimator is a mirror with a central bore of 1 cm diameter. Note, the mirror plane and backside of the mirror are parallel. The sample holder is put with the ceramic ends of the screw on the rear side of the mirror. The sample sticks through the hole. The beam passes through a beamsplitter and hits the mirror and the

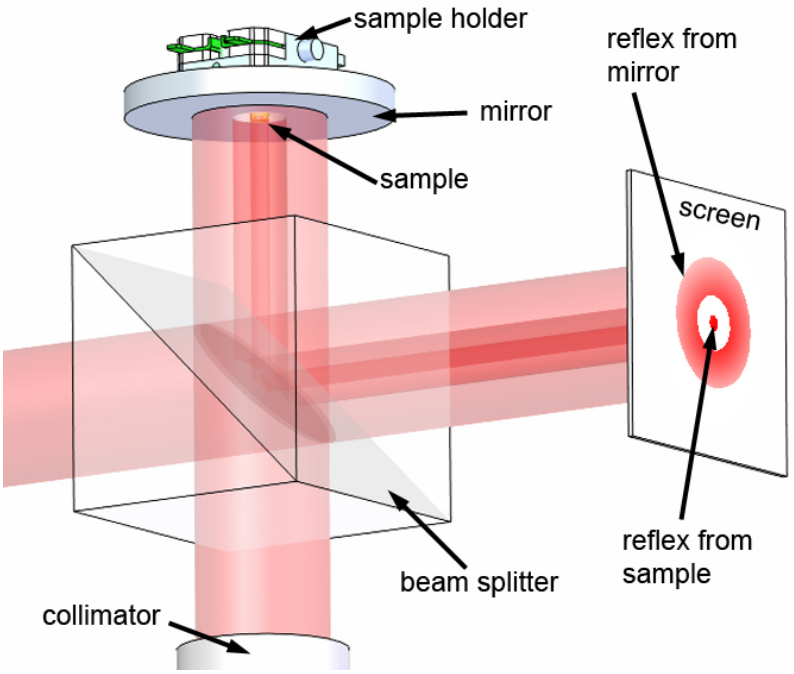

FIGURE 46: Tool to minimize the angle between sample surface and parabolic mirror.

sample. Then it travels back to the beamsplitter. The reflected part is observed on a screen. The reflex from the mirror will appear as a ring because of the bore. The light reflected from the sample is seen as a small spot. By moving the three screws the sample reflex has to be moved into the center of the ring. The sample is then adjusted parallel to the mirror as well as to the plane defined by the three ceramics. Hence, when the sample is moved inside the STM unit, its plane will be also parallel to the scan plane. Next, the sample holder is inserted

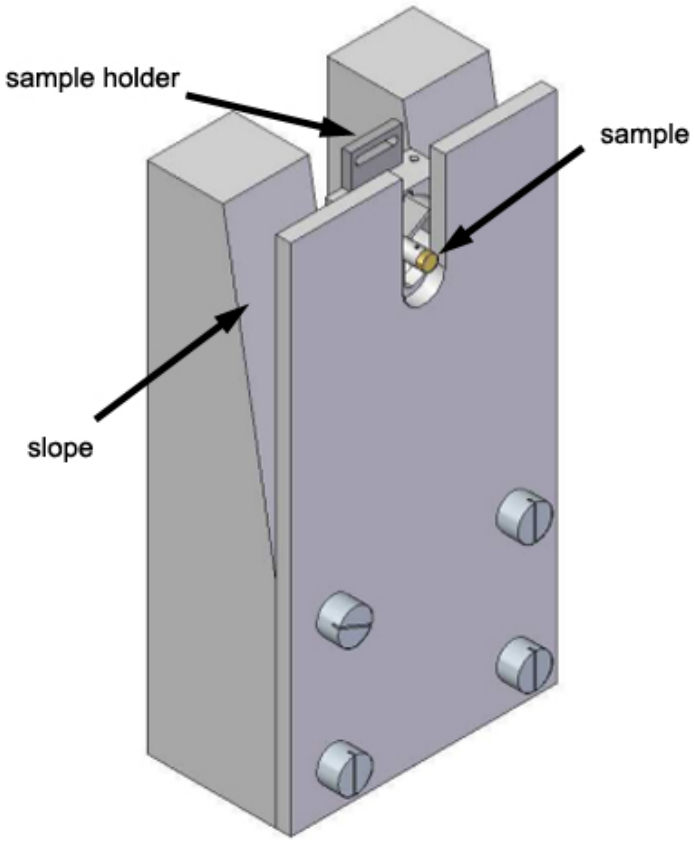

FIGURE 47: Tool for adjusting the vertical position of the sample in the STM.

into the *vertical adjustment tool* Figure 47 to control the vertical position with respect to the parabolic mirror. Turning all the screws by the same amount this can be optimized. The two steps, the adjustment of the angles and of the vertical position, have to be repeated until the desired result is obtained. Each screw is then fixed by a counter screw.

A.2 ADJUSTMENT OF THE OPTICS

In Chapter 3 a short summary of the alignment and focussing of the optical set-up was given. In this section we describe the necessary steps in detail.
As a first step the tip has to be brought as close as possible to the central axis of the parabolic mirror (PM). This is done before the sample is inserted into the STM. Only then there is visual access through the big window (MW200) and the beam splitter (BS) into the inner part of the PM. Let us introduce a new co-ordinate system here referencing to the movements of PM and tip. It is depicted in Figure 16. At the beginning, the mirror must be placed in its most backward position along the z direction. By moving along x and y directions, the PM can be centered around the tip holder. If this is not done , the risk is high that in a later step of the adjustment the PM is moved too far to one side and presses the tip holder against the wall of the hole of the PM (this not only short-cuts the tunneling current, but may also damage the scan tube of the STM). Afterwards, the prepared sample can be inserted.

For the adjustment of the RDH two additional elements are employed. The first is an adjustment laser (AL). The second element is alignment optics that is located mainly outside the vacuum chamber: a beam splitter (BS) on the platform between PM and REF1 directs half of the light (that is reflected/generated by the sample and then reflected by the PM) out of the main chamber through the window (MW200). The rest of the optics is outside. Once the light has passed the window, it is guided by three mirrors (only two, M2 and M3, are shown in the schematic view in Figure 16 for simplicity) onto a lens (L1). A CCD camera is positioned in front of the lens at its focal distance, such that a collimated beam entering the lens produces a small focus spot on the CCD.

The idea of the focusing procedure is that, when a parallel beam is well focussed onto the sample by a PM, then reflected as well as the (inelastically) scattered light emitted by the sample will be converted again to a collimated beam by the PM. This collimated beam produces, as just stated, a small spot on the alignment CCD. In cases where the PM is not focussed, other patterns will appear on the CCD. These are used as a guide to move the PM until it is focussed onto the sample, as described below. When the sensitivity of the CCD is adjusted correspondingly one can work employing very low intensities (below 1 µW) during the alignment process. The intensity of the HeNe laser can be set by an attenuator (At). The intensity of adjustment laser can be altered by an internal device.

The possibility to align the RDH optics by using very low incident intensities represents an improvement over the original adjustment process, where significantly higher laser powers had to be used (in order to detect low intensity reflexes on a simple screen). This ensures that the sample is not exposed to two much light which could lead to some photodegradation of the sample already before a TERS measurement [39, 40].

A diode laser with 660 nm is used as an adjustment laser (AL). It is coupled to a polarization maintaining fiber (PMC3) that is connected to the multi mode (MM1) fiber attached to the second collimator (C2). Because its wavelength is a little longer than that of the HeNe laser, it passes through the Raman edge filters without substantial losses. Next, by moving the PM this beam can be focussed onto the sample. Three piezo motors that walk along the axes of the PM are used to move it towards the sample and adjust its angular position. Initially, on the alignment camera a pattern of ring segments is seen (see Figure 48).

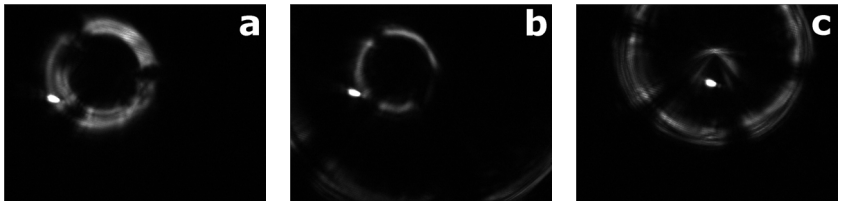

FIGURE 48: First adjustment steps. Images from the alignment camera. The bright small spot stemms from the plane part of the parabolic mirror, the ring pattern from the parabolic part.

Such a pattern indicate that the mirror is so far away from the sample that the incident light misses the sample and that the axes of PM and the collecting collimator C2 are not parallel. Yet, a small part incident light is reflected by about 45° and will travel more or less horizontally to the other side of the PM, is reflected again and sent backwards along the alignment path. This part of light forms the ring pattern in Figure 48a. When moving the PM closer to the sample the pattern shrinks. Eventually a new series of ring segments emerges from the periphery of the CCD chip when light is reflected from the sample (see Figure 48b) and c).

The elongated spot on the images stems from the plane rim of the PM (see description of the sample holder above and Figure 15) and serves as a reference during the focusing procedure. The PM is further moved towards the sample and tilted, such that the reference reflex moves into the center of the ring structure and the ring contracts around it (see Figure 48c).

By continuing the adjustment procedure, the ring system is further shrunk and the sensitivity of the CCD is adjusted to compensate for the increase in light density due to the focusing) until a circular spot of minimal size is seen, that coincides with the reference reflex (see the transition from Figure 49a to Figure 49b).

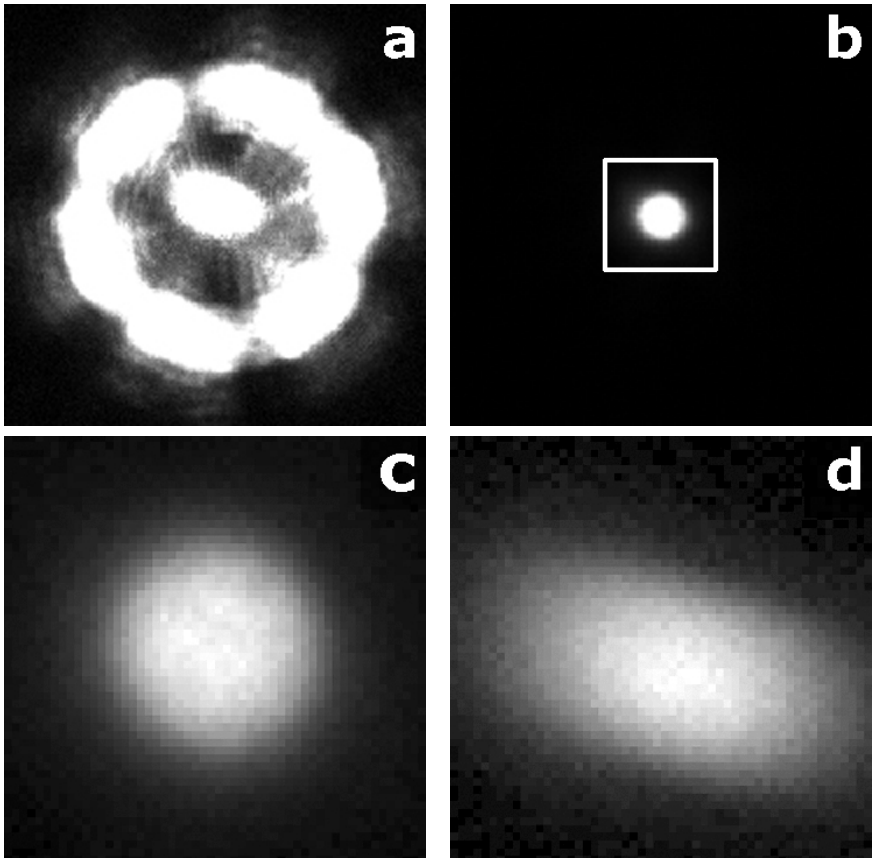

FIGURE 49: Comparison of pattern for slightly defocussed and fully focussed parabolic mirror. a) slightly defocused and b) focused parabolic mirror. c) enlarged view of the area indicated by the white square in b). d) reference reflex when light from parabolic mirror is blocked.

To check the adjustment, the part of the light reflected from the parabolic part of the mirror must be blocked. Only the reference reflex should then be visible at the same position. And vice versa, when the reference reflex is blocked (compare Figure 49c with Figure 49d.

At this stage, the adjustment laser is focused onto the sample and light emitted from the focal region can be collected into the fiber MM1. Once it is re-connected to the spectrograph via MM2 recording of spectra is possible, i.e. the adjustment of the light collecting path is done. But a second adjustment procedure needs to be com-

pleted: Getting the incident HeNe laser light into the focus.

For that purpose the shutter of the HeNe laser is opened and two more reflexes appear. One from the parabolic and one from the plane part of the mirror, Figure 50a. At that stage it is important to make the axis of the incident HeNe beam parallel to that of the PM (which is already adjusted).

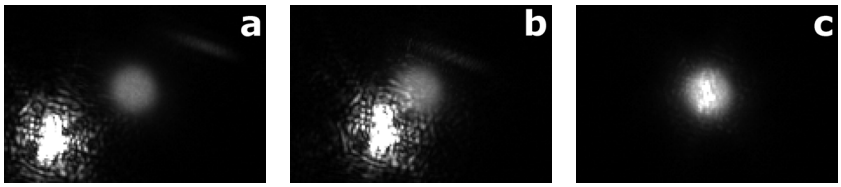

FIGURE 50: Alignment of HeNe laser with axis of the parabolic mirror. a) apart, b) close, c) aligned.

By moving the piezo controlled Raman edge filer (REF1) and plane mirror (M1) the angle between these two axes can be minimized (see Figure 50a, b and c).

If successful, the focus of the HeNe coincides with that of the adjustment laser. The final adjustment is accomplished when all four spots are at the same position like shown in Figure 50c.

One can see now the diffuse spot of the AL in the background of the sharper spot from the HeNe. In the latter case the four individual spots appear when only one of the lasers illuminates the sample and the reflexes of the PM are either blocked ore not. In this configuration it is already possible to make normal Raman experiments.

The final step that is needed before a TERS measurement can be performed is to bring the focus onto the tip. To do this an additional lens (L2) is inserted into the adjustment optics between L1 and the CCD. It moves the focus of the beam away from the CCD, so that on the CCD a cross section of the diverging beam is recorded. Figure 51a) shows this cross section: a disk with six shadows, like spokes in a wheel, with an angle of 60° between them. Three of them are produced from the three bars of the sample holder before the light arrives at the PM. The three others are created after the light is reflected from the PM, from the sample and from the PM again, when the light passes the sample holder on the way to the collecting collimator (C2).

For the next step, the tip is a approached to the sample. Once the tip it is in tunneling contact, the feedback of the STM is switched off and the tip is retracted with the z-piezo of the scanner as far as possible. The tip apex is now several 100 nm away from the surface. It can not

be left in tunneling because the noise introduced by the step motion of the PM would cause the tip to crash into the sample. When the tip is in this position it intersects the beam converging towards the focus and the diverging beam reflected from the sample, thus producing two new shadows in Figure 51b.

Moving the PM along the horizontal (vertical) axes these shadows will move, like the hands of a watch, towards the vertical (horizontal) axes when the tip gets closer to the focus (see Figure 51b). In close proximity to the focus the tip-shadows vanish because most of the tip holder and the tip wire has entered the conical volume along the central axis of the PM that is not illuminated due to the shadow of the sample. Yet, a large amount of the incident light is scattered by the tapered part of the tip close to its apex. This elastic scattering causes also the first three shadows to disappear. Figure 51c shows this stage of the focusing process: a disc with three shadows caused by the bars of the sample holder after the light has left the PM. The tip is now already very close to the focus.

For the final step of the focusing L2 is removed from the adjustment optics. The resulting image is shown in Figure 52b.

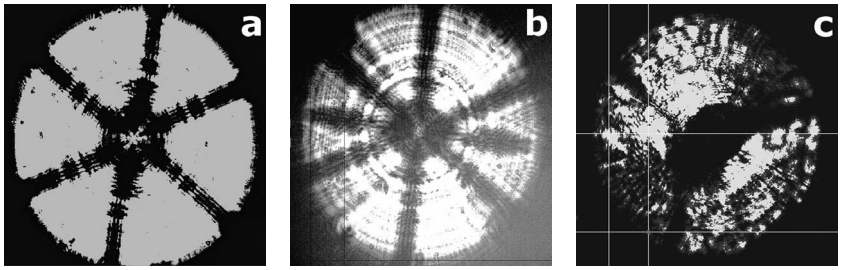

FIGURE 51: Light pattern depending on the distance of the tip to the focal region: a) tip far from the focus. b) Tip some µm away from the focus. c) Tip close to the focus or in the focus. The shadow of the tip is not longer visible because most of the tip is in the shadow of the sample. Due to the scattering of the incoming light from the tip also the first three shadows are lost. They are created by the bars of the sample holder when the incident light passes them the first time. The three remaining shadows stem from the sample holder after the light has left the PM.

The central region shows the ring structure of a slightly defocused PM. Towards its upper right there is an interference pattern of the light scattered by the tip. Moving the PM along x and y the pattern will follow the movement until the center of the pattern coincides with the reflex from the focus. For the case that the PM is slightly defocused, the procedure of focusing the mirror and moving the focus onto the tip has to repeated several times before an optimal result is reached. At this point two of the aforementioned improvements become very important. I) the tilt angle between the sample surface and the x,y plane of the mirror movement should be as small as possible to ensure that during the x and y movement the focus does not drift too far away from the sample. This is ensured by aligning the sample in the sample holder with the angel adjustment tool (see Figure 46). II) The tip has to be as close to the center of the PM axes as possible before the focusing starts. Here, the new design of tip holders is very helpful, because it avoids to clamp the tip wire into too big a bore, which causes it to be off center. It is also important to ensure that both the mirror and the tip are centered along the common central axis as much as possible before the focusing procedure is started.

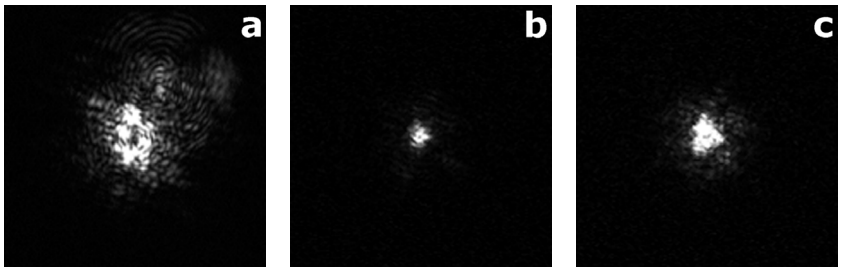

FIGURE 52: Images of the focused situation from the adjustment camera. a) The parabolic mirror is slightly defocused and the tip is displaced from the center. The reflection of the tip appears to the upper right of the focus as a series of interference circles. b) Shape of the focus, when the tip is retracted by three steps of the piezo motor (ca. 3µm). c) The tip is approached to the sample in the center of the focus.

Finally, the focus looks like in Figure 52c). In panel b) the tip is retracted by three steps of the piezo motor. In panel c) the tip is approached to the sample. The spot has clearly increased in size and intensity.

Note: the situation can look slightly different every time. Probably due to different tip shapes, positions of the sample holder and exact placement of the parabolic mirror. But the general patterns can be recognized.

At this final stage, both the incoming HeNe laser and the AL are focused onto the tip. Once the MM has been disconnected from the AL and reconnected to the spectrograph, spectra can be recorded. Thus,

TERS, photon STM and other tip-enhanced studies can be performed. For the photon STM no exciting laser is needed. Hence, the steps involving the HeNe laser can be omitted in the procedure and the AL can be used to focus onto the tip.

A.3 TERS TIPS

For TERS, as the name already suggests, tips play a very important role. Their ability to enhance the Raman signal by several orders of magnitude decides over success or failure of the experiment. During TERS experiments under ambient conditions it is usually not difficult to exchange a tip if it does not work. For a UHV-TERS set-up like the one we are using a tip exchange is much more complicated for several reasons: a) the old tip has first to be removed from the vacuum chamber using the linear transfer and load lock system; b) a new tip has to be inserted, again via the load lock and linear transfer system including pumping down. c) re-alignment of optics and PM is required. The whole exchange process usually takes half a day. While already in normal TERS experiments a method for the reliable production of TERS active tips is important, for the UHV-TERS it is even more crucial due to the reasons just stated. The problem of producing reliable tips for TERS experiments is not yet resolved. Wang *et al.* write in ref. [114]:

"It should be noted that even after several years' development of TERS, how to produce TERS tips with high quality and reproducibility is still a central problem bothering most TERS scientists. Therefore, it is not surprising that at the SM-SERS and TERS symposium held in Tsukuba in 2006, the concluding remark was 'tip, tip, and tip!!!.' "

Although, the method they describe in the same paper is an important progress towards reliable tips, the above statement is still valid today.

In TERS experiments tips play a double role. For one, they are used in the STM (or AFM in other set-ups) for the topographic imaging of the surface. For this purpose, (STM) tips must have a sufficient electrical conductivity along the tip shaft, mechanical stability and suitable atomic structure at the tip apex, in the sense that the tip end is made of a single atom that protrudes far enough below all the others. This atom is the closest to the sample. Most of the tunneling current will then flow through this atom due to the exponential distance dependence of the tunneling effect. Because of this it is possible a achieve fairly good STM images with tips that are simply cut with a scissor from a piece of wire. In a TERS experiment the tip has to fulfill a second requirement: it has to work, in accord with the sample and the surrounding medium, as a excellent near-field antenna permitting plasmonic excitations. Essentially, the efficiency of this antenna is determined by its plasmon mode density that depends on a number of parameters: on the material and the shape of the tip at the scale of several nanometers to micrometers, on the material and the shape of the sample (whether it is flat sample or a nanometer sized particle or a cluster of nanoparticles); quite important is also the gap between tip

and the sample. In order to create an sufficient enhancement, the plasmon mode density has to be high for both, the frequency of the laser and the frequencies of the inelastically scattered light that is to be observed. We use a HeNe laser of 632.8 nm wavelength. The Raman lines to be observed are shifted by about -100 to $-2500\,\mathrm{cm}^{-1}$. Hence, the plasmon mode density should be high in a region between 632.8 and 750 nm. In this region gold and silver are almost equally strong in plasmonic activity. Gold is chosen as a tip material because it is less reactive than silver and does not form oxide layers. For the same reason and because it is rather easy to clean from undesired adsorbates, the (111) surface of single crystalline gold has been chosen as the substrate for the C_{60} (sub)monolayers.

Most research groups working in TERS use one of two different types of tip preparation. The first is evaporation of silver or gold onto some tip like a silicon cantilever of an AFM or a tungsten tip. The nobel metal forms randomly distributed clusters on the surface of the tip. These work as an assembly as the optical antenna. The second common class of tip producing techniques are based on the electrochemical etching from gold or silver wires. Electrochemically etched Au tips are also used in this work. The general shape of these tips is a conus that terminates in a semi-sphere forming the tip apex. The cone angle, the radius of the apex but also the crystalline structure of the tip and its surface roughness determine the plasmonic properties. The shape of the tips can be determined by scanning electron microscopy (SEM). However, during the SEM imaging a carbon layer grows on the tip surface. Such tips can produce intense SER and TER signals of amorphous carbon and would disturbe the TERS measurements. Thus, tips that were in the SEM were not used in our experiments. Instead tip etching methods are developed that produce reliable tips with high yields. For TERS experiments tips produced with the most reliable method are used, but not studied with SEM.[1]

Unfortunately, a presumably appropriate shape of the tip alone does not guarantee its suitability as a TERS tip. Many groups report this phenomenon. For example Hartschuh *et al.* write [92]: "Even though all metal tips were fabricated using the same procedure and appeared equally sharp in scanning electron microscopy images, the observed enhancement factors varied from tip to tip. In fact, only 20-30% of the tips we studied produced an appreciable enhancement." Tips are mostly etched from as purchased wires. Due to the wire production through drawing, they consist of small crystalline grains with stress build up within them. Roy *et al.* report [116] that if the grain

1 A possibility of using tips after their characterization with SEM would be to remove the carbon layer. To some extend this can be done by plasma etching. But a corresponding device is not available in our laboratory. Another option would be to sputter clean the tip. This technique can also be used to further sharpen the tips [115].

size is comparable to or smaller than the wavelength of the electron oscillations this influences the plasmonic structure of the produced tips. They note that annealed Au wires have much bigger grains and less stress. Tips etched from these have a higher chance of having a single crystal tip end, which leads to more reliable TERS activity.

We have used both, as purchased and flame annealed Au wires for tip-etching. Annealed gold wire, however, is very soft and difficult to handle. Especially, it is quite delicate to mount such soft tips into the tip holders with the success rate being near zero. The tips used in our experiments are all etched from the untreated wire.

The first method we have investigated is that of Bin Ren *et al.* [117] and its improvement by Wang *et al.* [114]. A 10 ml glass beaker is filled with the etching solution, a 1:1 mixture ofe pure ethanol and fuming HCl. A gold ring of 2 cm diameter from 1 mm Au wire is placed in the surface of the solution. A piece of Au wire of 0.25 mm diameter is vertically centered in the ring and submerged by 2 mm below the surface of the solution. Between ring and tip-wire a voltage of 2.3 V is applied, with the tip being positive polarized. Two different power supplies have been compared. The first is manufactured by the electronic laboratory (Elab) of the FHI. It includes an electronic switch that opens the etching circuit once the etching current drops below a pre-set value to prevent over-etching of the tip. The second power supply is a potentiostat as described in ref. [114]. It is connected to an external switch box that also opens the etching circuit when a current threshold is underrun. The difference here is that the voltage is held very reliably at a constant value with the potentiostat. By employing the potentiostatic power supply and applying a suitable constant voltage, the etching process is accompanied with current oscillations like those described in ref. [114, 117]. A typical current signal of an entire etching cycle is presented in Figure 53.

The oscillations are offset from zero current by a monotonously declining background value. The appearance of the oscillations indicates that the etching process happens synchronously over a large part of the surface of the wire. Otherwise only an average current would be recorded. The oscillations are a consequence of the formation and dissolution of an AuCl film that passivates the Au surface [114, 117, 118].

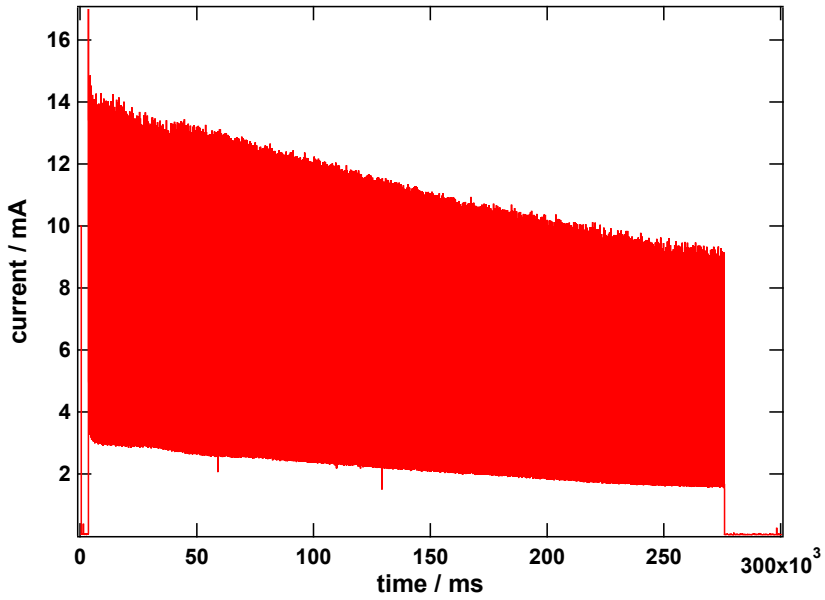

FIGURE 53: Current oscillations recorded during the etching of the tip presented in Figure 59. The entire etching process takes about 4.5 min. The current drops to zero when the switch opens the etching circuit after the final piece of the tip wire has fallen off.

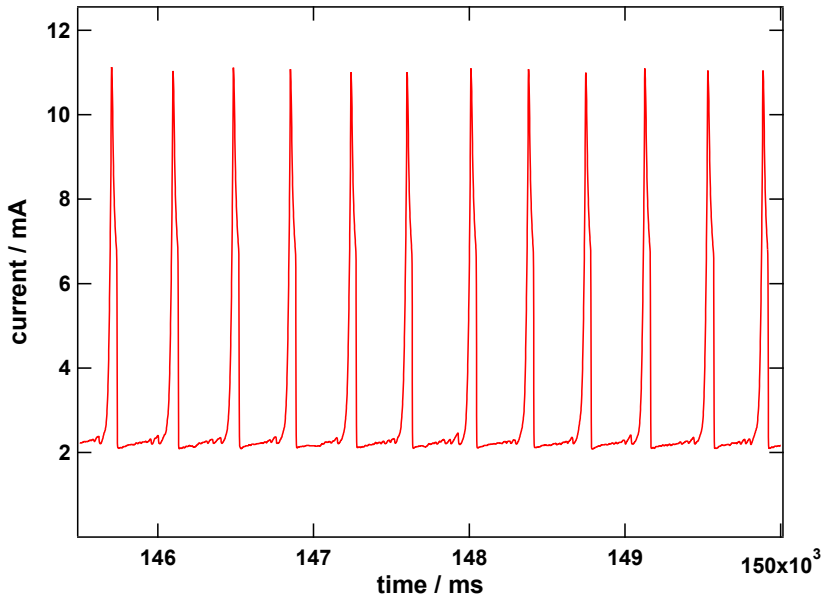

FIGURE 54: Higher time resolution of an area in the middle of the etching cycle. Evenly spaced peaks indicate a homogeneous etching of the wire.

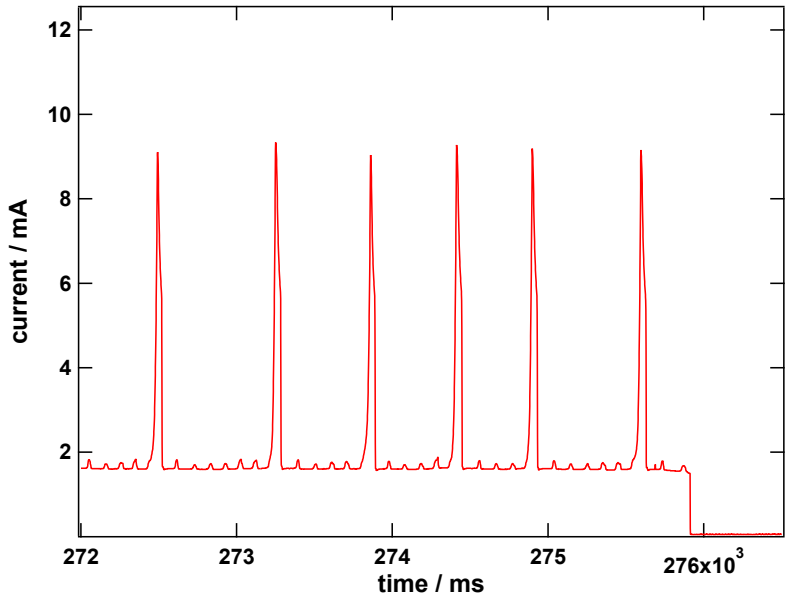

FIGURE 55: End of the etching cycle. The peaks are wider spaced than at earlier times during the etching (Figure 54). Smaller, evenly spaced peaks have appeared between the main etching peaks. These indicate that the tip is about to break. The sharp drop of the current at the right is the opening of the switch that prevents over-etching of the tip. The threshold was set just below the current base line of 1.5 mA.

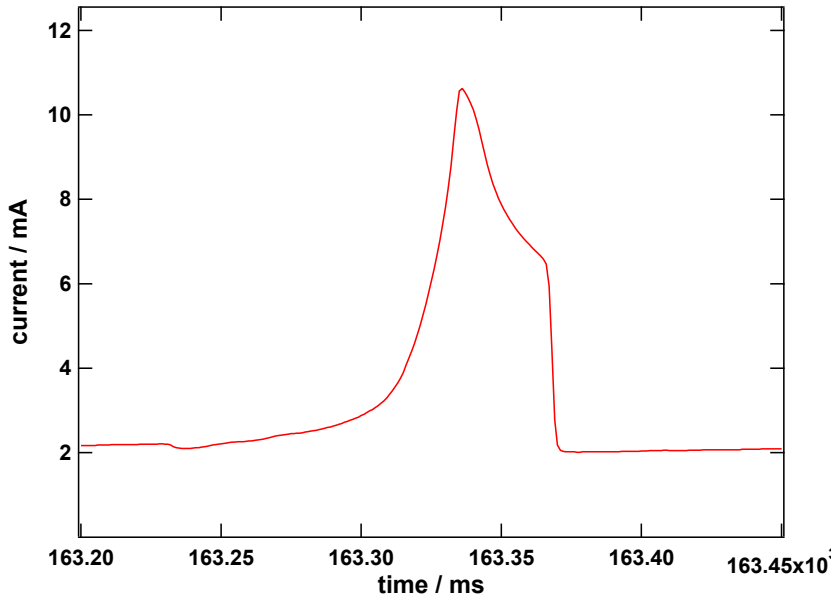

FIGURE 56: Close view of one current peak during the etching process.

It takes about 4.5 to 6 min to prepare one tip with this method. If the etching process is stopped before the final piece of the wire drops off, the etched wire looks like in Figure 57 and Figure 58 (all images of tips are presented at the very end of this section). The lower part of the wire is homogeneously etched into a thinner cylinder. In the meniscus region where the wire gets in contact with the electrolyte surface, the wire is tapered but has a rather rough surface. In this region, the etching speed seems to be faster.

Towards the end of the etching process (Figure 55), the peaks of the oscillations are spaced wider apart than at earlier times (Figure 54) and a number of equally spaced smaller peaks appear between two of the major ones. This can be used as an indicator that the wire is about to break. When the lower part finally tears off the current suddenly drops and the switch opens the circuit. Hence, the etching is stopped instantly to preserve a sharp tip end.

While we where able to produce good tips also with the first voltage supply (Figure 59) the employment of the potentiostat and the monitoring of the current oscillations have allowed us to adjust the etching parameters. As a result, five out of six tips have smooth surfaces and small tip radii of below 40 nm, four of them around 20 nm.

Images of tips prepared with as purchased wire are shown in Figure 59 for the potentiostat and in Figure 60 for the Elab voltage supply. The tip shown in Figure 59 has been fabricated during the etching process shown in Figure 53 through Figure 56.

Tips made of flame annealed Au wire were only produced with the Elab power supply; therefore, no information of the current response during the etching is available. In Figure 61 and Figure 62 three images of such a tip at different scales are shown.

On the large scale (Figure 61) clearly large crystallites of up to 100 µm in size are seen. The etching process seems to work preferentially along certain crystal directions and at grain boundaries. As a result smooth surfaces and sharp edges are observed. Striking is the observation that the roughness seen on the upper part of the taper of tips from non-treated Au wire (Figure 58) are not present in the annealed tips. Especially the holes along the wire axes have disappeared. This points to the fact that these features are caused by preferential etching along certain crystal directions and that the crystallites in the not annealed wire are elongated along the wire axes and rather small (several 100 nm) in diameter. Although some grain boundaries in the former type are clearly visible, it could still be possible that not all boundaries are seen. To further analyze this it would be necessary to perform an electron backscattered diffraction analysis, like done in ref. [116]. The authors of this paper conclude that tips that were etched from annealed wires are likely to have a single crystal at their

end. They note that these tips are more reliable in TERS experiments than others. However, they do not discuss wether there is a difference in TERS quality for different crystal orientations of the tip end.

Figure 63 and Figure 64 shows another tip prepared from annealed wire. It exhibits a much higher surface roughness than the example shown before. This difference could be a consequence of different crystal orientations and preferential etching along certain crystal axes. It would be very interesting to test these tips in TERS experiments and to determine the crystal orientations to find an answer to the question how to produce reliable tips for TERS. For the technical reasons stated above this was not done.

Too large a surface roughness, in particular close to the tip apex, may cause another problem: SERS signals from possible contaminations of the tip surface.

The observation that the surface of the piece of the wire that was submerged into the solution during the etching is smoother than the rest led to the idea to try a two-step process of tip etching based on the above technique. The tip is first etched like before. But before the tip cuts off the etching is stopped and re-started after the wire is submerged a little bit further into the solution. The idea here is that the smoother etching process that works on the submerged part will now finish the etching, thus yielding smoother tip tapers. SEM images of such a tip are displayed in Figure 65.

The surface of the tip is indeed smooth over a much larger length. A second neck has formed, like expected, higher up the wire. The final tip, however, is rather blunt. So this route was not further pursued.

The second etching method that was tested is the one of Eisele *et al.* [119]. A 90 % aqueous solution of KCl is used as the etchant. The set-up is composed of two platinum rings that are positioned in a vertical distance of 7 mm from each other. The Au wire is placed in the center of both rings. Each ring is wetted with the etching solution. Between the upper ring and the tip wire a voltage of 10 V is applied, the tip being positive. The lower ring serves as an indicator if the wire is cut: once it is cut, a circuit that is closed between the tip wire and the lower ring is opened, because the lower part of the wire has dropped. Using the same switch-off box as in the first method, the etching circuit is opened to avoid over-etching. Eisele *et al.* reports that for 0.1 mm Au wire the etching takes about 10 min and the lamellas in the rings have to be re-wetted up to 8 times.

As in our set-up tips of 0.25 mm diameter are required, we have tested the method with wires of this diameter. Naturally, the etching takes much longer (~1 h) and the lamellas have to be re-wetted with etchant much more often. For this reason this modification of the method is rather time consuming. Another problem was that while the tip is smoothly etched at the upper lamella, it was also etched about 1 mm above at a second point. The etching there was much rougher and often caused the wire to break at this point, not the desired one, leaving a frayed end of the wire that could not be called a tip. This problem could be solved by cleaning the wire every time the lamella broke with a beam of ultra pure water. This was done to wash off a yellow bead that formed during the etching process above the upper ring on the Au wire that was assumed to be responsible for the unwanted etching.

An image of a tip prepared with this method is presented in Figure 66. Panel a) shows the almost perfect cone of the last 50 µm of the tip. The surface appears very smooth. Apparently, there seems to be no preferential etching like in the first method described above. The dents on the last 10 µm are probably from imperfections like microfractures in the wire used. In panel b) the last µm is shown. The radius of the tip end is about 40 nm.

Both the surface smoothness and the sharpness of the tip are of desired qualities for TERS experiments, but this technique is very time consuming and high-maintenance. Therefore, we have not followed this investigation further.

For the second etching method, there seems to be no preferential etching of certain crystal directions, while the first one is more easy to handle and in particular does not need maintainence during the etching. Thus, we have tested a combination of the two. The set-up of the first (one ring in the surface of the etching solution in a beaker) is used with the etchant (aqueous solution of KCl) solution of the second. No faster etching at the miniscus is observed but rather the entire wire that is submerged into the solution is homogeneously etched. Consequently no neck in the wire is formed that would lead to a braking of the wire and the formation of a sharp tip. Obviously, this technique is not suitable for tip preparation.

As a conclusion, for our purposes, the etching after Wang *et al.* [114] provides the best way to produce good tips in a reliable fashion and with justifiable effort.

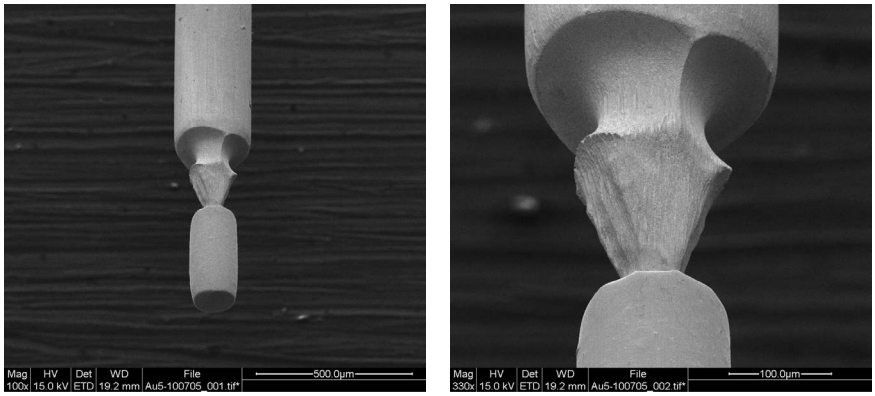

FIGURE 57: SEM image of the result of the etching process when it is stopped before the final end of the wire has dropped. The wire was not annealed before the etching. A neck was etched into the wire where a miniscus of the solution had formed on the wire. The downwards pointing taper in the center will eventually form into the tip. The step in the taper is caused by a slipping of the miniscus during the process. The part of the wire that was submerged into the solution during the etching is evenly etched into a smooth cylinder.

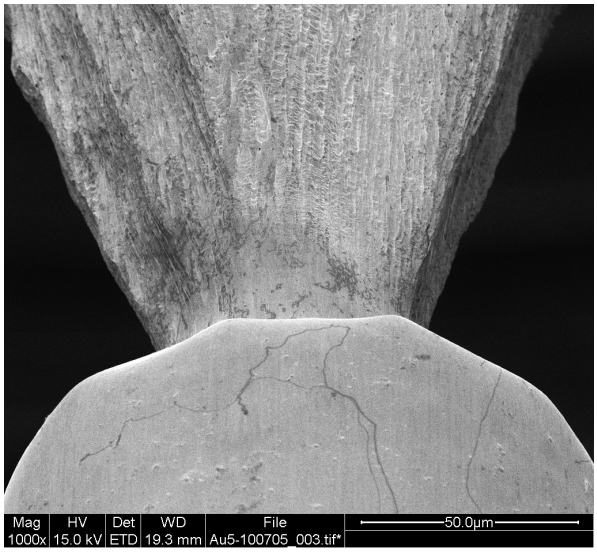

FIGURE 58: Close-up view of the unfinished tip presented in Figure 57. There is a large difference in the roughness between the conical part at the top and the cylinder at the bottom. The surface of the taper is structured with vertical grooves. Also tiny pores along the wire axes can be seen. These features are a consequence of preferential etching of certain crystal direction. See the discussion in the text for more details

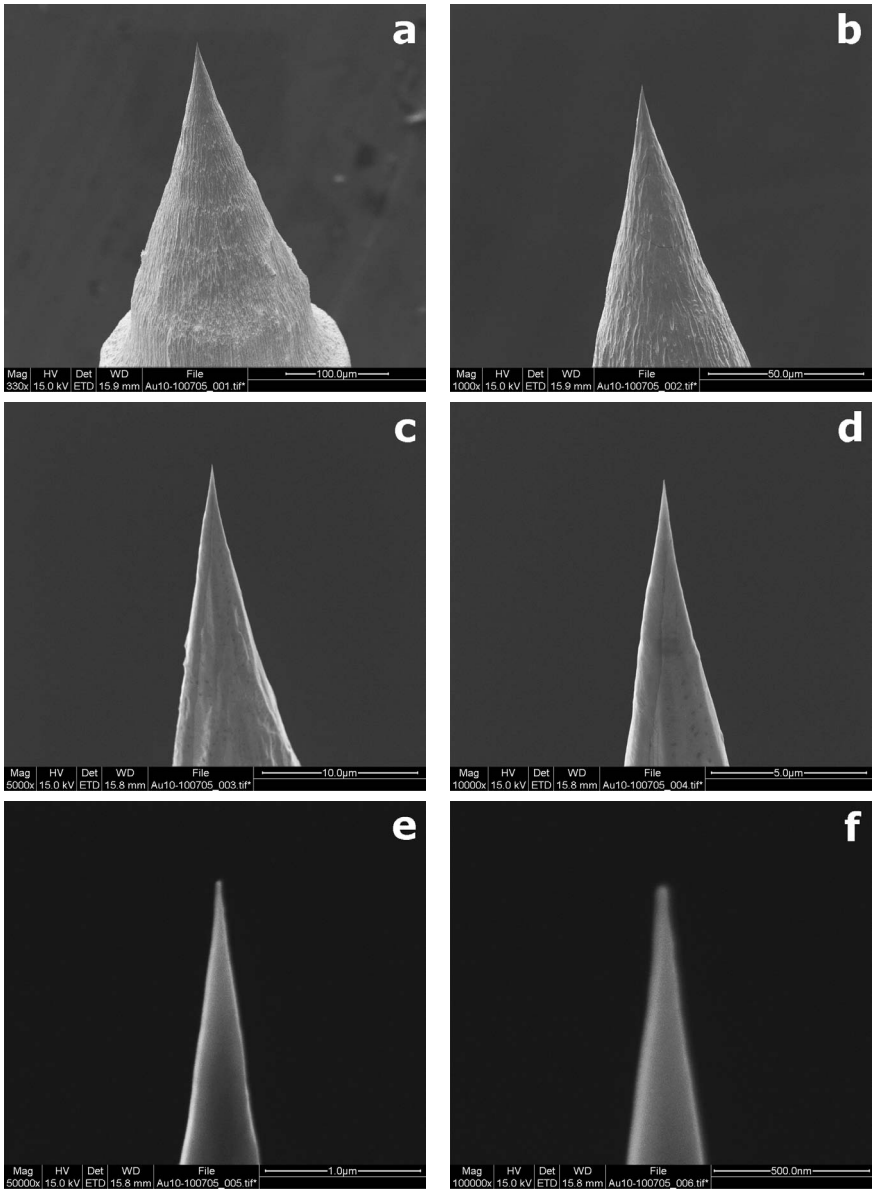

FIGURE 59: Series of SEM images of a tip etched with the potentiostat as power supply from an as purchased drawn Au wire. During the etching of this tip, the current oscillations displayed in Figure 57 were obtained. The magnification increases from the upper left to the lower right. On the larger scales (a) through c)) the roughness of the cone-surface can be seen. The last 10 µm, d), of the tip have a very smooth surface. Especially the last 2 µm shown in e) form a almost perfect cone. From the highest resolution image, f), the radius of the tip is determined to 20 nm.

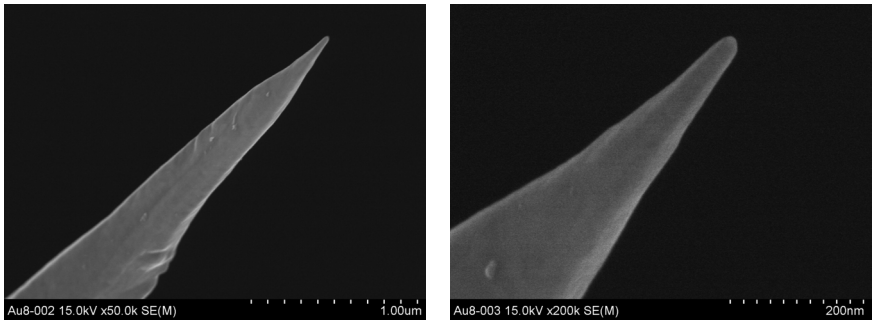

FIGURE 60: Two SEM images of a tip etched with the Elab power supply from an as purchased drawn Au wire. Left panel: the surface is smooth over the last µm. Right panel: the radius of the tip as determined by the image in panel b) is about 40 nm.

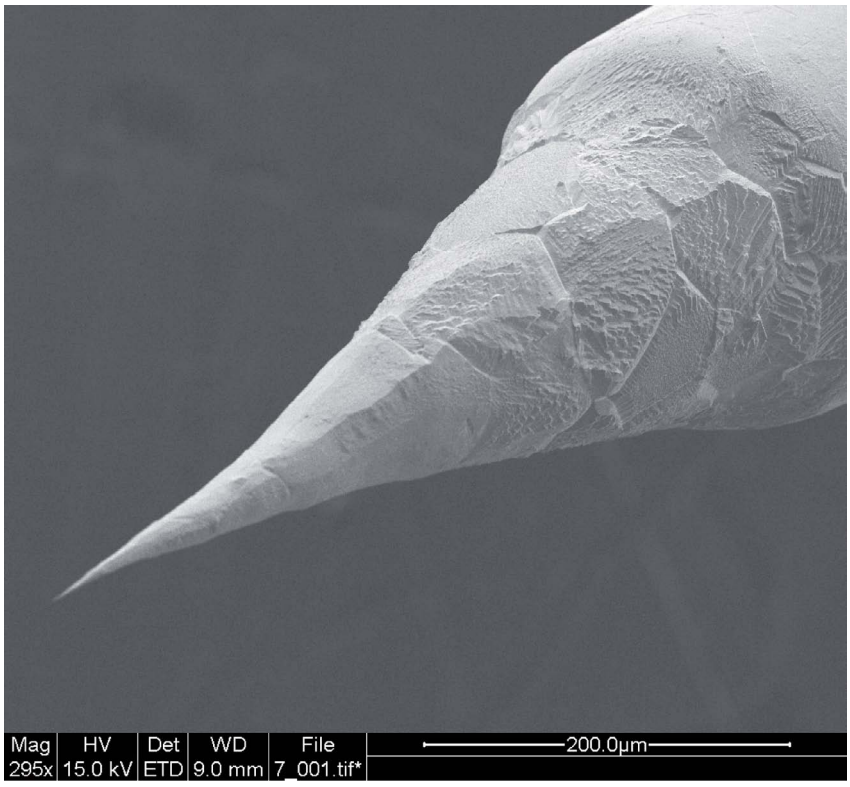

FIGURE 61: Large scale SEM image of a tip etched from a flame annealed Au wire. Large crystallites of up to 100 µm are visible. The surface structure is completely different than that of non annealed tips (see Figure 58 and Figure 59). Different crystal orientations can be inferred from the step patterns of individual grains.

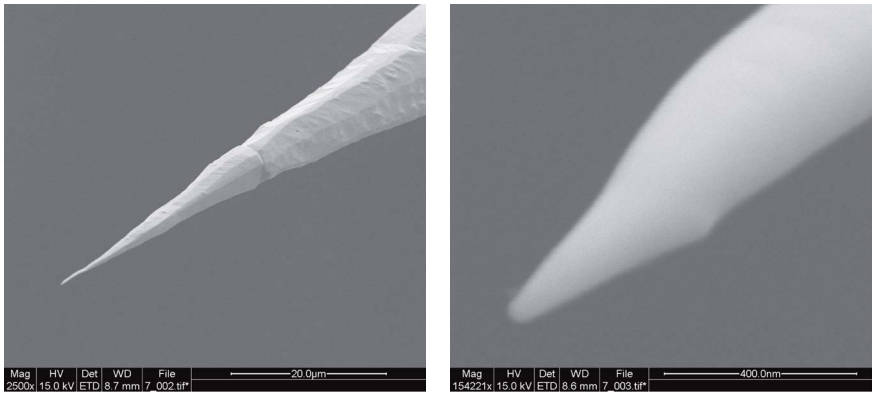

FIGURE 62: Higher resolution SEM images of the same tip as in Figure 61. In the left panel different crystal facets and a single grain boundary 30 µm from the tip end are seen. The right panel shows the smooth tip end with a radius of 25 nm.

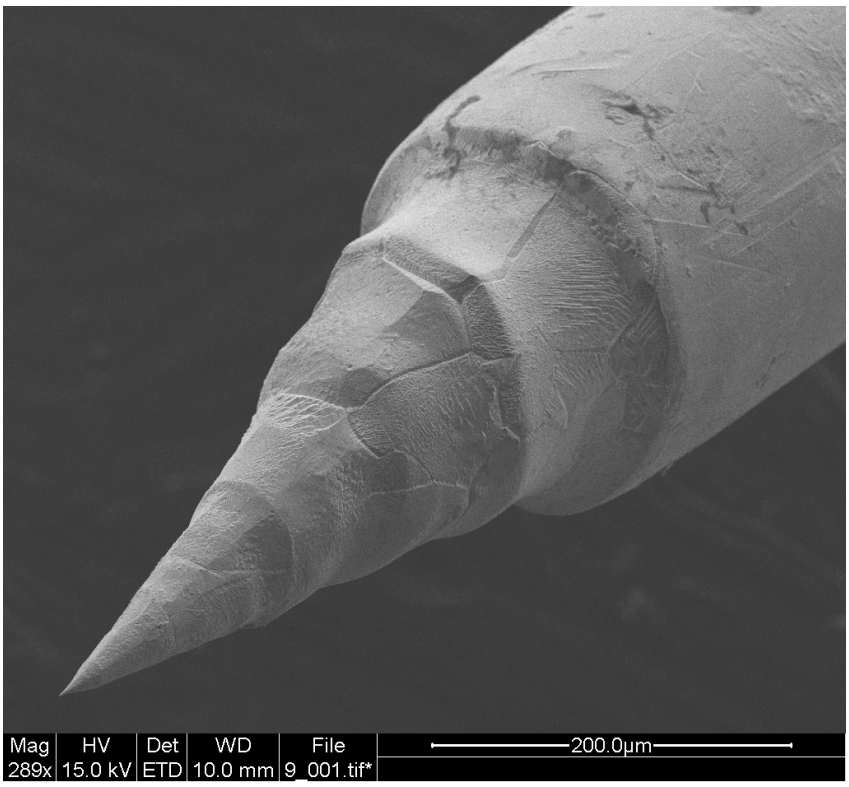

FIGURE 63: SEM image of another tip etched from a flame annealed Au wire. Again grain boundaries and different crystal faces can be seen.

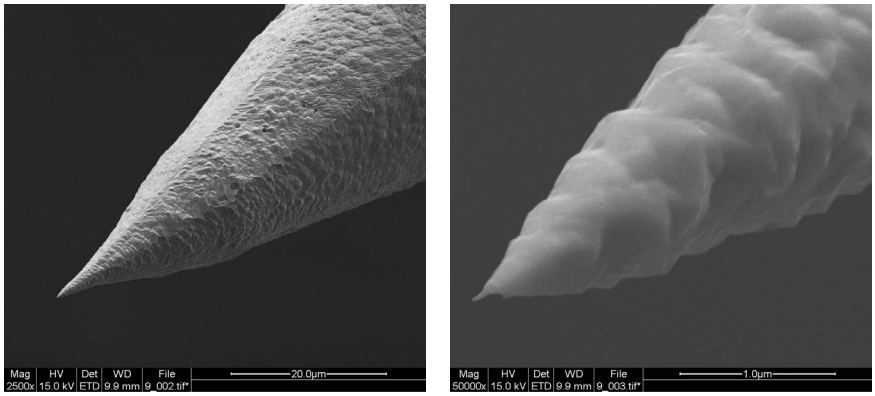

FIGURE 64: Higher resolution SEM images of the same tip as in Figure 63. The left panel shows the last 50 µm. The surface is clearly much rougher than for the tip in Figure 62. This is probably a result of the orientation of the crystals in that region and of a etching mechanism that works preferentially in particular crystal directions. The right panel shows a very fine tip end of about 10 nm radius, although the material near the end consists of bumps of several 100 nm in size.

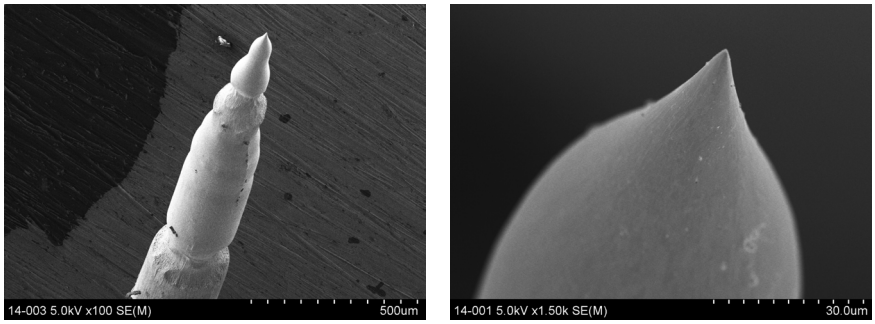

FIGURE 65: SEM images of a tip etched with the two step etching process described above. The shape is even and the surface is very smooth, but the tip radius inferred from the right panel is about 1 µm.

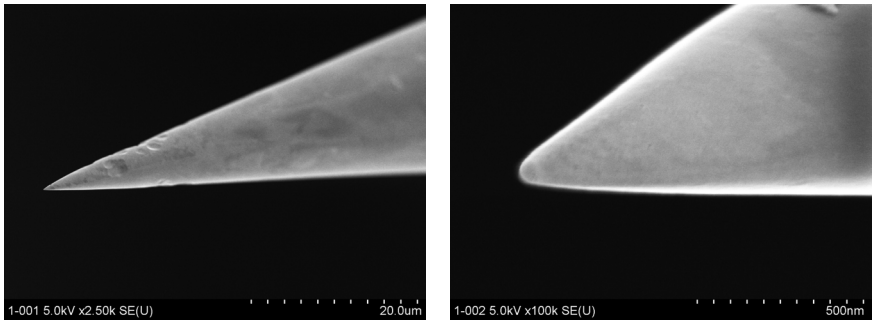

FIGURE 66: SEM images of a tip prepared by etching with KCl solution. Left panel: the last 50 µm have an almost perfect conical shape. Right panel: both smoothness of the surface and radius (40 nm) are promising for TERS.

BIBLIOGRAPHY

[1] C. V. Raman and K. S. Krishnan. A New Type of Secondary Radiation. *Nature*, 121(3048):501–502, March 1928. (Cited on pages 1 and 14.)

[2] C. V. Raman. A Change of Wave-length in Light Scattering. *Nature*, 121(3051):619–619, April 1928.

[3] C. V. Raman and K. S. Krishnan. A new class of spectra due to secondary radiation. *Indian Journal of Physics*, 2:399–419, 1928. (Cited on pages 1 and 14.)

[4] M. Schmitt and J. Popp. Raman spectroscopy at the beginning of the twenty-first century. *Journal of Raman Spectroscopy*, 37(1-3):20–28, January 2006. (Cited on page 1.)

[5] Ernst Abbe. Beiträge zur Theorie des Mikroskops und der Mikroskopischen Wahrnehmung. *Arch. Mikroskop. Anat.*, 9:413–480, November 1873. (Cited on page 1.)

[6] G. Karagounis and R. Issa. Raman Spectra of Adsorbed Molecules : Quenching of Fluorescence by Adsorption. *Nature*, 195(4847):1196–1197, September 1962. (Cited on page 1.)

[7] G. Binnig. Tunneling through a controllable vacuum gap. *Applied Physics Letters*, 40(2):178, 1982. (Cited on pages 3, 7, and 8.)

[8] G. Binnig and H. Rohrer. Scanning tunneling microscopy. *Helvetica Physica Acta*, 55(6):726–735, 1982.

[9] G. Binnig, H. Rohrer, Ch. Gerber, and E. Weibel. Surface Studies by Scanning Tunneling Microscopy. *Physical Review Letters*, 49(1):57–61, July 1982. (Cited on page 8.)

[10] G. Binnig and H. Rohrer. In touch with atoms. *Reviews of Modern Physics*, 71(2):S324–S330, March 1999. (Cited on pages 3, 7, and 8.)

[11] H. A. Bethe. Theory of diffraction by small holes. *Physical Review*, 66(7/8):163–182, January 1944. (Cited on page 3.)

[12] E. A. Ash and G. Nicholls. Super-resolution Aperture Scanning Microscope. *Nature*, 237:510–512, 1972.

[13] D. W. Pohl, W. Denk, and M. Lanz. Optical Stethoscopy: Image recording with resolution $\lambda/20$. *Applied Physics Letters*, 44(7):651–653, January 1984.

[14] A. Harootunian, E. Betzig, M. Isaacson, and A. Lewis. Superresolution Fluorescence Near-Field Scanning Optical Microscopy. *Applied Physics Letters*, 49(11):674–676, January 1986.

[15] B. Hecht, B. Sick, U. P. Wild, V. Deckert, Renato Zenobi, O. J. F. Martin, and D. W. Pohl. Scanning near-field optical microscopy with aperture probes: Fundamentals and applications. *Journal of Chemical Physics*, 112(18):7761–7774, January 2000. (Cited on page 3.)

[16] B. Hecht, H. Bielefeldt, Y. Inouye, D. W. Pohl, and L. Novotny. Facts and artifacts in near-field optical microscopy. *Journal of Applied Physics*, 81(6):2492–2498, January 1997. (Cited on page 3.)

[17] Robin J. H. Clark and Trevor J. Dines. Resonance Raman Spectroscopy, and Its Application to Inorganic Chemistry. New Analytical Methods (27). *Angewandte Chemie International Edition in English*, 25(2):131–158, February 1986. (Cited on page 3.)

[18] Eric C. Le Ru, Lina C. Schroeter, and Pablo G. Etchegoin. Direct measurement of resonance Raman spectra and cross sections by a polarization difference technique. *Analytical chemistry*, 84(11):5074–9, June 2012. (Cited on pages 3, 4, 17, and 49.)

[19] R. Wilbrandt. Time-resolved resonance Raman spectroscopy: A retrospect on the early days. *Biospectroscopy*, 2(5):263–275, 1996. (Cited on page 4.)

[20] W. M. Kwok, C. Ma, P. Matousek, A. W. Parker, D. Phillips, W. T. Toner, M. Towrie, and S. Umapathy. A Determination of the Structure of the Intramolecular Charge Transfer State of 4-Dimethylaminobenzonitrile (DMABN) by Time-Resolved Resonance Raman Spectroscopy. *The Journal of Physical Chemistry A*, 105(6):984–990, February 2001.

[21] P. Matousek, M. Towrie, and A. W. Parker. Fluorescence background suppression in Raman spectroscopy using combined Kerr gated and shifted excitation Raman difference techniques. *Journal of Raman Spectroscopy*, 33(4):238–242, April 2002.

[22] Andrew C. Benniston, Pavel Matousek, Iain E. McCulloch, Anthony W. Parker, and Michael Towrie. Detailed Picosecond Kerr-Gated Time-Resolved Resonance Raman Spectroscopy and Time-Resolved Emission Studies of Merocyanine 540 in Various Solvents. *The Journal of Physical Chemistry A*, 107(22):4347–4353, June 2003.

[23] Philipp Kukura, David W. McCamant, Sangwoon Yoon, Daniel B. Wandschneider, and Richard A. Mathies. Structural observation of the primary isomerization in vision with

femtosecond-stimulated Raman. *Science*, 310(5750):1006–9, November 2005.

[24] Sangdeok Shim, Christina M. Stuart, and Richard A. Mathies. Resonance Raman cross-sections and vibronic analysis of rhodamine 6G from broadband stimulated Raman spectroscopy. *Chemphyschem : a European journal of chemical physics and physical chemistry*, 9(5):697–9, April 2008.

[25] Chong Fang, Renee R. Frontiera, Rosalie Tran, and Richard A. Mathies. Mapping GFP structure evolution during proton transfer with femtosecond Raman spectroscopy. *Nature*, 462(7270):200–4, December 2009. (Cited on page 4.)

[26] A. J. Mcquillan, P. J. Hendra, and M. Fleischmann. Raman spectroscopic investigation of silver electrodes. *Journal of Electroanalytical Chemistry*, 65(2):933–944, January 1975. (Cited on pages 4 and 17.)

[27] D. L. Jeanmaire and R. P. Van Duyne. Surface Raman spectroelectrochemistry. Part I. Heterocyclic, aromatic, and aliphatic amines adsorbed on the anodized silver electrode. *Journal of Electroanalytical Chemistry*, 84(1):1–20, January 1977. (Cited on pages 4 and 17.)

[28] P. G. Etchegoin, P. D. Lacharmoise, and E. C. Le Ru. Influence of photostability on single-molecule surface enhanced Raman scattering enhancement factors. *Analytical chemistry*, 81(2):682–8, January 2009. (Cited on page 4.)

[29] Lukas Novotny and Niek van Hulst. Antennas for light. *Nature Photonics*, 5(2):83–90, February 2011. (Cited on page 4.)

[30] Palash Bharadwaj, Ryan Beams, and Lukas Novotny. Nanoscale spectroscopy with optical antennas. *Chemical Science*, 2(1):136, 2011. (Cited on page 4.)

[31] R. M. Stöckle, V. Deckert, C. Fokas, D. Zeisel, and Renato Zenobi. Sub-wavelength Raman spectroscopy on silver islands. *Vibrational Spectroscopy*, 22(1-2):39–48, 2000. (Cited on page 4.)

[32] M. S. Anderson. Locally Enhanced Raman Spectroscopy with an Atomic Force Microscope. *Applied Physics Letters*, 76(21):3130–3132, 2000. (Cited on pages 4, 5, and 50.)

[33] Bruno Pettinger, Gennaro Picardi, Rolf Schuster, and Gerhard Ertl. Surface enhanced Raman spectroscopy: Towards single molecular spectroscopy. *Electrochemistry (Jp)*, 68(12):942–949, January 2000.

[34] N. Hayazawa, Yasushi Inouye, Z. Sekkat, and Satoshi Kawata. Metallized tip amplification of near-field Raman scattering. *Optics Communications*, 183(1-4):333–336, January 2000. (Cited on page 4.)

[35] Eric C. Le Ru and Pablo G. Etchegoin. Single-molecule surface-enhanced Raman spectroscopy. *Annual review of physical chemistry*, 63:65–87, January 2012. (Cited on pages 4, 20, and 21.)

[36] Achim Hartschuh. Tip-Enhanced Near-Field Optical Microscopy. *Angewandte Chemie International Edition in English*, 47(43):8178–8191, January 2008.

[37] Bruno Pettinger. Tip-enhanced Raman Spectroscopy – Recent Developments and Future Prospects. *Advances in Electrochemical Science and Engineering*, 9:377–418, 2006.

[38] Katrin F. Domke, Dai Zhang, and Bruno Pettinger. Tip-enhanced Raman spectra of picomole quantities of DNA nucleobases at Au(111). *Journal of the American Chemical Society*, 129(21):6708–6709, January 2007.

[39] Bruno Pettinger, Bin Ren Bin, Gennaro Picardi, Rolf Schuster, and Gerhard Ertl. Tip-enhanced Raman spectroscopy (TERS) of malachite green isothiocyanate at Au(111): bleaching behavior under the influence of high electromagnetic fields. *Journal of Raman Spectroscopy*, 36(6-7):541–550, January 2005. (Cited on pages 21, 23, 52, and 98.)

[40] Jens Steidtner and Bruno Pettinger. Tip-enhanced Raman spectroscopy and microscopy on single dye molecules with 15 nm resolution. *Physical Review Letters*, 100(23):236101, January 2008. (Cited on pages 4, 5, 25, 49, 51, 53, and 98.)

[41] Bruno Pettinger, Philip Schambach, Carlos J. Villagómez, and Nicola Scott. Tip-enhanced Raman spectroscopy: near-fields acting on a few molecules. *Annual review of physical chemistry*, 63:379–99, January 2012. (Cited on pages 5, 25, 50, 86, and 87.)

[42] M. Moskovits. Surface-enhanced Raman spectroscopy: a brief retrospective. *Journal of Raman Spectroscopy*, 36(6-7):485–496, January 2005.

[43] Boon-Siang Yeo, Johannes Stadler, Thomas Schmid, Renato Zenobi, and Weihua Zhang. Tip-enhanced Raman Spectroscopy - Its status, challenges and future directions. *Chemical Physics Letters*, 472(1-3):1–13, January 2009.

[44] Johannes Stadler, Benedikt Oswald, Thomas Schmid, and Renato Zenobi. Characterizing unusual metal substrates for gap-

mode tip-enhanced Raman spectroscopy. *Journal of Raman Spectroscopy*, 44(2):227–233, February 2013.

[45] Tanja Deckert-Gaudig and Volker Deckert. Nanoscale structural analysis using tip-enhanced Raman spectroscopy. *Current opinion in chemical biology*, 15(5):719–24, October 2011.

[46] Dana Cialla, Tanja Deckert-Gaudig, Christian Budich, Michael Laue, Robert Möller, Dieter Naumann, Volker Deckert, and Jürgen Popp. Raman to the limit: tip-enhanced Raman spectroscopic investigations of a single tobacco mosaic virus. *Journal of Raman Spectroscopy*, 40(3):240–243, March 2009. (Cited on page 4.)

[47] Jens Steidtner and Bruno Pettinger. High-resolution microscope for tip-enhanced optical processes in ultrahigh vacuum. *Review of scientific instruments*, 78(10):103104, January 2007. (Cited on pages 4, 5, 25, and 53.)

[48] Niculina Peica, Serge Röhrig, Andreas Rüdiger, Katharina Brose, Christian Thomsen, and Janina Maultzsch. Characterization of dye molecules and carbon nanostructures by tip-enhanced Raman spectroscopy. *Physica Status Solidi B*, 246(11-12):2708–2712, December 2009. (Cited on page 49.)

[49] Zhenglong Zhang, Li Chen, Mengtao Sun, Panpan Ruan, Hairong Zheng, and Hongxing Xu. Insights into the nature of plasmon-driven catalytic reactions revealed by HV-TERS. *Nanoscale*, 5(8):3249–52, April 2013.

[50] N. Jiang, E. T. Foley, J. M. Klingsporn, M. D. Sonntag, N. A. Valley, J. A. Dieringer, T. Seideman, G. C. Schatz, M. C. Hersam, and R. P. Van Duyne. Observation of multiple vibrational modes in ultrahigh vacuum tip-enhanced Raman spectroscopy combined with molecular-resolution scanning tunneling microscopy. *Nano letters*, 12(10):5061–7, October 2012. (Cited on page 49.)

[51] R. Zhang, Y. Zhang, Z. C. Dong, S. Jiang, C. Zhang, L. G. Chen, L. Zhang, Y. Liao, J. Aizpurua, Y. Luo, J. L. Yang, and J. G. Hou. Chemical mapping of a single molecule by plasmon-enhanced Raman scattering. *Nature*, 498(7452):82–86, June 2013. (Cited on pages 5, 25, 49, and 86.)

[52] Kai-An Wang, Ying Wang, Ping Zhou, J. Holden, Song-lin Ren, G. Hager, H. Ni, P. Eklund, G. Dresselhaus, and M. Dresselhaus. Raman scattering in C60 and alkali-metal-doped C60 films. *Physical Review B*, 45(4):1955–1958, January 1992. (Cited on page 5.)

[53] P.C. Eklund, Zhou Ping, Wang Kai-An, G. Dresselhaus, and M.S. Dresselhaus. Optical phonon modes in solid and doped C60. *Journal of Physics and Chemistry of Solids*, 53(11):1391–1413, November 1992. (Cited on pages 49 and 50.)

[54] Ping Zhou, Kai-An Wang, Ying Wang, P. Eklund, M. Dresselhaus, G. Dresselhaus, and R. Jishi. Raman scattering in C60 and alkali-metal-saturated C60. *Physical Review B*, 46(4):2595–2605, July 1992.

[55] J.S. Duclos, R.C. Haddon, and S. Glarum. Raman studies of alkali-metal doped A xC 60 films (A=Na, K, Rb and Cs; x=0, 3, and 6). *Science*, 254(5038):1625–7, 1991.

[56] Donald S. Bethune, Gerard Meijer, Wade C. Tang, and Hal J. Rosen. The vibrational Raman spectra of purified solid films of C60 and C70. *Chemical Physics Letters*, 174(3-4):219–222, November 1990.

[57] Ping Zhou, A. M. Rao, Kai-An Wang, J. D. Robertson, C. Eloi, Mark S. Meier, S. L. Ren, Xiang-Xin Bi, P. C. Eklund, and M. S. Dresselhaus. Photo-assisted structural transition and oxygen diffusion in solid C60 films. *Applied Physics Letters*, 60(23):2871, 1992.

[58] D.W. Snoke and M. Cardona. A bond polarizability model for the C60 Raman spectrum. *Solid State Communications*, 87(2):121–126, July 1993.

[59] S. Guha, J. Menéndez, J. Page, G. Adams, G. Spencer, J. Lehman, P. Giannozzi, and S. Baroni. Isotopically resolved Raman spectra of C60. *Physical Review Letters*, 72(21):3359–3362, May 1994.

[60] S. Guha, J. Menéndez, J. Page, and G. Adams. Empirical bond polarizability model for fullerenes. *Physical Review B*, 53(19):13106–13114, May 1996.

[61] Zhixun Luo, Boon H. Loo, Aidong Peng, Ying Ma, Hongbing Fu, and Jiannian Yao. Single-molecule surface-enhanced Raman scattering of fullerene C60. *Journal of Raman Spectroscopy*, 42(3):319–323, March 2011.

[62] Camille G. Artur, Rowan Miller, Matthias Meyer, Eric C. Le Ru, and Pablo G. Etchegoin. Single-molecule SERS detection of C60. *Physical chemistry chemical physics : PCCP*, 14(9):3219–25, March 2012. (Cited on pages 49 and 55.)

[63] R. M. Stockle, Y. D. Suh, Volker Deckert, and Renato Zenobi. Nanoscale chemical analysis by tip-enhanced Raman spectroscopy. *Chemical Physics Letters*, 318(1-3):131–136, January 2000. (Cited on pages 5 and 50.)

[64] J. J. Wang, D. A. Smith, D. N. Batchelder, Y. Saito, J. Kirkham, C. Robinson, K. Baldwin, G LI, and B. Bennett. Aperture-less near-field Raman spectroscopy. *Journal of Microscopy*, 210(3):330–333, June 2003.

[65] Prabhat Verma, Kohei Yamada, Hiroyuki Watanabe, Yasushi Inouye, and Satoshi Kawata. Near-field Raman scattering investigation of tip effects on C60 molecules. *Physical Review B*, 73(4):045416, January 2006. (Cited on pages 5 and 50.)

[66] Eric I. Altman and Richard J. Colton. Nucleation, growth, and structure of fullerene films on Au(111). *Surface Science*, 279(1-2):49–67, December 1992. (Cited on pages 5, 36, and 51.)

[67] Eric I. Altman and Richard J. Colton. The interaction of C60 with noble metal surfaces. *Surface Science*, 295(1-2):13–33, September 1993. (Cited on pages 36, 51, and 82.)

[68] E. I. Altman and R. J. Colton. Determination of the orientation of C60 adsorbed on An(111) and Ag(111). *Physical Review B*, 48(24), 1993. (Cited on pages 5 and 51.)

[69] Vladimir Shalaev and Andrey Sarychev. Nonlinear optics of random metal-dielectric films. *Physical Review B*, 57(20):13265–13288, May 1998. (Cited on page 7.)

[70] G. Binnig, C. F. Quate, and Ch. Gerbe. Atomic Force Microscope. *Physical Review Letters*, 56(9):930–933, March 1986. (Cited on page 7.)

[71] Gunnar Schulze. *Elementary Processes in Single Molecule Devices: Electronic Transport and Molecular Isomerization*. PhD thesis, 2009. (Cited on pages 9 and 10.)

[72] J. Tersoff and D.R. Hamann. Theory and Application for the Scanning Tunneling Microscope. *Physical Review Letters*, 50(25):1998–2001, 1983. (Cited on pages 8, 11, and 12.)

[73] J. Bardeen. Tunnelling from a many-particle point of view. *Physical Review Letters*, 6(2):57–59, 1961. (Cited on pages 8 and 11.)

[74] Derek A. Long. *The Raman Effect. A Unified Treatment of the Theory of Raman Scattering by Molecules*. Wiley, 2001. (Cited on page 14.)

[75] M. Fleischmann, P.J. Hendra, A. J. McQuillan, R. L. Paul, and E. S. Reid. Raman spectroscopy at electrode-electrolyte interfaces. *Journal of Raman Spectroscopy*, 4(3):269–274, January 1976. (Cited on page 17.)

[76] Andreas Otto and Masayuki Futamata. Electronic Mechanisms of SERS. In K. Kneipp, M. Moskovits, and H. Kneipp, editors, *Topics in Applied Physics: Surface-Enhanced Raman Scattering*, volume 103, pages 147–182. Springer, 2006. (Cited on page 18.)

[77] E. Burstein, Y.J. Chen, C.Y. Chen, S. Lundquist, and E. Tosatti. „Gian"Raman scattering by adsorbed molecules on metal surfaces. *Solid State Communications*, 29(8):567–570, February 1979. (Cited on page 18.)

[78] J. Billmann and A. Otto. Electronic Surface-State Contribution To Surface Enhanced Raman-Scattering. *Solid State Communications*, 44(2):105–107, January 1982. (Cited on page 18.)

[79] A. Otto. On the contribution of charge transfer excitations to SERS. *Journal of Electron Spectroscopy and Related Phenomena*, 29(1):329–342, January 1983.

[80] J Billmann and A Otto. Charge-Transfer between Adsorbed Cyanide and Silver Probed by SERS. *Surface Science*, 138(1):1–25, January 1984. (Cited on page 18.)

[81] L. Novotny and B. Hecht. *Principles of Nano-Optics*. Cambridge. (Cited on pages 18, 19, and 46.)

[82] Hongxing Xu, Xue-Hua Wang, Martin Persson, H. Xu, Mikael Käll, and Peter Johansson. Unified Treatment of Fluorescence and Raman Scattering Processes near Metal Surfaces. *Physical Review Letters*, 93(24):243002, December 2004. (Cited on page 20.)

[83] Martin Moskovits. Surface-enhanced spectroscopy. *Reviews of Modern Physics*, 57(3):783–826, July 1985.

[84] K. Kneipp, H. Kneipp, I. Itzkan, R. R. Dasari, and M. S. Feld. Surface-enhanced Raman scattering and biophysics. *Journal of Physics: Condensed Matter*, 14(18):R597—-R624, January 2002.

[85] E.C. Le Ru and P.G. Etchegoin. Rigorous justification of the $|E|^4$ enhancement factor in Surface Enhanced Raman Spectroscopy. *Chemical Physics Letters*, 423(1-3):63–66, May 2006. (Cited on pages 20 and 21.)

[86] Evan J. Blackie, Eric C. Le Ru, and Pablo G. Etchegoin. Single-Molecule Surface-Enhanced Raman Spectroscopy of Nonresonant Molecules. *Journal of the American Chemical Society*, 131(40):14466–14472, January 2009. (Cited on page 20.)

[87] Eric C. Le Ru and Pablo G. Etchegoin. *Principles of surface-enhanced Raman spectroscopy and related plasmonic effects*. Amsterdam: Elsevier, 2009. (Cited on page 21.)

[88] Eric C. Le Ru, Pablo G. Etchegoin, and M. Meyer. Enhancement factor distribution around a single surface-enhanced Raman scattering hot spot and its relation to single molecule detection. *Journal of Chemical Physics*, 125(20):204701, January 2006. (Cited on page 21.)

[89] Rufus Boyack and Eric C. Le Ru. Investigation of particle shape and size effects in SERS using T-matrix calculations. *Physical chemistry chemical physics : PCCP*, 11(34):7398–405, September 2009. (Cited on page 21.)

[90] Ioan Notingher and Alistair Elfick. Effect of sample and substrate electric properties on the electric field enhancement at the apex of SPM nanotips. *The Journal of Physical Chemistry B*, 109(33):15699–706, August 2005. (Cited on pages 21 and 23.)

[91] Andrew Downes, Donald Salter, and Alistair Elfick. Finite element analysis of tip-enhanced Raman scattering. *Proc. of SPIE*, 6195:61950D–61950D–13, April 2006. (Cited on page 21.)

[92] A. Hartschuh, N. Anderson, and L. Novotny. Near-field Raman spectroscopy using a sharp metal tip. *Journal of Microscopy*, 210:234–240, January 2003. (Cited on pages 21, 23, 86, and 105.)

[93] Johannes Stadler, Thomas Schmid, and Renato Zenobi. Nanoscale chemical imaging of single-layer graphene. *ACS nano*, 5(10):8442–8, October 2011. (Cited on page 23.)

[94] Bruno Pettinger, Katrin F. Domke, Dai Zhang, Gennaro Picardi, and Rolf Schuster. Tip-enhanced Raman scattering: Influence of the tip-surface geometry on optical resonance and enhancement. *Surf. Sci.*, 603(10-12):1335–1341, January 2009. (Cited on page 23.)

[95] Bruno Pettinger, Katrin F. Domke, Dai Zhang, Rolf Schuster, and Gerhard Ertl. Direct monitoring of plasmon resonances in a tip-surface gap of varying width. *Physical Review B*, 76(11):113409, January 2007. (Cited on pages 23 and 73.)

[96] Jens Steidtner. Spitzenverstärkte Ramanspektroskopie und -mikroskopie im Ultrahochvakuum. *PhD thesis*, 2007. (Cited on pages 25, 28, 37, and 53.)

[97] M. A. Lieb and A. J. Meixner. A high numerical aperture parabolic mirror as imaging device for confocal microscopy. *Optics Express*, 8(7):458–474, January 2001. (Cited on pages 25 and 46.)

[98] M. Andreas Lieb. *Mikroskopie mit Parabolspiegeloptik*. PhD thesis, 2001. (Cited on page 46.)

[99] A. Ghanadzadeh Gilani, S. E. Hosseini, M. Moghadam, and E. Alizadeh. Excited state electric dipole moment of nile blue and brilliant cresyl blue: a comparative study. *Spectrochimica acta. Part A, Molecular and biomolecular spectroscopy*, 89:231–7, April 2012. (Cited on page 49.)

[100] J. Menendez and J.B. Page. Vibrational spectroscopy of C60. In M. Cardona and G. Güntherodt, editors, *Light Scattering in Solids VIII*, volume 76, pages 27–95. Springer, Berlin, 2000. (Cited on pages 54, 55, 56, and 70.)

[101] Zhi-Min Zhang, Shan Chen, Yi-Zeng Liang, Zhao-Xia Liu, Qi-Ming Zhang, Li-Xia Ding, Fei Ye, and Hua Zhou. An intelligent background-correction algorithm for highly fluorescent samples in Raman spectroscopy. *Journal of Raman Spectroscopy*, 41(6):659–669, October 2009. (Cited on pages 55 and 72.)

[102] Ronald Birke, John Lombardi, and Joel Gersten. Observation of a Continuum in Enhanced Raman Scattering from a Metal-Solution Interface. *Physical Review Letters*, 43(1):71–75, July 1979. (Cited on page 55.)

[103] A. Otto, I. Mrozek, H. Grabhorn, and W. Akemann. Surface-Enhanced Raman-Scattering. *Journal of Physics: Condensed Matter*, 4(5):1143–1212, January 1992.

[104] E. C. Le Ru and P. G. Etchegoin. Surface-Enhanced Raman Scattering (SERS) and Surface-Enhanced Fluorescence (SEF) in the context of modified spontaneous emission. *arXiv:physics [physics.chem-ph]*, (0509154), 2005. (Cited on page 55.)

[105] Zhixun Luo and Yan Fang. SERS of C60/C70 on gold-coated filter paper or filter film influenced by the gold thickness. *Journal of colloid and interface science*, 283(2):459–63, March 2005. (Cited on pages 58 and 59.)

[106] Stewart F Parker, Stephen M Bennington, Jon W Taylor, Henryk Herman, Ian Silverwood, Peter Albers, and Keith Refson. Complete assignment of the vibrational modes of C60 by inelastic neutron scattering spectroscopy and periodic-DFT. *Physical chemistry chemical physics : PCCP*, 13(17):7789–804, May 2011. (Cited on pages 58 and 59.)

[107] R. Henry, E. and J. Hofrichter. Singular value decomposition: Application to analysis of experimental data. *Methods in Enzymology*, 210:129–192, 1992. (Cited on page 73.)

[108] Matthias Elgeti, Eglof Ritter, and Franz J. Bartl. New Insights into Light-Induced Deactivation of Active Rhodopsin by SVD and Global Analysis of Time-Resolved UV/Vis- and FTIR-Data.

Zeitschrift für Physikalische Chemie, 222(8-9):1117–1129, August 2008. (Cited on page 73.)

[109] V. Davydov, L. Kashevarova, A. Rakhmanina, V. Senyavin, R. Céolin, H. Szwarc, H. Allouchi, and V. Agafonov. Spectroscopic study of pressure-polymerized phases of C60. *Physical Review B*, 61(18):11936–11945, May 2000. (Cited on pages 81, 84, and 85.)

[110] M. S. Dresselhaus, G. Dresselhaus, and P. C. Eklund. *Science of Fullerenes and Carbon Nanotubes.*, volume 381. Academic Press, San Diego, May 1996. (Cited on page 82.)

[111] Ping Zhou, Zheng-Hong Dong, A.M. Rao, and P.C. Eklund. Reaction mechanism for the photopolymerization of solid fullerene C60. *Chemical Physics Letters*, 211(4-5):337–340, August 1993. (Cited on page 82.)

[112] Ying Wang, J.M. Holden, Xiang-xin Bi, and P.C. Eklund. Thermal decomposition of polymeric C60. *Chemical Physics Letters*, 217(4):413–417, January 1994. (Cited on page 82.)

[113] Masato Nakaya, Yuji Kuwahara, Masakazu Aono, and Tomonobu Nakayama. Reversibility-controlled single molecular level chemical reaction in a C60 monolayer via ionization induced by a scanning tunneling microscope. *Small*, 4(5):538–41, May 2008. (Cited on page 94.)

[114] Xi Wang, Zheng Liu, Mu-De Zhuang, Hai-Ming Zhang, Xiang Wang, Zhao-Xiong Xie, De-Yin Wu, Bin Ren Bin, and Zhong-Qun Tian. Tip-enhanced Raman spectroscopy for investigating adsorbed species on a single-crystal surface using electrochemically prepared Au tips. *Applied Physics Letters*, 91(10):101105, January 2007. (Cited on pages 104, 106, and 111.)

[115] S. W. Schmucker, N. Kumar, J. R. Abelson, S. R. Daly, G. S. Girolami, M. R. Bischof, D. L. Jaeger, R. F. Reidy, B. P. Gorman, J. Alexander, J. B. Ballard, J. N. Randall, and J. W. Lyding. Field-directed sputter sharpening for tailored probe materials and atomic-scale lithography. *Nature communications*, 3:935, January 2012. (Cited on page 105.)

[116] D. Roy, C. M. Williams, and K. Mingard. Single-crystal gold tip for tip-enhanced Raman spectroscopy. *Journal of Vacuum Science & Technology B: Microelectronics and Nanometer Structures*, 28(3):631, 2010. (Cited on pages 105 and 109.)

[117] Bin Ren, Gennaro Picardi, and Bruno Pettinger. Preparation of gold tips suitable for tip-enhanced Raman spectroscopy and light emission by electrochemical etching. *Review of scientific instruments*, 75(4):837–841, January 2004. (Cited on page 106.)

[118] B.W. Mao, B. Ren, X.W. Cai, and L.H. Xiong. Electrochemical oscillatory behavior under a scanning electrochemical microscopic configuration. *Journal of Electroanalytical Chemistry*, 394(1-2):155–160, September 1995. (Cited on page 106.)

[119] Max Eisele, Michael Krüger, Markus Schenk, Alexander Ziegler, and Peter Hommelhoff. Note: Production of sharp gold tips with high surface quality. *Review of scientific instruments*, 82(2):026101, February 2011. (Cited on page 110.)

CURRICULUM VITAE

Der Lebenslauf ist in der Online-Version aus Gründen des Datenschutzes nicht enthalten.

PUBLISHED WORK

Bruno Pettinger, Philip Schambach, Carlos J. Villagómez, and Nicola Scott. Tip-enhanced Raman spectroscopy: Near-fields acting on a few molecules. *Annual review of physical chemistry*, 63:379-99, 2012.

DANKSAGUNG

An dieser Stelle möchte ich mich bei allen bedanken, die zum Erfolg dieser Arbeit beigetragen haben.

Als Erstes möchte ich Herrn Prof. Dr. Martin Wolf dafür danken, dass ich in seiner Abteilung Physikalische Chemie meine Doktorarbeit durchführen durfte und dafür, dass er mir die Möglichkeit gegeben hat, mein Forschungsvorhaben zu verwirklichen.

Frau Prof. Dr. Stephanie Reich danke ich für die Bereitschaft das Zweitgutachten zu meiner Arbeit zu erstellen, sowie dafür, dass sie mir stets mit ihrem kompetenten Rat zur Seite stand.

Herrn Dr. Bruno Pettinger möchte ich dafür danken, dass er mir ermöglicht hat an einem sehr spannenden und herausfordernden Thema zu arbeiten. Ich danke Ihm auch für seine guten Ideen und seine fachliche Förderung und zahlreiche wissenschaftliche Diskussionen.

Herrn Prof. Dr. Hans-Joachim Freund danke ich dafür, dass wir unsere Experimente in seiner Abteilung Chemische Physik durchführen und alle dort vorhandene Einrichtungen nutzen konnten.

Herrn Dr. Takashi Kumagai danke ich dafür, dass ich meine Tätigkeit in seiner neugegründeten Arbeitsgruppe fortsetzen konnte, sowie für das Mitwirken an einigen der hier veröffentlichten Messungen.

Ferner möchte ich mich noch bei Dr. Nicola Scott, Dieter Bauer und Dr. Carlos Villagomez aus der UHV-TERS Gruppe für die gute Zusammenarbeit und Unterstützung bedanken.

Besonderer Dank gilt Sven Kubala. Er hat mich immer wieder kompetent und tatkräftig bei zahlreichen Um- und Aufbauarbeiten unterstützt.

Eine Arbeit wie diese lässt sich nicht alleine bewerkstelligen. Ich bin sehr glücklich darüber, dass ich mich immer auf die Hilfe und den Rat meiner Kollegen verlassen konnte. Sie haben für eine sehr gute und produktive Arbeitsatmosphäre gesorgt. Besonders will ich hierfür den folgenden Personen danken: Christin Büchner, Dr. Fernando Stavale, Dr. Frauke Bierau, Gero Thielsch, Gisela Weinberg, Jan Rocker, Jonas Lähnemann, Klaus Peter Vogelgesang, Prof. Dr. Leon-

hard Grill, Dr. Markus Düttmann, Dr. Markus Heide, Dr. Martin Sterrer, Dr. Matthias Elgeti, Matthias Naschitzki, Dr. Mathis Gruber, Prof. Dr. Niklas Nilius, Dr. Peter Kupser, Sebastian Heeg, Stefanie Stuckenholz und Walter Wachsmann.

Der International Max Planck Research School (IMPRS) will ich für viele lehrreiche Veranstaltungen und vor allem für die Möglichkeit danken, mit meinen Kollegen eine Konferenz zu organisieren.

Dem Elab, der Feinwerktechnik und der Haustechnik danke ich für die gute Zusammenarbeit.

Bei Dr. Frank Hitzel and Glenn Nielsen von DME bedanke ich mich für die gute Beratung.

All meinen Freunden danke ich für die moralische Unterstützung.

Ganz besonders bedanke ich mich bei meinen Eltern, die mich bei meiner Ausbildung unterstützt und somit den Grundstein für diese Arbeit gelegt haben.

Der größte Dank gebührt meiner Freundin Hélène.

SELBSTÄNDIGKEITSERKLÄRUNG

Hiermit erkläre ich, dass ich die vorliegende Arbeit selbständig und nur unter Verwendung der angegebenen Quellen und Hilfsmittel angefertigt habe.

Berlin, August 2013

Philip Schambach